A Uniform Atmospheric Retrieval Analysis of Ultra-Cool Brown Dwarfs

by

Joseph A. Zalesky

A Dissertation Presented in Partial Fulfillment
of the Requirements for the Degree
Doctor of Philosophy

Approved August 2022 by the
Graduate Supervisory Committee:

Michael R. Line, Chair
Jennifer Patience
Christopher Groppi
Patrick Young
Maitrayee Bose

ARIZONA STATE UNIVERSITY

December 2022

ABSTRACT

Brown dwarfs are a unique class of object which span the range between the lowest mass stars, and highest mass planets. New insights into the physics and chemistry of brown dwarfs comes from the comparison between spectroscopic observations, and theoretical atmospheric models. In this thesis, I present a uniform atmospheric retrieval analysis of the coolest Y, and late-T spectral type brown dwarfs using the CaltecH Inverse ModEling and Retrieval Algorithms (CHIMERA). In doing so, I develop a foundational dataset of retrieved atmospheric parameters including: molecular abundances, thermal structures, evolutionary parameters, and cloud properties for 61 different brown dwarfs. Comparisons to other modeling techniques and theoretical expectations from the James Webb Space Telescope (JWST) are made. Finally, I describe the techniques used to improve CHIMERA to run on Graphical Processing Units (GPUs), which directly enabled the creation of this large dataset.

DEDICATION

To my family, my friends, my pet rabbit Louie, and my love Wanda. Thank you for helping me to see the light in the darkness.

TABLE OF CONTENTS

LIST OF TABLES

LIST OF FIGURES

Chapter 1

INTRODUCTION

Brown dwarfs are a unique class of objects which were theorized to exist almost 60 years ago (Hayashi and Nakano, 1963; Kumar, 1963), and observationally confirmed within the last 40 (Becklin and Zuckerman, 1988; Rebolo *et al.*, 1995; Oppenheimer *et al.*, 1995). While not being massive enough to to fuse hydrogen into helium like their stellar cousins, they are both too massive, and form through different processes, than planets (Shu, 1977; Saumon *et al.*, 1996; Boss, 2001; Bate *et al.*, 2003). This places the study of brown dwarfs' atmospheric processes at an intersection between stellar astrophysics, and planetary science (Marley and Robinson, 2015).

Brown dwarfs' atmospheric properties span a range between cooler, Jovian-mass planets and the coolest, lowest mass stars ($3000K \gtrsim \mathrm{T_{eff}} \gtrsim 200K$) (Burrows *et al.*, 2001). Within this range are the L, T, and Y Dwarf sub-classes. Each of these host unique atmospheric molecular signatures which have historically defined the transition between each type (methane, CH_4, for L to T, and ammonia, NH_3, for T to Y) (Oppenheimer *et al.*, 1995; Kirkpatrick *et al.*, 1999; Cushing *et al.*, 2005; Kirkpatrick, 2005; Cushing *et al.*, 2011).

This body of knowledge was largely established through methods similar to stellar astrophysics, whereby comparisons between atmospheric models, originally developed for stars, and observational spectra and photometry were made. In particular, *self-consistent* atmospheric models, that are models which retain a self-consistent treatment of the atmosphere through radiative-convective-thermochemical equilibrium, were largely responsible for this initial development (Marley *et al.*, 1996; Burrows *et al.*, 2001; Marley *et al.*, 2002; Knapp *et al.*, 2004; Marley *et al.*, 2010). While these

models provide a self-consistent treatment of the atmosphere, there are well-known shortcomings with this approach. Most notably are poorly fitting spectra, either due to missing physics and/or a lack of model flexibility (Patience *et al.*, 2012; Leggett *et al.*, 2017), and artificially precise constraints due to improper interpolation from the grid of model parameter points (Cottaar *et al.*, 2014; Czekala *et al.*, 2015a). In particular, one of the major theoretical challenges has been accurately modeling the impact of condensate clouds that act to mute spectral features by creating obscuring layers in the photosphere. However, without models which can reproduce key spectral features, it is difficult to interpret where and to what level of complexity cloud physics is needed. Though there have been efforts to remedy some of these problems (Morley *et al.*, 2012; Marley *et al.*, 2021a), self-consistent modeling of substellar atmospheres has proven to be a challenging theoretical bottleneck over the last two decades that warranted the development of new approaches.

Borrowing from the success of solar system studies (Twomey *et al.*, 1977; Fletcher *et al.*, 2007; Lee *et al.*, 2012; Line *et al.*, 2012; Benneke and Seager, 2012), the technique of *atmospheric retrieval* has provided a powerful alternative that addresses the issues inherent to self-consistent modeling (Line *et al.*, 2015, 2017). Atmospheric retrieval relaxes many of the self-consistent assumptions and instead opts to use a forward radiative transfer model with more free parameters. This method allows the spectroscopic data to drive the best-fit solution and, despite the increase in number of free parameters, is often the preferred model to match both space and ground-based observations (Line *et al.*, 2017). The relaxation of the assumption of thermochemical equilibrium also allows for first direct measurement of the relative molecular abundances (e.g. H_2O, CH_4, and CO) in substellar atmospheres. Thus, atmospheric retrieval of both brown dwarf and exoplanets enables new exploration of key outstanding questions in atmospheric physics and chemistry.

The recent National Academies' Decadal Survey on Astronomy and Astrophysics 2020 highlighted one of these questions, "How do giant planets fit within a continuum of our understanding of all substellar objects?" They noted that brown dwarfs, "offer the opportunity to rigorously test models of thermal evolution, atmospheric dynamics, chemistry, [and] cloud formation that are also applicable to extrasolar giant planets. Characterizing the differences and similarities of the two classes of object will elucidate their formation mechanisms, informing the limits of both planet and star formation." The focus of my dissertation has been directly aligned with answering this, and several other related questions.

The outstanding questions explored in this work are: (1) What are the atmospheric compositions of substellar objects? (2) What important physical and chemical processes affect their elemental and molecular abundances? (3) How do the abundance distributions of stars, brown dwarfs, and exoplanets compare? (4) Given the limits of current and future instrumentation, how well should we be able to constrain substellar atmospheres? (5) Where can improvements in atmospheric modeling result in new knowledge about these substellar worlds?

To answer these questions, Chapter 2 begins with studying a population of the coldest brown dwarfs, the Y dwarfs. Chapter 2 uses observations from the Hubble Space Telescope's Wide Field Camera 3, and the retrieval model CHIMERA, to establish fundamental trends of: the vertical temperature structure; fundamental parameters such as $T_{\rm eff}$, gravity, radius, & mass; and finally the elemental and molecular atmospheric composition for the Y dwarf spectral class. A comparison of these results to more traditional grid models are also carried out to provide a more holistic understanding of their atmospheres. Chapter 2 concludes with predictions for the performance from the James Webb Space Telescope, for which, after many years, we are finally beginning to receive observations from.

Chapter 3 diverts from purely scientific results into an application of using graphical processing units to address the computational expense of performing atmospheric retrievals. Following a discussion on the fundamental limitations of the CHIMERA model, a detailed explanation of the software used to accomplish an over order of magnitude decrease in the runtime of the retrieval model is given.

Chapter 4 returns to pure science to analyze a much larger sample of 50 late-T dwarfs, enabled by the computational advances made in Chapter 3. This chapter establishes the largest dataset of retrieved brown dwarf atmospheric properties to date. This includes a detailed discussion of their thermal structures, atmospheric composition, and again fundamental parameters such as $T_{\rm eff}$, and gravity. Detail on any objects which deviate from the observed trends are discussed. Finally, a succinct summary of all the major findings presented in this thesis, and possible directions of future research, are provided in Chapter 5.

Chapter 2

PROPERTIES OF Y DWARFS

2.1 Abstract

Ultra-cool brown dwarfs offer a unique window into understanding substellar atmospheric physics and chemistry. Their strong molecular absorption bands at infrared wavelengths, Jupiter-like radii, cool temperatures, and lack of complicating stellar irradiation make them ideal test beds for understanding Jovian-like atmospheres. Here, we report the findings of a uniform atmospheric retrieval analysis on a set of 14 Y- and T-type dwarfs observed with the Hubble Space Telescope Wide Field Camera 3 instrument. From our retrieval analysis, we find the temperature structures to be largely consistent with radiative-convective equilibrium in most objects. We also determine the abundances of water, methane, and ammonia, as well as upper limits on the alkali metals sodium and potassium. The constraints on water and methane are consistent with predictions from chemical equilibrium models, while those of ammonia may be affected by vertical disequilibrium mixing, consistent with previous works. Our key result stems from the constraints on the alkali metal abundances where we find their continued depletion with decreasing effective temperature, consistent with the trend identified in a previous retrieval analysis on a sample of slightly warmer late T-dwarfs in Line et al. (2017). These constraints show that the previously observed Y-J color trend across the T/Y transition is most likely due to the depletion of these metals, in

accordance with predictions from equilibrium condensate rainout chemistry. Finally, we simulate future James Webb Space Telescope observations of ultra-cool dwarfs and find that the Near Infrared Spectrometer (NIRSpec) PRISM offers the best chance at developing high-precision constraints on fundamental atmospheric characteristics.

2.2 Introduction

Brown dwarfs have solicited intriguing questions since their discovery several decades ago (Becklin and Zuckerman, 1988; Rebolo *et al.*, 1995; Oppenheimer *et al.*, 1995). While not being massive enough to to fuse hydrogen into helium (Hayashi and Nakano, 1963; Kumar, 1963), they were still too massive to be considered as "traditional" planets following the roughly $13M_{Jup}$ definition based on the fusion of deuterium (Shu, 1977; Saumon *et al.*, 1996). More recently there have been arguments that formation pathways, rather than mass limits, are more useful when defining the difference between brown dwarfs and planets (Boss, 2001; Bate *et al.*, 2003). This has placed the study of brown dwarfs at an interesting crossroads between planetary science and stellar astrophysics. Efforts to understand the physics of brown dwarfs have thus pulled methodologies from both fields in order to measure the physical characteristics and understand the evolution of these objects (for a review, Marley and Robinson, 2015).

Motivation for studying the atmospheres of brown dwarfs is two-fold. First, brown dwarfs do not have a stable internal energy source, and thus their evolution is highly dependent upon their initial formation mass (e.g. Baraffe *et al.*, 2003) and specific physical/chemical structure of their atmosphere (e.g. Saumon and Marley, 2008). Secondly, brown dwarfs offer the chance to study planetary-like atmospheric conditions, while not having to include the complication of an irradiating host star. Understanding the physical and chemical mechanisms at work in cooler brown dwarf atmospheres

thus provides constraints on both their evolution, and the characteristics of planetary-like atmospheres.

The bulk properties of field brown dwarfs (mass, radius, $T_{\rm eff}$, etc.) have been well studied over the past several decades (for a review, Burrows *et al.*, 2001). With cool effective temperatures ($200K \lesssim T_{\rm eff} \lesssim 3000K$) over photospheric pressures ($300 \lesssim P \lesssim 10^{-4}$ bar), their thermal emission predominately radiates in the near-to-mid infrared, with their spectra being sculpted by strong molecular and atomic opacities of species such as: hydrogen and helium (H_2/He), water (H_2O), methane (CH_4), ammonia (NH_3), and alkali metals such as potassium (K) and sodium (Na) for the coolest objects to carbon monoxide and dioxide (CO,CO_2), H_2O, H_2/He, and metal hydrides and oxides for the hottest (Fegley and Lodders, 1996; Lodders and Fegley, 2002; Lodders, 2003). The precise molecular and cloud compositions, and their evolution with temperature, give rise to spectral signatures which define the L-T-Y spectroscopic classes (Oppenheimer *et al.*, 1995; Kirkpatrick *et al.*, 1999; Cushing *et al.*, 2005; Kirkpatrick, 2005; Cushing *et al.*, 2011).

While empirical approaches exist (e.g. Cruz *et al.*, 2009; Filippazzo *et al.*, 2015), the primary method of choice for inferring atmospheric properties relies upon detailed comparisons between theoretical models and the observed spectra. This often takes the form of pre-computing a large grid of theoretical spectra across a range of key physical parameters (Allard *et al.*, 1996, 2012; Marley *et al.*, 1996; Tsuji *et al.*, 1996). Most commonly these grids include effective temperature and gravity, but more recently have been modified to include variable cloud models (Ackerman and Marley, 2001; Marley *et al.*, 2002), eddy diffusion within the atmosphere (Saumon *et al.*, 2006), rainout of specific condensates, and varying metallicity and carbon-to-oxygen (C/O) ratios (Marley *et al.*, 2017; Mollière *et al.*, 2017; Samland *et al.*, 2017). These large grid models are then interpolated between grid points and fit via standard maximum

likelihood comparisons (e.g. Cushing *et al.*, 2008) or modern MCMC methods (e.g. Madhusudhan and Seager, 2011; Rice *et al.*, 2015; Mann *et al.*, 2015; Samland *et al.*, 2017).

Though this grid modeling approach provides a useful baseline for beginning the analysis of infrared spectra, it has been shown to fail to accurately reproduce key spectral features, and often provides poor fits to the data (e.g. Leggett *et al.*, 2017). For example, Patience *et al.* (2012) has demonstrated that grid models from different groups cannot reproduce statistically similar results for the same dataset of young brown dwarf companions. These inconsistencies between grid model fitting and the observational data suggest that not all of the possible atmospheric physics and chemistry is being taken into account within the established grid models. Despite this, a more recent effort in Baudino *et al.* (2017) found greater consistency between several widely-used grid models, though outstanding issues in abundance determinations still remain. These inconsistencies motivate the need for a new methodology to compliment the grid-modeling approach to reach a more complete understanding of brown dwarf spectra.

Realizing the limitations of the grid modeling approach, Line *et al.* (2015, 2017) (hereafter Parts I & II) applied well established atmospheric retrieval (Twomey *et al.*, 1977; Fletcher *et al.*, 2007; Lee *et al.*, 2012; Line *et al.*, 2012; Benneke and Seager, 2012) tools to the problem by performing a uniform retrieval analysis on a sample of late-T dwarfs. In Part I, the authors were able to validate their model on two benchmark T-dwarfs by showing that the overall retrieved abundances and C/O ratios were consistent with the objects' stellar companion. With the larger sample (11 T7-T8 targets) in Part II, they found a strong depletion of the combined Na+K abundances with decreasing $T_{\rm eff}$. This had long been a theoretical expectation from rainout chemistry (Fegley and Lodders, 1994), and hypothesized from trends of near-infrared colors

(Marley *et al.*, 2002; Leggett *et al.*, 2010; Liu *et al.*, 2012; Lodieu *et al.*, 2013), but the measured abundance depletion had never been directly detected. These investigations demonstrate that the retrieval method as applied to brown dwarf atmospheres is able to constrain key atmospheric properties often overlooked in traditional methods.

Our primary goals in this work, Part III, are to both expand the previously analyzed dataset into the cooler, early-Y dwarf (Y0-Y1) regime to see if the trends identified in Part II continue to cooler temperatures, and to test the various model assumptions made in Parts I & II. This is accomplished by performing a retrieval analysis on a set of objects from Schneider *et al.* (2015), which contains near-IR (0.9-1.7μm, Y,J,H band) spectra of 6 late-T and 16 early-Y dwarfs using Hubble Space Telescope's Wide Field Camera 3 (HST,WFC3).

In Section 2.3 we briefly outline the methods of our atmospheric retrieval model. Section 2.4 discusses the dataset from WFC3 and the history of our targets. Constraints on the temperature structure (Section 2.5.1), evolutionary parameters (Section 2.5.2), and chemical abundances (Section 2.5.3) are then discussed. We also perform a comparison of our retrieval method with a recently published grid model in Section 2.5.4. In Section 2.6 we predict how well the future *James Webb Space Telescope* (*JWST*) will be able to improve our constraints. Finally, we list our primary conclusions in Section 2.7.

2.3 Methods

We utilize the same basic retrieval framework and forward model as described in Part's I and II, briefly summarized here. The model includes 31 free-parameters which include: constant-with-altitude volume mixing ratios (VMR's) for: H_2O, CH_4, NH_3, CO, CO_2, H_2S, and a combined alkali [Na+K] fixed at a solar ratio (7 in total), gravity, radius-to-distance scale factor $(R/D)^2$, 15 independent temperature-

Table 2.1: 31 Free-Parameters in Our Retrieval Model

Parameter	Description
$\log(f_i)$	7 log(constant-with-altitude Volume Mixing Ratios)
log(g)	$\log(GM/R^2)$ [cm s^{-2}]
$(R/D)^2$	radius-to-distance scale [R_{Jup}/pc]
T(P)	temperature at 15 pressure levels [K]
$\Delta\lambda$	wavelength calibration uncertainty [nm]
b	errorbar inflation exponent (Part I, Equation 3)
γ, β	TP-profile smoothing hyperparameters (Part I, Table 2/Equation 5)
$\kappa_{P_0}, P_0, \alpha$	Cloud profile parameters (Part II, Equation 1)

pressure (TP) profile points implemented within a Gaussian-Process-like smoothing framework, and a simple cloud parameterization (Burrows *et al.*, 2006); summarized in Table 2.1. All of our molecular and alkali cross-sections are those of Freedman *et al.* (2008, 2014). We have also implemented new Na and K cross-sections from Allard *et al.* (2016) but found no substantial change to our retrieved abundances.

One aspect to re-iterate is that we neglect scattering, which may break down in the presence of strongly forward-scattering clouds. Part II did not find any strong evidence for the presence of optically thick clouds in the late-T dwarf sample, as expected for cooler brown dwarfs (e.g. Kirkpatrick, 2005), though the alkali depletion trend was consistent with the expected trend in the Na_2S and KCl condensation-temperature profile intersections. Y-dwarfs are cooler than late T-dwarfs, permitting

the possible formation of water-ice clouds at low pressures (Morley *et al.*, 2014), though we note that the presence of water clouds would have minimal impact over the 1.0-1.7μm wavelength range covered by WFC3 (see Figure 16b of Morley *et al.*, 2018).

At the WFC3 spectral resolution (R$\sim$140) and signal-to-noise ratio (J-band SNR $\sim$ 20), the alkalis' overall spectral signal, if present, is blended together to create a continuum-like absorption feature along the red portion of the Y-band due to the broad wings of the 0.59 and 0.77μm resonance lines, and weak features at 1.24μm in the J-band. As was done in Parts I & II, we have combined their signatures and kept the [Na/K] fixed to the solar ratio for this reason. We have experimented with relaxing this assumption and allowing both Na and K to be retrieved independently, but find no substantial difference in our results.

To solve the parameter estimation problem we use the affine-invariant MCMC sampler `emcee` (Foreman-Mackey *et al.*, 2013), initialized using a grid-model profile TP profile from Marley *et al.* (1996) interpolated to our 15 level parameterization. We choose an approximate $T_{\rm eff}$ and gravity for each object based on the spectral type from Schneider *et al.* (2015) and approximate thermochemical equilibrium abundances for a representative pressure. As in Parts I & II, we have checked that our MCMC chains have converged (typically 40-60K iterations with 200 walkers) and that our results are not sensitive to the initial starting conditions for our model.

2.4 Dataset

In both Parts I & II, ground-based near-IR spectra from the SpeX Prism Library (Burgasser, 2014) were used. As our aim is to extend into the cooler Y dwarf regime, we turn to space-based spectroscopy in order to have comparable SNR on cooler targets. Our chosen dataset are the 6 late-T and 16 early-Y objects observed in

Schneider *et al.* (2015) with HST's WFC3, which details the WFC3 data reduction process. This sample was chosen as it provides the most complete, uniformly reduced spectra of the known Y dwarfs.

For all of our targets we have used the most recent distance estimates available in the literature (Martin *et al.*, 2018; Kirkpatrick *et al.*, 2019). We have also done an analysis assuming parallax estimates from several other authors, the results of which are presented in Section 2.5.2 (Dupuy and Liu, 2012; Luhman and Esplin, 2016; Smart *et al.*, 2017).

We first performed an initial retrieval on all 22 of our targets. While the retrieval technique obtains constraints on various atmospheric parameters, it is ultimately a data-driven technique which requires precise spectroscopy to properly converge. We found that 8 of our 22 targets had low enough SNR to prevent our retrieval model from converging upon physically-realistic TP profiles, and thus have not included them in our analysis.

A brief review the remaining 14 objects, specified by their Wide-field Infrared Survey Explorer (WISE) identification, is provided below. Key observational quantities (YJH magnitudes and distance estimates) are summarized in Table 2.2. Synthetic photometry is from Schneider *et al.* (2015). Distance estimates are from Martin *et al.* (2018); Kirkpatrick *et al.* (2019).

Table 2.2: Basic Photometric Properties of Our Sample

WISE/AllWISE Name	Spec. Type	Y_{MKO} [mag]	J_{MKO} [mag]	H_{MKO} [mag]	Dist. [pc]
WISEA J032504.52-504403.0	T8	19.980±0.027	18.935±0.024	19.423±0.027	27.2±2.2.
WISEA J040443.50-642030.0	T9	20.328±0.032	19.647±0.025	19.970±0.033	21.9±1.4
WISEA J221216.27-693121.6	T9	20.282±0.023	19.737±0.024	20.225±0.036	12.2±0.4
WISEA J033515.07+431044.7	T9	20.166±0.029	19.467±0.023	19.938±0.031	13.9±0.5
WISEA J094306.00+360723.3	T9.5	...	19.766±0.025	20.315±0.038	10.7±0.3
WISEA J154214.00+223005.2	T9.5	20.461±0.028	19.937±0.026	20.520±0.045	11.6±0.6
WISEA J041022.75+150247.9	Y0	...	19.325±0.024	19.897±0.038	6.52±0.17
WISEA J073444.03-715743.8	Y0	20.870±0.041	20.354±0.029	21.069±0.071	15.1±1.2
WISEA J173835.52+273258.8	Y0	...	19.546±0.023	20.246±0.031	7.34±0.22
WISEA J205628.88+145953.6	Y0	...	19.129±0.022	19.643±0.026	7.23±0.20
WISEA J222055.34-362817.5	Y0	20.899±0.034	20.447±0.025	20.858±0.035	11.9±0.75
WISEA J163940.84-684739.4	Y0 Pec.	20.833±0.023	20.626±0.023	20.764±0.029	4.39±0.10
WISEA J140518.32+553421.3	Y0.5	21.33±0.057	21.061±0.035	21.501±0.073	6.76±0.49
WISE J154151.65-225024.9	Y1	20.461±0.028	19.934±0.026	20.520±0.045	5.98±0.14

WISEA J032504.52-504403.0 (W0325, T8): This is one of several new brown dwarf discoveries from Schneider *et al.* (2015). The object spectroscopically well-matches the T8 spectral standard (Burgasser *et al.*, 2006a). Follow-up work was done by Leggett *et al.* (2017) who published an archival J band magnitude.

WISEA J040443.50-642030.0 (W0404, T9): This is another new discovery from Schneider *et al.* (2015) who found the spectrum to closely match the T9 spectral standard (Cushing *et al.*, 2011).

WISEA J221216.27-693121.6 (W2212, T9): Another discovery of Schneider *et al.* (2015) which is also in good agreement with the T9 spectral standard.

WISEA J033515.07+431044.7 (W0335, T9): This object was discovered in the Mace *et al.* (2013) study along with 86 other T dwarfs and given the classification of T9. Both Beichman *et al.* (2014) and Schneider *et al.* (2015) found good agreement with this classification. Leggett *et al.* (2015) published new ground-based YJHK photometry from Gemini Observatory for this target and noted an unusually faint K-band measurement with respect to their other T dwarfs. They found that current equilibrium models could not well-explain their photometric measurements unless the assumed NH_3 abundance was halved and/or there were systematic issues with the CH_4 linelist. Leggett *et al.* (2017) used archival photometry combined with non-equilibrium models from Tremblin *et al.* (2015) to conclude that this target may have sub-solar metallicity.

WISEA J094306.00+360723.3 (W0943, T9.5): W0943 was initially discovered in Cushing *et al.* (2014) who published WISE and Hubble photometry along with WFC3 G141 spectroscopy. It was given a classification of T9.5 which agree well with the results from Schneider *et al.* (2015).

WISEA J154214.00+223005.2 (W1542, T9.5): W1542 was also discovered in the Mace *et al.* (2013) study and given the classification of T9.5 which is in agree-

ment with other similar studies (Beichman *et al.*, 2014; Schneider *et al.*, 2015).

WISEA J041022.75+150247.9 (W0410, Y0): This is a well studied object that was part of the initial classification of Y dwarfs as distinct from their T dwarf counterparts (Cushing *et al.*, 2011). These measurements helped establish the extreme blue shift of Y-J colors across the T/Y transition (e.g. Liu *et al.*, 2012; Kirkpatrick *et al.*, 2012). Cushing *et al.* (2014) obtained the first space-based spectrum of this object and confirmed Y0 classification. Leggett *et al.* (2013) found that fitting YJHK photometry from the Near-Infrared Imager on Gemini North with cloudy models from Morley *et al.* (2012) results in effective temperatures, gravities, and low cloud sedimentation efficiencies consistent with previous analyses of early-Y dwarfs. Spectra from Schneider *et al.* (2015) agree well with the photometry of Leggett *et al.* (2013). Leggett *et al.* (2015) highlighted that current equilibrium models were unable to reproduce their updated photometry for early-Y dwarfs and that retrieval techniques are needed to understand these objects. Leggett *et al.* (2017) visually fit the spectra of Schneider *et al.* (2015) with cloud-free, vertical disequilibrium models from Tremblin *et al.* (2015) and found that while Y and H band are visually well-fit, the J-band model spectrum was $\sim$20% brighter.

WISEA J073444.03-715743.8 (W0734, Y0): This is another object initially discovered by an early WISE Survey (Kirkpatrick *et al.*, 2012). Follow-up photometric work by both Tinney *et al.* (2014) and Leggett *et al.* (2015) noted the rather red Y-J color for this object, more consistent with a late-T than an early-Y dwarf.

WISEA J173835.52+273258.8 (W1738, Y0): This object is probably one of the most well-studied cool brown dwarfs as it represents the Y0 spectral standard (Cushing *et al.*, 2011). Saumon *et al.* (2012) introduced updated collisionally induced H_2 and NH_3 opacities and found improved fits to observed infrared colors. Lodieu *et al.* (2013) provided Z-band imaging of this and several other cool brown

dwarfs. Leggett *et al.* (2013) noted the rather blue Y-J colors now seen in many Y dwarfs. Rajan *et al.* (2015) performed the first photometric monitoring of such a cool target, however this object proved too faint to provide the precision needed to confirm variability in the J-band. Recent ground-based spectra have revealed that non-equilibrium models from Tremblin *et al.* (2015) better-fit the entire near-infrared spectrum of this object, however a majority of the Y-band is not well fit (Leggett *et al.*, 2016b). Leggett *et al.* (2016a) found a peak-to-peak 3% Spitzer [4.5] variability consistent with W1738's rotation period of roughly 6hrs.

WISEA J205628.88+145953.6 (W2056, Y0): W2056 represents another archetypal WISE early-Y dwarf also analyzed in the Cushing *et al.* (2011) and Kirkpatrick *et al.* (2012) studies. Leggett *et al.* (2013) obtained ground-based YJHK photometry and far-red spectra for this object. They noted that overall, cloudy models from Morley *et al.* (2012) fit both the red spectra and K band well but were too faint near 1.0, 1.5, and 1.65μm. This was attributed to both overly-strong NH_3 absorption due to vertical mixing of NH_3 not being included in the models, and incomplete CH_4 molecular line lists. Leggett *et al.* (2017) provided new ground-based M' observations for this object, and visually fit cloud-free models from Tremblin *et al.* (2015) to archival WFC3 spectra. Due to poor S/N and sparse sampling in their grid model, the archival WFC3 spectra were fit only by-eye.

WISEA J222055.34-362817.5 (W2220, Y0): W2220 was initially discovered in the Kirkpatrick *et al.* (2012) study as a new Y dwarf. Chosen as part of a astrometric survey, Beichman *et al.* (2014) noted that W2220 provided tentative evidence for variability due to more than a magnitude difference between archival J and H-band measurements. Leggett *et al.* (2017) concluded this object is consistent with a solar-metallicity and solar-age field dwarf.

WISEA J163940.84-684739.4 (W1639, Y0 Pec.): W1639 was first discovered

by Tinney *et al.* (2012) after carefully resolving the near-infrared counterpart to the WISE point source with ground-based imagining. Though J-band spectroscopy matches well to the Y0 standard, both Y-band spectra and Y-J colors deviate from the standard, leading to the Y0-Peculiar classification (Schneider *et al.*, 2015). Opitz *et al.* (2016) searched for, but found no evidence of another companion to the known Y dwarf to within 2AU. Leggett *et al.* (2017) found that while their non-equilibrium models matched T_{eff} estimates from Schneider *et al.* (2015), the non-equilibrium models resulted in a significantly lower gravity for this object.

WISEA J140518.32+553421.3 (W1405, Y0.5): W1405 is an early-Y dwarf that was identified by a methane-induced H-band feature (Kirkpatrick *et al.*, 2011; Cushing *et al.*, 2011). Morley *et al.* (2012) obtained ground-based YJH photometry in order to compare with a suite of models which incorporated various condensates including several sulfides, KCl, and Cr. They found that these models better fit near-infrared data better than completely cloud-free models. Using updated YJHK photometry, Leggett *et al.* (2013) found that this object should be cool enough to display effects from the presence of water clouds, but their model grid did not extend down to cool enough temperatures for a reliable water-cloud model fit. Lodieu *et al.* (2013) obtained lower-limit z-band measurements for this dim object. Schneider *et al.* (2015) reclassified this object as Y0.5 due to its J-band spectroscopy being narrower than the Y0 spectral standard. Cushing *et al.* (2016) obtained Spitzer 3.6 and $4.5\mu m$ light curves and found the first evidence for variability in a Y dwarf with 3.6% variability detected with an 8.2hr period. Leggett *et al.* (2017) found this object to also be consistent with solar metallicity and age.

WISE J154151.65-225024.9 (W1541, Y1): W1541 is the latest-type Y dwarf we have analyzed which was re-classified as Y1 based upon the width of J-band spectroscopic measurements (Schneider *et al.*, 2015). This object is another Y dwarf part

of the initial WISE discovery papers (Kirkpatrick *et al.*, 2011; Cushing *et al.*, 2011; Kirkpatrick *et al.*, 2012). Morley *et al.* (2012) obtained ground-based Y and J-band photometry of this object where they note that their cloudy, rather than cloud-free models better reproduce the observed colors of their Y dwarf photometry. However, Saumon *et al.* (2012) noted that with improved NH_3 opacities, their cloud-free models well-matched the observed colors. Ground-based YJHK photometry was obtained by Leggett *et al.* (2013) who's cloud-free models estimate T_{eff} ∼325K. Leggett *et al.* (2015) obtained improved H-band measurements and compared measured colors with a suite of both water-cloud and cloud-free models. Though they find that the inclusion of water-clouds do better-fit several colors, there are still magnitude-scale systematic offsets between the models and data. Leggett *et al.* (2017) was able to successfully reproduce either Y or J-band spectroscopy but a simultaneous fit to the entire YJH spectrum could not be obtained.

2.5 Results

Here we present our results from the analysis of our 14 late-T/early-Y dwarfs. Full posteriors of all model parameters are available in the online copy of this work. Figure 2.1 summarizes the fits with the WFC3 data in black, best-fit spectra in blue, and residuals in red. Several objects only have 1.1-1.7μm coverage as full YJK coverage requires both G105 and G141 spectra from HST (Schneider *et al.*, 2015). From visual inspection, there is no systematic structure in the residuals and most of our objects have a χ^2_ν between 1 and 3. W2056 has a higher χ^2_ν=5.05 but this is due to an oversubtraction artifact with fluxes between the J and H bands being well below 0 by $\sim 2\sigma$. We have experimented with removing such data from our fit, but found it to not impact our results (see Section 2.5.2).

We first discuss the implications of our constraints on the temperature structure

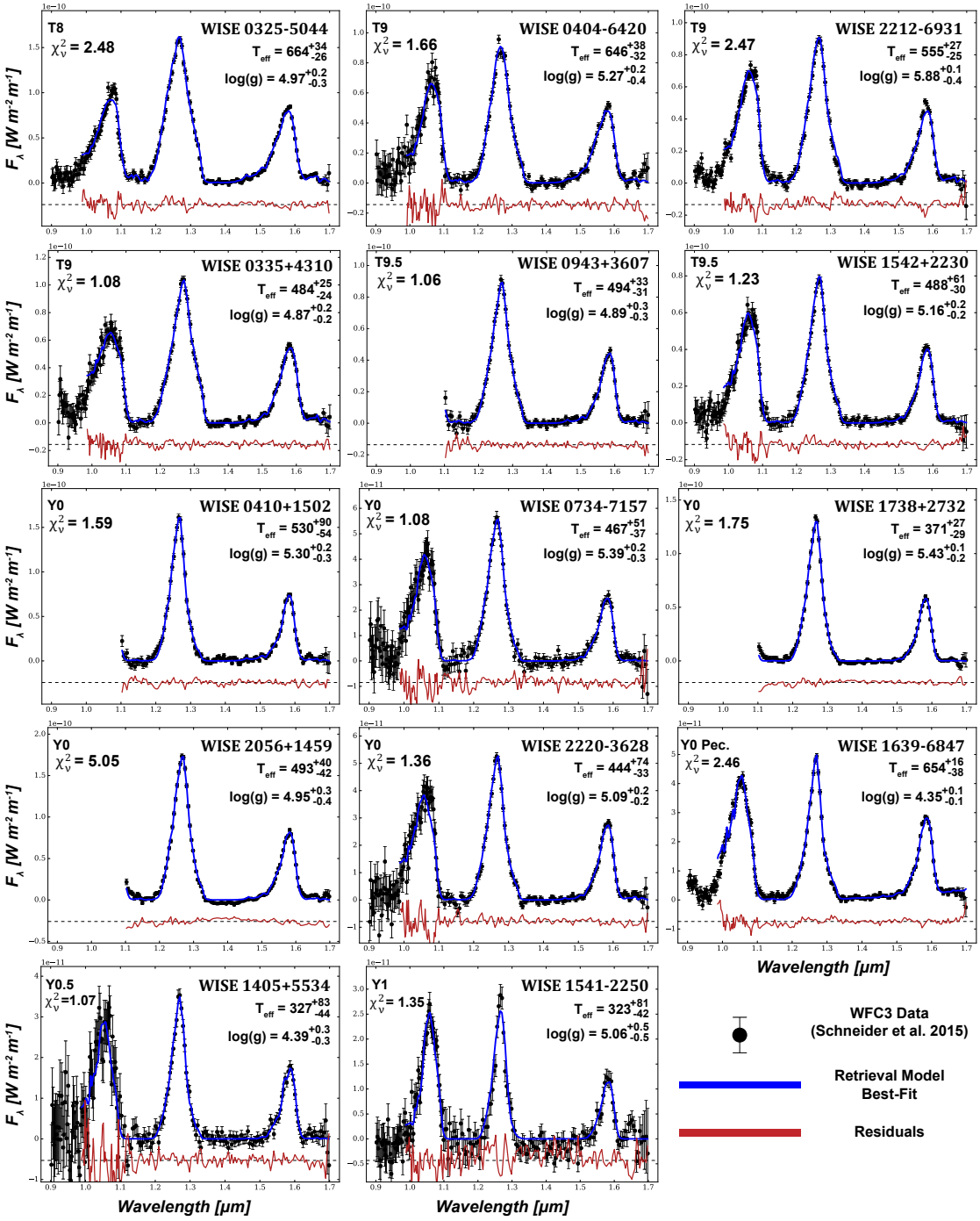

Figure 2.1: WFC3 observations (black points), best-fit retrieval model (blue), and residuals (lower, red) for the WFC3 sample sorted by the Schneider *et al.* (2015) spectral classification (upper left). The retrieved log(g) [cgs] and derived effective temperature [K] are given in the upper right hand corner of each panel.

and evolutionary properties of these objects. Our retrieved evolutionary parameters are enumerated in Table 2.3. We then highlight our retrieved abundances which are listed in Table 2.4. Finally we discuss how observations of these objects with JWST will impact our ability to characterize these objects.

2.5.1 Vertical Temperature Structure

For any non-irradiated sub-stellar object, the energy balance, and hence thermal structure of the atmosphere, is governed by the flow of internal heat flux through the atmosphere, controlled by the gravity and atmospheric opacity. These properties are directly set by both the mass and age of the system (e.g. Allard *et al.*, 1996). In ultra cool dwarfs, energy is primarily transported through radiation and convection (Marley and Robinson, 2015).

Late-T/early-Y type objects are ideal for the characterization of the TP profile structure due to the high degree of spectral modulation (which maps to a wide range of probed pressures) and the presumed lack of optically thick clouds (Morley *et al.*, 2012). As before, we make few a priori assumptions regarding the thermal structure of the atmosphere, and instead allow the observations to drive the solutions. By then making comparisons between our results, and those of self-consistent models, we can then investigate where "atypical" atmospheric processes, such as deviations from radiative-convective equilibrium, may be occurring. Should any significant deviations be found, such information can be utilized in order to improve grid-based models' treatment of atmospheric structure by inclusion of other possible sources of heating. (e.g. Sorahana *et al.*, 2014; Tremblin *et al.*, 2015).

Figure 2.2 summarizes the resulting TP profiles. The median TP profile is shown in black, with 1σ and 2σ confidence intervals outlined in red. Overlaid on top of the retrieval results are radiative-convective equilibrium profiles (blue) derived using the

ScCHIMERA modeling tool described in Piskorz *et al.* (2018) and Bonnefoy *et al.* (2018), generated using the T_{eff} and log(g) range derived from the retrieval results. We compute the effective temperature as in Parts I and II by numerically integrating for the bolometric flux of the retrieved spectral spread for each object from 1 - 20 μm. Contribution functions (grey) from the WFC3 observations are also overlaid which can be treated as the effective photosphere probed by WFC3. As was noted in Part II, we reiterate that the atmospheric structure above and below these regions is largely driven by our TP profile smoothing parameter (described in Part I), and that interpretation of such structure should be done with caution.

The WFC3 observations probe pressures from roughly 1-100 bars with typical 1σ temperature uncertainties of $\sim$50-100 K, consistent with the SpeX T-dwarfs from Part II. For a large majority of objects, the retrieved structures appear consistent with the assumption of radiative-convective equilibrium. Though true for a large majority of objects, W1639 stands out in stark contrast. The retrieved TP profile shows almost no consistency with that of radiative-convective equilibrium, as well as an interesting "kink" structure at roughly 10bars. The unique atmospheric structure also suggests our WFC3 wavelengths are sensitive to much lower pressures of roughly 0.1-0.01bars.

WISEA J1639-6847

W1639 is the only object in our sample with a classification of "Y0: Peculiar" (Schneider *et al.*, 2015). Though the object's J-band spectra well-match the Y0 spectral standard, the overall Y-J color is significantly bluer due to a bright Y-band. Additionally, the overall position of the Y-band is significantly blue-shifted when compared to the T9 spectral standard. These features, remarked upon by Schneider *et al.* (2015) are not just an artifact of the WFC3 data, as the bright Y-band has also been observed with the ground-based FIRE instrument (Tinney *et al.*, 2012). These unique prop-

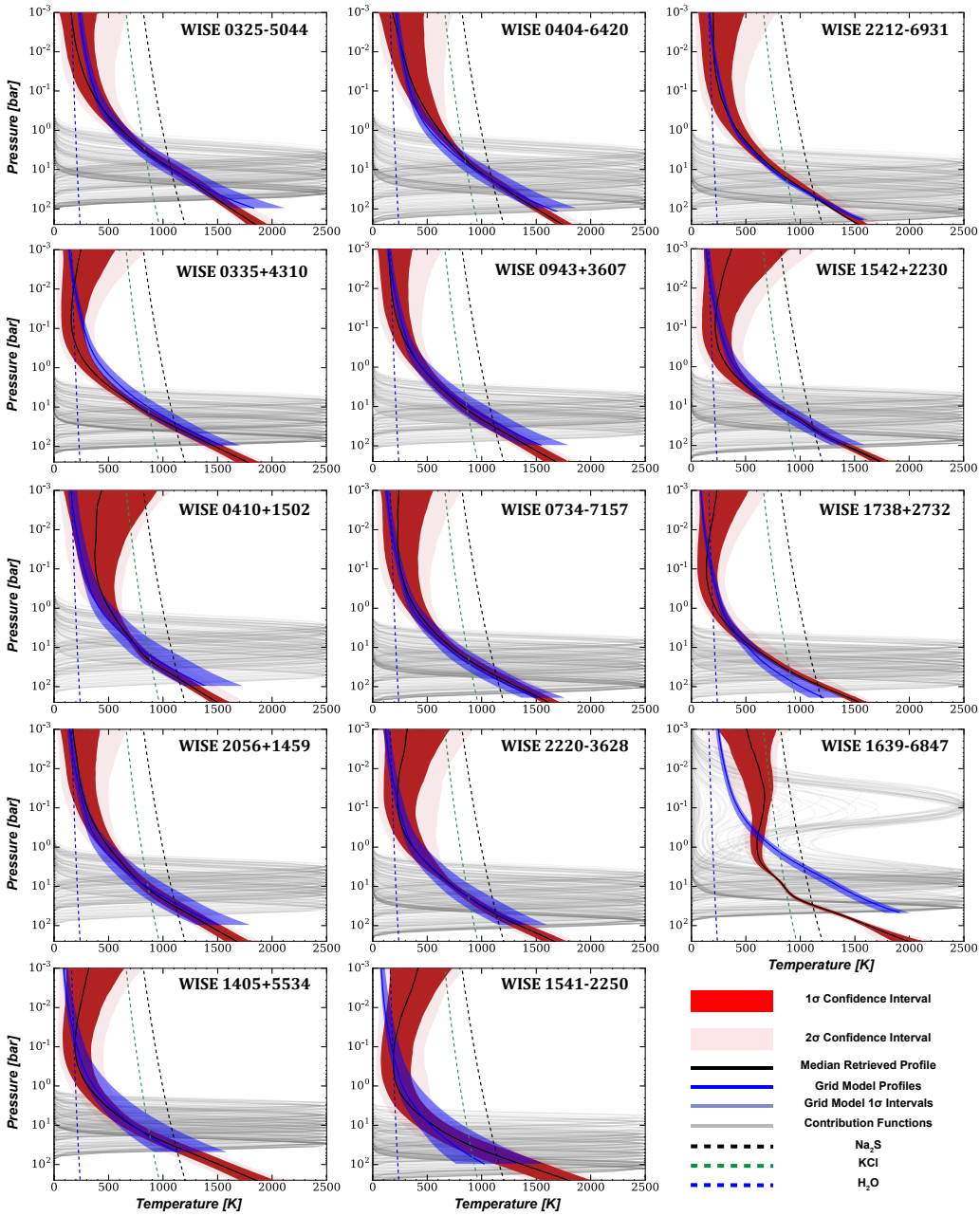

Figure 2.2: Retrieved TP profiles for all targets. Black lines are median values with red 1σ and 2σ confidence intervals. In grey are the contribution functions of the atmosphere from the WFC3 observations and can be thought of as the effective photosphere. Overlaid (blue) are solar-composition radiative-convective equilibrium profile spreads derived from the retrieved spread in effective temperature and gravity. Finally we also include solar-composition equilibrium condensation curves (dashed lines) for several important species (Morley *et al.*, 2012, 2014).

erties motivated Schneider *et al.* (2015) to invest more of their limited WFC3 time to this object, resulting in much better Y-band constraints than the other objects in our sample (see Figure 2.1) and are the main contributor for the improved TP profile constraints relative to our other objects. Though the W1639 spectrum seems well-fit by our model (reduced χ^2 of $\sim$2) there are several lingering issues with the resulting best-fit parameters.

First is that, despite the object being in the Y0 Pec. classification, we derive an effective temperature of 654^{+16}_{-38}K. There has been a suggestion that double-diffusive convection can result in much shallower thermal structures than predicted by equilibrium grid models (Tremblin *et al.*, 2015). This would be consistent with the profile we retrieve for W1639. However, using basic energy balance arguments and thermodynamics, Leconte (2018) demonstrated that this mechanism would result in *steeper*, not shallower, temperature gradients, in contrast to Tremblin *et al.* (2015) and the profile of W1639. Release of latent heat due to condensation of various cloud species may also result in shallower adiabats. However Figure 2.2 shows that the main contributor to such heat, water, would negligibly impact our objects based on the intersection of the retrieved TP profile with water's equilibrium condensation curve.

Additionally, our estimate for log(g) is the lowest out of our 11 objects at log(g) = $4.35^{+0.1}_{-0.1}$ requiring a radius of R=$0.4^{+0.03}_{-0.02}$R$_{\rm Jup}$ and M=$1.5^{+0.3}_{-0.3}$M$_{\rm Jup}$ (see Section 2.5.2, Table 2.3). These constraints are significantly smaller than allowed by typical field dwarfs and, combined with the peculiar TP profile, leads us to conclude that our data-driven retrieval model may not be well-suited to explain the physical characteristics of this single unique object. However we reiterate that the remaining object's TP profiles seem to agree well with assumptions of radiative-convective equilibrium.

2.5.2 Effective Temperature, Gravity, Radius, & Mass

The effective temperature, gravity, and thus radius, and mass are diagnostic of brown dwarf evolutionary history (e.g. Burrows *et al.*, 2001; Baraffe *et al.*, 2003; Saumon and Marley, 2008). Evolution models suggest that our late-T ($\geq$T8) and early-Y ($\leq$Y1) sample, should have T_{eff}'s from 800-350K (Pecaut and Mamajek, 2013). Field-age late-T and early-Y dwarfs are expected to have log(g)$\approx$5 with a relatively strong upper bound at log(g)$\approx$5.3 for even the oldest and coldest brown dwarfs possible (e.g Saumon and Marley, 2008). Field-aged objects over the 10 - 80 M_{Jup} range are expected to have radii within $\sim$20% of Jupiter's.

In this work, the total $(R/D)^2$ scaling factor is a free parameter. By using constraints on the distance D from the literature and our retrieved constraints on $(R/D)^2$, we are then able to *derive* constraints on the photometric radius R. Using this *derived* constraint, with our retrieved log(g), we can then derive the total mass of the object M, with a prior upper limit of $80M_{Jup}$. Table 2.3 and Figure 2.3 summarize the retrieved and derived estimates for these evolutionary parameters under two sets of model assumptions.

Free Retrieval

We first focus on our a less constrained, "free" retrieval, which only incorporates the $80M_{Jup}$ mass prior upper limit, as has been done in Parts I and II. Our retrieved log(g) and derived T_{eff} for this case are shown as red symbols in Figure 2.3. In general we find that the uncertainties in both log(g) and T_{eff} are consistent with the results from Part II with 1σ errors between 0.1-0.5 dex and 30-90K respectively. This is encouraging as both our dataset in this work, and the dataset in Part II had comparable SNR on the observed spectra. For a majority of objects, our derived effective temperatures

Table 2.3: Retrieved & Derived Evolutionary Parameters

WISE/ALLWISE Name	Spec. Type	T_{eff} [K]	log(g) [cgs]	R [R_{Jup}]	Mass [M_{Jup}]	Priors
WISEA J032504.52-504403.0	T8	664^{+34}_{-26}	$4.97^{+0.19}_{-0.30}$	$1.08^{+0.11}_{-0.11}$	44^{+24}_{-23}	Free
		660^{+29}_{-24}	$5.06^{+0.27}_{-0.36}$	$1.10^{+0.11}_{-0.10}$	56^{+46}_{-32}	Constrained
WISEA J040443.50-642030.0	T9	646^{+38}_{-32}	$5.27^{+0.18}_{-0.30}$	$0.78^{+0.06}_{-0.06}$	47^{+22}_{-24}	Free
		639^{+37}_{-30}	$5.20^{+0.22}_{-0.43}$	$0.81^{+0.06}_{-0.06}$	42^{+24}_{-25}	Constrained
WISEA J221216.27-693121.6	T9	555^{+27}_{-25}	$5.88^{+0.08}_{-0.35}$	$0.47^{+0.05}_{-0.03}$	69^{+8}_{-34}	Free
		540^{+40}_{-32}	$5.25^{+0.16}_{-0.29}$	$0.71^{+0.02}_{-0.02}$	36^{+16}_{-17}	Constrained
WISEA J033515.07+431044.7	T9	484^{+25}_{-24}	$4.87^{+0.22}_{-0.22}$	$0.87^{+0.06}_{-0.06}$	23^{+15}_{-10}	Free
		483^{+24}_{-25}	$4.87^{+0.23}_{-0.21}$	$0.88^{+0.06}_{-0.06}$	23^{+14}_{-9}	Constrained
WISEA J094306.00+360723.3	T9.5	494^{+33}_{-31}	$4.89^{+0.30}_{-0.31}$	$0.70^{+0.07}_{-0.07}$	15^{+15}_{-8}	Free
		494^{+36}_{-36}	$4.86^{+0.30}_{-0.30}$	$0.75^{+0.07}_{-0.06}$	16^{+17}_{-8}	Constrained
WISEA J154214.00+223005.2	T9.5	488^{+60}_{-30}	$5.16^{+0.15}_{-0.18}$	$0.61^{+0.05}_{-0.05}$	21^{+11}_{-8}	Free
		484^{+39}_{-26}	$5.07^{+0.16}_{-0.26}$	$0.71^{+0.05}_{-0.04}$	23^{+12}_{-10}	Constrained
WISEA J041022.75+150247.9	Y0	530^{+90}_{-54}	$5.30^{+0.23}_{-0.32}$	$0.73^{+0.10}_{-0.08}$	43^{+24}_{-21}	Free
		529^{+83}_{-86}	$5.06^{+0.29}_{-0.59}$	$0.75^{+0.07}_{-0.04}$	27^{+24}_{-13}	Constrained
WISEA J073444.03-715743.8	Y0	467^{+51}_{-37}	$5.39^{+0.17}_{-0.28}$	$0.71^{+0.07}_{-0.07}$	50^{+21}_{-23}	Free
		456^{+50}_{-34}	$5.24^{+0.18}_{-0.33}$	$0.77^{+0.77}_{-0.05}$	42^{+22}_{-22}	Constrained
WISEA J173835.52+273258.8	Y0	371^{+27}_{-29}	$5.43^{+0.13}_{-0.17}$	$0.71^{+0.05}_{-0.05}$	59^{+15}_{-22}	Free
		371^{+33}_{-30}	$5.20^{+0.2}_{-0.29}$	$0.73^{+0.04}_{-0.03}$	34^{+20}_{-17}	Constrained
WISEA J205628.88+145953.6	Y0	493^{+40}_{-42}	$4.95^{+0.31}_{-0.35}$	$0.67^{+0.07}_{-0.05}$	16^{+15}_{-8}	Free
		485^{+38}_{-38}	$4.93^{+0.25}_{-0.29}$	$0.72^{+0.03}_{-0.02}$	18^{+14}_{-9}	Constrained
WISEA J222055.34-362817.5	Y0	444^{+74}_{-33}	$5.09^{+0.24}_{-0.23}$	$0.72^{+0.08}_{-0.07}$	26^{+21}_{-9}	Free
		449^{+57}_{-35}	$5.07^{+0.16}_{-0.26}$	$0.74^{+0.07}_{-0.07}$	26^{+13}_{-12}	Constrained
WISEA J163940.84-684739.4	Y0 Pec.	654^{+16}_{-38}	$4.35^{+0.09}_{-0.08}$	$0.40^{+0.03}_{-0.02}$	$1.5^{+0.3}_{-0.3}$	Free
		-	-	-	-	Constrained
WISEA J140518.32+553421.3	Y0.5	327^{+83}_{-44}	$4.39^{+0.28}_{-0.31}$	$0.66^{+0.12}_{-0.09}$	$4.4^{+3.9}_{-2.1}$	Free
		338^{+98}_{-58}	$3.89^{+0.22}_{-0.15}$	$0.75^{+0.08}_{-0.06}$	$1.7^{+1.4}_{-0.5}$	Constrained
WISE J154151.65-225024.9	Y1	323^{+81}_{-42}	$5.06^{+0.50}_{-0.48}$	$0.33^{+0.07}_{-0.05}$	$5.4^{+9.7}_{-3.4}$	Free
		389^{+85}_{-87}	$3.91^{+0.33}_{-0.19}$	$0.72^{+0.04}_{-0.02}$	$1.7^{+2.0}_{-0.6}$	Constrained

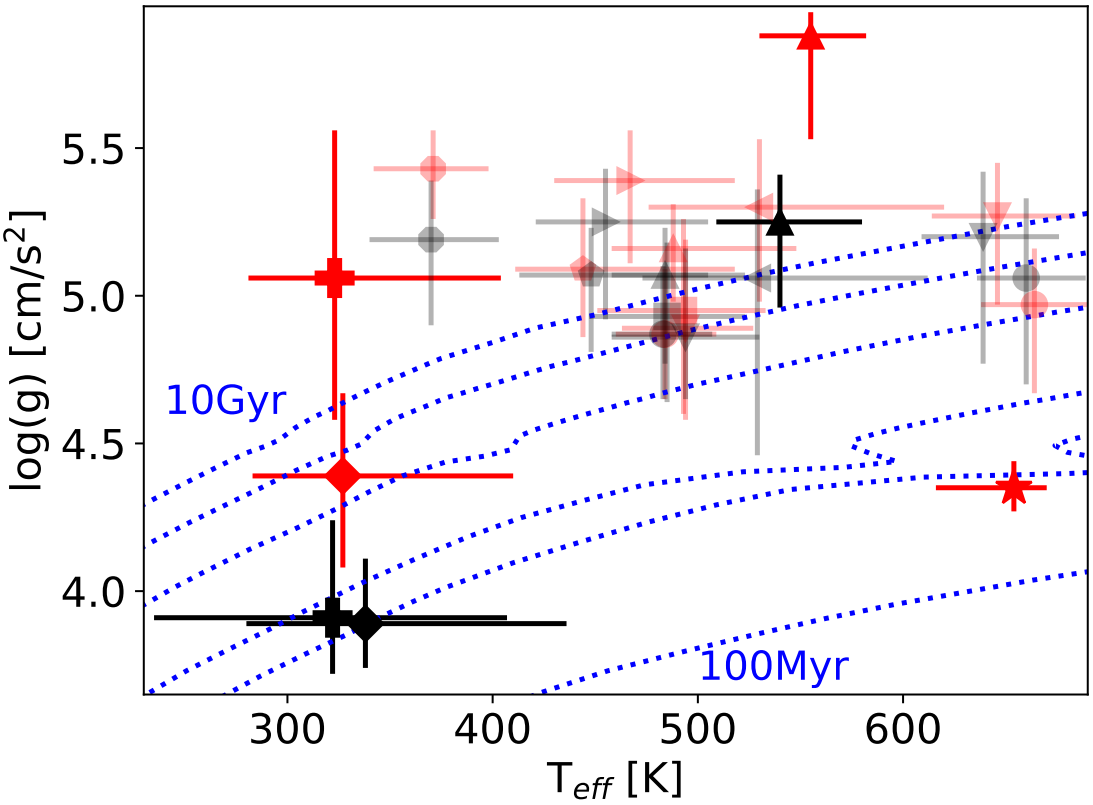

Figure 2.3: T_{eff} and log(g) 1σ constraints for our free retrieval results (red) and constrained retrieval (black). Each object has its own unique symbol. Most objects, save the coldest two (W1405,W1541) and W1639 (see text) show consistent results between the free and constrained retrievals at 1σ. Evolutionary trends from Marley et al. (2019, in prep.) with constant age (blue dotted) are overlaid for context at 100Myr, 600Myr, 1Gyr, 3Gyr, 6Gyr, and 10Gyr.

agree with the spectral types given in Schneider *et al.* (2015) when compared to the table provided in Pecaut and Mamajek (2013). The notable exception to this trend is W1639 whose unique TP profile is discussed in Section 2.5.1.

Overplotted on Figure 2.3 are curves of constant age (blue,dashed) from the upcoming Sonora grid of evolutionary models (Marley et al. 2019, in prep.). Several objects appear to have gravities that extend well beyond those anticipated by the 10Gyr curve, though our retrieved uncertainties are large enough to be consistent with the oldest models at $\sim 2\sigma$. This result is not unique to our retrieval approach as

Schneider *et al.* (2015) also noted that grid-model comparisons resulted in a similar result with several object's log(g) estimates requiring gravity values higher than computed in their grid model. In addition to high gravity estimates, we also found several objects to have smaller radii than expected for our late-T, early-Y sample with several objects below a lower limit value of $\sim 0.7 R_{Jup}$ (Saumon and Marley, 2008). Both the uncomfortably high gravities and small radii prompted us to explore the robustness of our results through a battery of tests.

We first investigated the possibility of an unknown systematic error in the observed spectra biasing the fits. We considered this as it was noticed that the observed fluxes fell below 0, well outside of the reported 1-sigma uncertainties in some cases, in the deep absorption bands for several objects (namely W2056, W2220, W1541, see Figure 2.1). This is due to oversubtraction when attempting to remove background fluctuations. To test this we introduced a free parameter to uniformly shift the model spectra fluxes to within the 1σ error estimates of the data, but found that it did not produce any considerable change in parameter estimates.

Next we explored some of the key assumptions made within our model. In this initial set of "free" retrievals we had assumed a hard prior upper limit of $80 M_{Jup}$ on the mass. This prior rejects combinations of radii and gravities that would exceed this mass limit. We tested the sensitivity of our results to this mass upper limit by effectively removing the prior. These resulted in significantly higher retrieved gravities with some objects such as W1738 reaching as high as $\log(g)=5.7^{+0.18}_{-0.32}$. This indicated to us that the data was indeed favoring higher masses and gravities along with lower radii.

We then explored how radius assumptions (through $(R/D)^2$–assuming a distance) could influence the retrievals by fixing the radii to a realistic $0.9 R_{Jup}$ (and turning the mass upper limit prior back on). For the case of W0734 (originally retrieved

R$\sim$0.71R$_{\rm Jup}$, log(g)=$5.39^{+0.17}_{-0.28}$), we found that the fixed radius resulted in a decreased gravity (log(g)=$5.12^{+0.2}_{-0.33}$). However, the resulting marginalized posterior is highly non-Gaussian due to the enforcement of the 80M$_{\rm Jup}$ cutoff. This suggests that, despite enforcing these priors, the high-gravity solution is still favored.

Constrained Retrieval

We finally decided to run a completely separate set of retrievals on all of our objects with more stringent priors based on results from evolutionary models that we have labeled as "constrained" retrievals. This included restricting 0.7R$_{\rm Jup}$ <R<2.0R$_{\rm Jup}$, 3.5<log(g)<5.5, and effectively removing the mass upper limit. The results of this analysis are shown as black symbols in Figure 2.3 and are enumerated in Table 2.3. Objects whose "constrained" retrieval results are within 1σ of the "free" retrieval are translucent, while those who log(g) change by $> 1\sigma$ are opaque.

We obtained two key results from this constrained retrieval test. First is that, regardless of our priors on evolutionary parameters, the data suggest that these objects have anomalously high gravity estimates. This can be seen in Figure 2.3 where most objects still lie above the 10Gyr trend for both the "constrained" (black) and "free" (red) retrieval. For the Y0 objects, we find a consistent decrease in their log(g) estimates by upwards of 0.3 dex and a slight increase in the radii estimates to roughly 0.75R$_{\rm Jup}$. Though this places our retrieval results in better agreement with evolutionary models, our posterior distributions for log(g) are consistently non-Gaussian, and push against the log(g)=5.5 upper limit, suggesting that the high gravity solution is still favored.

Our second result is that, regardless of our priors on evolutionary parameters, we still obtain the same constraints on our chemical abundances to within 1σ. This was a bit surprising as there is a well-known correlation between the gravity and overall

metallicity for these objects. We ensured this by picking three of our objects with anomalously high gravities (W2212, W0734, W1738) and enforcing that log(g)=5.0. We found that our retrieved metallicity did indeed decrease as expected, however our overall fit to the data was much worse under this assumption, with an average delta χ^2_ν of 6.5, indicating that our original retrieved metallicities and high gravities are the statistically favored solution.

Caveats & Exceptions

There were four objects in total which did not follow these trends which are the opaque points in Figure 2.3. Though W2212 obtains plausible constraints on the mass and $T_{\rm eff}$, it requires a radius of R=$0.47^{+0.05}_{-0.03}$ under the "free" retrieval assumption. Our "constrained" retrieval does result in a more physically realistic R=$0.71^{+0.02}_{-0.02}$, we find that our constraints on the chemical abundances change by $\sim 2\sigma$. We ran a separate retrieval on this target using an different distance estimate from Kirkpatrick *et al.* (2012) where we obtain a physically realistic R=$0.68^{+0.06}_{-0.05}$ and our chemical abundances did not change beyond 1σ though the retrieved gravity is still the largest of our sample at log(g)=$5.5^{+0.11}_{-0.17}$. Full model posteriors for this additional run are available at the linked Zenodo site.

For W1639, our retrieval model could not converge upon a physically realistic TP profile given the assumptions in the constrained retrieval and thus has no corresponding black star in Figure 2.3. For both W1405 and W1541 (diamond and cross respectively) we find that though our retrieval model converges upon solutions for both objects, they are largely nonphysical. By enforcing stronger constraints on the radius, we find that a Jupiter-like mass and significantly lower gravities (by $\sim 2\sigma$) are needed in order to well-match the spectra under these assumptions. Additionally, our constraints on the chemical abundances change by upwards of 3σ. Though we include

these four objects in the results of subsequent sections, we strongly caution against over-interpretation of their chemical abundance constraints given they significantly change under different model assumptions.

The one technique which proved successful in reducing the retrieved gravity of an object without encountering non-Gaussian posteriors or changes in chemical abundances was changing the assumed parallax. Our distance estimates had been taken from two specific sources in the literature (Martin *et al.*, 2018; Kirkpatrick *et al.*, 2019). These were chosen in order to use the most updated parallax estimates from the Spitzer instrument. However, several other campaigns have previously measured parallaxes for several of our targets (e.g. Luhman and Esplin, 2016; Smart *et al.*, 2017). In most cases, the distances proved consistent to our previous assumptions and, as expected, our retrieved parameters remained the same. However using the parallax measurement for W2056 from Smart *et al.* (2017) resulted in a more physically realistic $\log(g)=4.58^{+0.33}_{-0.37}$. Though we did not find similar results for the other distance estimates from Smart *et al.* (2017), we note that this result shows how sensitive our evolutionary parameters are to measured parallaxes. If the distance estimates are systematically biased in a similar fashion this may also account for the fact that our radii estimates are slightly lower than expected from evolutionary models.

2.5.3 Composition

One of the key utilities of retrievals is their ability to directly determine the molecular abundances in an atmosphere, rather than assume them from elemental abundances and equilibrium chemistry. From the molecular abundances we can *derive* the atomic abundance ratios (e.g., metallicity, C/O, N/O etc.), and more importantly, explore trends in these abundances which are diagnostic of atmospheric chemical mechanisms. The primary motivations for looking at molecular abundances

in the Y-dwarf regime are to (1) determine at what temperature the alkali metals completely disappear and if it is consistent with grid-model chemical predictions, and to (2) determine the role of ammonia as it is anticipated to be strongly influenced by disequilibrium vertical mixing. Again, our retrieval forward model assumes constant-with-altitude (pressure) molecular mixing ratios. The retrieved abundances are therefore representative of column integrated abundances over the photosphere probed by WFC3.

Table 2.4 summarizes the molecular abundance constraints (median and 68% confidence interval). All abundances are reported as the log of the volume mixing ratio log(VMR). Items in Table 2.4 without error bounds are 3σ upper limits. We find well defined, bounded constraints for H_2O, CH_4, NH_3, and in two cases Na+K, but obtain only upper limits for CO, CO_2, H_2S, and the alkalies. Upper limits are consistent with a non-detection as shown in Part II. These results are also broadly consistent with expectations from chemical equilibrium predictions as H_2O, CH_4, and NH_3 are expected to be the dominant species where as CO, CO_2, H_2S, and the alkali metals less so (Burrows and Sharp, 1999). Section 2.5.3 highlights trends identified in both NH_3 and alkali metals. First, we discuss the derived bulk atmospheric metallicity and carbon-to-oxygen ratios.

Table 2.4: Retrieved Atmospheric Abundances

WISE/ALLWISE Name	Spec. Type	H_2O	CH_4	CO	CO_2	C/O	H_2S	NH_3	Na+K
WISEA J032504.52-504403.0	T8	$-3.31^{+0.12}_{-0.13}$	$-3.05^{+0.11}_{-0.16}$	-4.1	-3.7	0.99±0.18	-5.0	$-4.49^{+0.12}_{-0.18}$	$-5.52^{+0.09}_{-0.07}$
WISEA J040443.50-642030.0	T9	$-3.01^{+0.11}_{-0.13}$	$-2.74^{+0.10}_{-0.16}$	-3.0	-3.3	1.02±0.16	-5.0	$-4.63^{+0.13}_{-0.20}$	-6.0
WISEA J221216.27-693121.6	T9	$-2.59^{+0.07}_{-0.18}$	$-2.56^{+0.05}_{-0.16}$	-2.9	-3.3	0.79±0.09	-6.8	$-4.05^{+0.08}_{-0.13}$	-5.0
WISEA J033515.07+431044.7	T9	$-3.35^{+0.09}_{-0.09}$	$-3.48^{+0.11}_{-0.11}$	-3.8	-3.9	0.57±0.07	-5.3	$-4.78^{+0.13}_{-0.12}$	$-5.97^{+0.07}_{-0.10}$
WISEA J094306.00+360723.3	T9.5	$-3.35^{+0.14}_{-0.15}$	$-3.13^{+0.17}_{-0.15}$	-3.3	-3.2	1.22±0.25	-5.0	$-4.46^{+0.16}_{-0.16}$	-5.2
WISEA J154214.00+223005.2	T9.5	$-3.04^{+0.09}_{-0.08}$	$-2.92^{+0.08}_{-0.10}$	-4.2	-4.3	0.95±0.15	-6.0	$-4.32^{+0.10}_{-0.12}$	-6.7
WISEA J041022.75+150247.9	Y0	$-2.90^{+0.13}_{-0.15}$	$-2.63^{+0.17}_{-0.19}$	-3.3	-4.1	1.09±0.30	-4.3	$-4.11^{+0.15}_{-0.19}$	-5.0
WISEA J073444.03-715743.8	Y0	$-2.91^{+0.12}_{-0.15}$	$-2.77^{+0.09}_{-0.14}$	-3.4	-3.7	0.78±0.16	-6.0	$-4.29^{+0.10}_{-0.14}$	-6.0
WISEA J173835.52+273258.8	Y0	$-2.87^{+0.08}_{-0.08}$	$-2.75^{+0.12}_{-0.10}$	-3.3	-4.1	0.79±0.23	-5.0	$-4.21^{+0.10}_{-0.09}$	-5.2
WISEA J205628.88+145953.6	Y0	$-3.18^{+0.16}_{-0.15}$	$-2.89^{+0.18}_{-0.17}$	-4.2	-4.4	1.10±0.27	-5.0	$-4.44^{+0.17}_{-0.17}$	-5.5
WISEA J222055.34-362817.5	Y0	$-3.04^{+0.11}_{-0.10}$	$-3.00^{+0.11}_{-0.12}$	-4.2	-4.3	0.62±0.10	-5.8	$-4.19^{+0.08}_{-0.10}$	-6.8
WISEA J163940.84-684739.4	Y0Pec.	$-3.32^{+0.04}_{-0.04}$	$-3.42^{+0.05}_{-0.04}$	-4.3	-4.6	0.46±0.06	-6.3	$-4.72^{+0.05}_{-0.04}$	-7.0
WISEA J140518.32+553421.3	Y0.5	$-3.24^{+0.15}_{-0.13}$	$-3.33^{+0.14}_{-0.16}$	-3.6	-3.8	0.46±0.10	-5.0	$-4.84^{+0.14}_{-0.16}$	-6.0
WISE J154151.65-225024.9	Y1	$-2.68^{+0.26}_{-0.24}$	$-2.80^{+0.26}_{-0.26}$	-3.5	-3.6	0.45±0.17	-5.0	$-4.43^{+0.21}_{-0.23}$	-6.4

Metallicity & C/O

The elemental abundance inventory of a substellar object is important to its evolutionary history as it governs total atmospheric opacity, and hence its cooling rate (Burrows *et al.*, 2001). It is important to understand the elemental abundances in brown dwarfs in order to place them into compositional context with both higher mass stars and lower mass planets.

One would expect the population of field brown dwarfs to have a similar elemental abundance pattern as stars, since both objects are thought to form via fragmentation within a molecular cloud. To contrast this, planets which are formed in protoplanetary disks can undergo migration within that disk. The existence of ice lines and dynamical models of migration have led to a range of predictions regarding planet-mass atmospheric elemental abundances. These can range any where from "stellar composition" to high metallicity (>100×Solar, (e.g. Fortney *et al.*, 2013; Mordasini *et al.*, 2016)) or high carbon-to-oxygen ratios (C/O > 1, (e.g. Öberg *et al.*, 2011; Madhusudhan *et al.*, 2014; Helling *et al.*, 2014; Eistrup *et al.*, 2016)). Identifying at what mass, in general, the diversity in composition substantially increases can ultimately assist us in truly bridging the gap between stars and planets. Since brown dwarfs sit between these mass limits, determining elemental abundances for a large number of substellar objects can help us in bridging this gap.

There are several challenging aspects to brown dwarf elemental abundance determinations. Firstly, at these cooler temperatures the chemical inventory is largely in the form of molecular, rather than elemental species. Molecules have much more complex spectroscopic features than atomic species with broad and deep roto-vibrational bands that overwhelm the spectral continuum; an oft used handle to obtain basic bulk parameters for hotter stars (e.g. Bean *et al.*, 2006). Additionally, some molecular

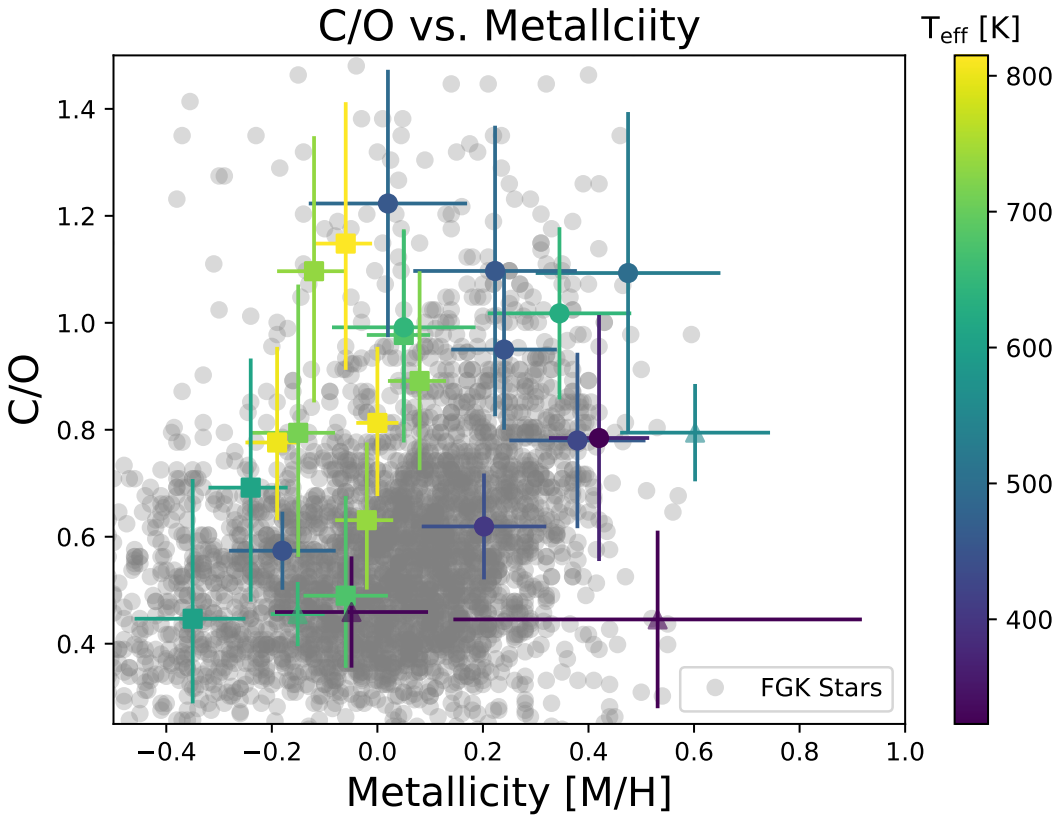

Figure 2.4: Metallicity vs. C/O for our retrieved results (circles) and the results from Part II (squares). Triangles should be interpreted with caution (see text). We also overlay estimates for the local FGK stellar population (grey) for context (Hinkel *et al.*, 2014). Our combined sample of late-T and early-Y dwarfs seem relatively consistent with the local stellar population.

species are thought to be affected by both equilibrium condensate rainout and vertical disequilibrium mixing, while others can retain uniform chemical abundance profiles throughout the atmosphere (e.g. Burrows *et al.*, 2001; Sharp and Burrows, 2007). Therefore, in order to accurately characterize the atmospheres of brown dwarfs, one must include the key molecular components covered over their bandpass, as well as the relevant chemical and dynamical processes which could affect such constituents.

Here, we focus our elemental abundance results on the metallicity and carbon-to-oxygen ratios only, as these are the most readily determinable elemental ratios for objects at these temperatures. Water and methane contain a bulk of the atmospheric

metal content (C and O) for atmospheres cooler than $\leq$1000K.

We determine directly from the retrieved molecular abundances the metallicity and C/O. The metallicity is computed by summing the molecular metal content (e.g., M=H_2O+2CO+3CO_2+NH_3+Na+K+CH_4+H_2S), then dividing by the background hydrogen content (H=2H_2+4CH_4+3NH_3+2H_2O+2H_2S) and finally normalizing by the solar M/H fraction to obtain our final "metallicity" ([M/H] = log((M/H)/(M/H)$_{solar}$)). The C/O is determined dividing the total carbon (CO+CO_2+CH_4) by the total oxygen (H_2O+CO+2CO_2).

For both the metallicity and C/O, really, it is the water and methane that dominate. We point out, as in Parts I and II, that this is a measure of the *atmospheric* elemental abundance inventory. The bulk abundances can only be determined via chemical assumptions. Specifically, it is predicted that condensate rain out by silicates (enstatite, forsterite) can sequester oxygen by effectively locking it into condensates which "rain" out of the atmosphere and no longer react with the surrounding gas (e.g. Fegley and Lodders, 1994). As in Part I we apply a correction factor to the C/O and metallicity by weighting the water abundance by a factor of 1.3 to accommodate for the lost O.

Figure 2.4 shows our results of our retrieved metallicity and C/O constraints (circles) compared to the results for late-T dwarfs in Part II (squares), as well as a representative sample of these parameters from near-by FGK stars (grey circles) (Hinkel *et al.*, 2014). Overplotted (triangles) are the results for W2212, W1639, W1405, and W1541 for which the retrieved abundances, and thus C/O and metallicities, are dependent upon the choice of priors for evolutionary parameters and should be interpreted with caution (Section 2.5.2). Plotted here are the results under the "free" retrieval assumption to be consistent with the objects in Part II.

We find that our metallicities are slightly enhanced, but overall broadly consistent

with the local FGK stellar population and our C/O values are consistent with the results of Part II and the stellar population. We note that there appears to be no correlation between the effective temperature and metallicity or C/O for our sample. In Part II it was discussed that the apparent trend of increasing C/O with increasing metallicity for the late-T's could potentially be explained with super-solar [Si/O] ratios affecting the efficiency of oxygen rainout into silicates. By including our new late-T and early-Y sample, we find no such trend even if one were to discount the objects with questionable constraints.

Chemical Trends

One of the defining features of a classic retrieval is in its ability to directly constrain atmospheric *molecular* abundances from the spectra, free from the a priori assumptions commonly made in self-consistent models. Molecular abundance trends with other properties provide insight into the chemical and physical processes operating in the atmospheres. The retrieved molecular abundances for the ensemble of HST WFC3 late-T and early-Y dwarf are given in Table 2.4. Here, we focus on how these abundances vary with effective temperature as this is predicted to be the dominant abundance controlling factor through equilibrium chemistry (Burrows and Sharp, 1999; Lodders and Fegley, 2002; Sharp and Burrows, 2007).

Figure 2.5 summarizes these trends (red, yellow points) in comparison to predictions from a self-consistent grid model (black curves) and to those derived for the warmer T-dwarfs from Part II (blue points). Our chosen grid model was introduced and validated in Piskorz *et al.* (2018) and Bonnefoy *et al.* (2018). We produce a grid of models given $T_{\rm eff}$, log(g), metallicity, and assume radiative-convective thermochemical equilibrium. The molecular abundance curves here are column weighted mixing ratio over the photosphere.

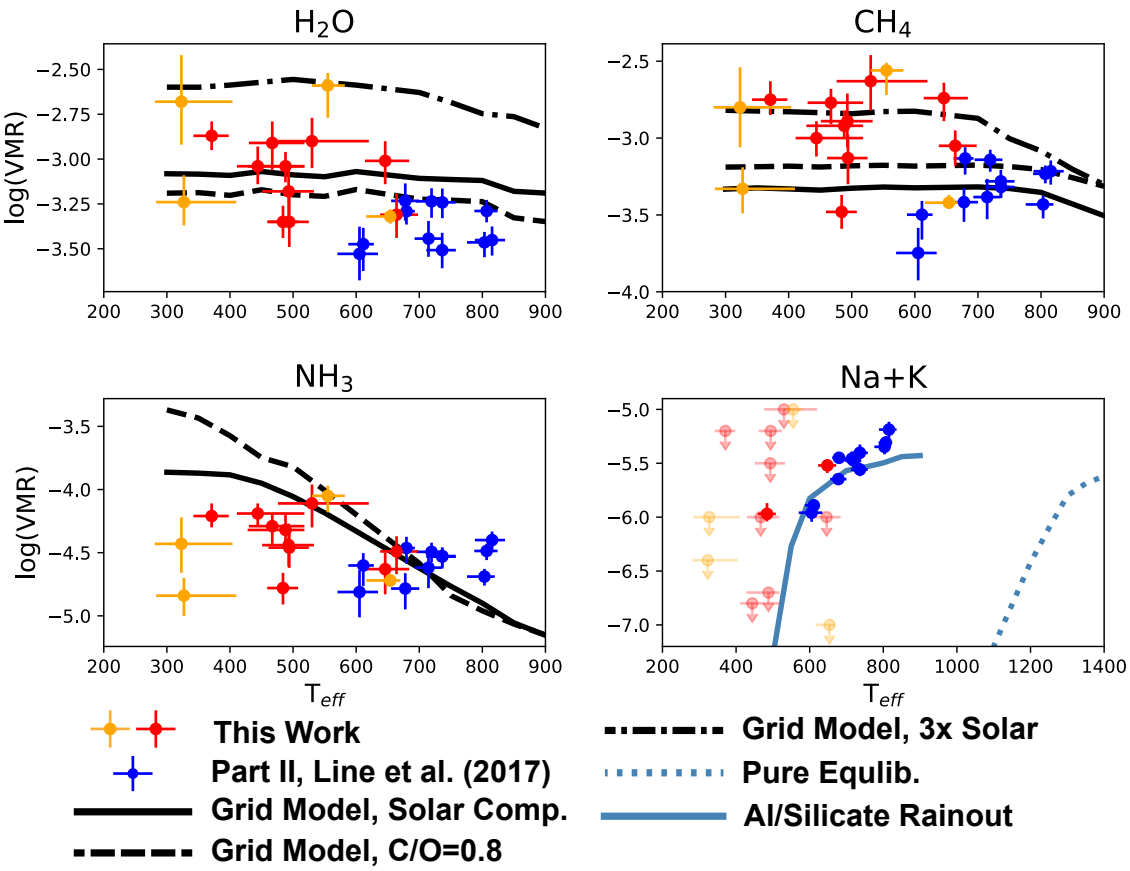

Figure 2.5: Constraints on our retrieved molecular abundances for H_2O (upper left), CH_4 (upper right), NH_3 (lower left) and Na+K (lower right) in units of Volume Mixing Ratio (VMR). Blue points are results from the hotter late-T sample in Part II. Red points are objects of this study whose abundances do not strongly depend on our assumptions of evolutionary priors (log(g), radius, mass) while yellow points are objects whose abundances are sensitive to these assumptions and should be interpreted with caution (see Section 2.5.2). Overlaid are grid model profiles for various metallicites, C/O ratios, and rainout assumptions. Unless stated otherwise, curves are 1x solar composition with assumed thermochemical equilibrium. Pure equilibrium trend from Burrows *et al.* (2001).

We find that the H_2O and CH_4 abundances show a systematic offset between the late-T and early-Y sample. For context we've also plotted column-integrated abundance trends from our grid model, showing that the variation we see between the two samples is largely reproducible by variations in both the C/O ratio and in the metallicity of the system. This falls in line with predictions from equilibrium chemistry where H_2O and CH_4 remain relatively constant for a given set of elemental abundance assumptions, and that neither molecule should be sensitive to other chemical processes such as vertical disequilibrium mixing (Burrows and Sharp, 1999; Sharp and Burrows, 2007).

Part II found no systematic trend in the ammonia abundance with effective temperature, despite thermochemical equilibrium predicting a $\sim$0.5 dex increase over the 800-600K temperature range for a given metallicity. Ammonia is well known to be influenced by vertical mixing at these cool temperatures. Vertical mixing is expected to quench the ammonia abundance to one order of magnitude *lower* than the equilibrium abundance over the photospheric layers (Saumon *et al.*, 2006; Marley and Robinson, 2015).

However, we note that with the addition of our sample, we see a slight trend of increasing ammonia that is largely consistent with thermochemical equilibrium assumptions at a range of metallicities and gravities. Note that we have not included the yellow points in this analysis given the complications with these objects, highlighted in Section 2.5.2. Though it is possible that the ammonia in the atmospheres of these objects is being affected by disequilibrium mixing at varying strengths, the ability to test such ideas quickly becomes limited by both the sparse number of retrieved NH_3 abundances, and the precision of our retrieval constraints.

A more striking compositional trend, extending far beyond the results in Part II, is that of the alkali metals with temperature. The retrieved Y-dwarf alkali abundances

fall off substantially with temperature relative to the warmer T-dwarfs. In all but two cases (W0325,W0335), we only obtain upper limits on the alkali abundances due to the lack of detectability. These results are consistent with predictions from equilibrium rainout chemistry (blue, solid) and strongly disfavor pure equilibrium (blue-dashed, from Burrows *et al.* (2001)). Pure equilibrium permits the existence of aluminum and silicates in the middle atmosphere which achieve equilibrium with the Na and K to form sanidine ($KAlSi_3O_8$) and albite ($NaAlSi_3O_8$) (Burrows *et al.*, 2001), resulting in a rapid depletion of gaseous Na and K at $\sim$1300K. In contrast, rainout rapidly removes aluminum/silicates leaving behind the gas phase alkalies until $\sim$700K where they begin to condense into KCl and Na_2S (e.g. Burrows *et al.*, 2001). These results are the first to show that a number of indirect lines of evidence for rainout from both pre-computed grid models (e.g Marley *et al.*, 2002; Morley *et al.*, 2012, 2014), and observations of reddening Y-J colors (e.g. Liu *et al.*, 2012; Schneider *et al.*, 2015) are directly owed to the depletion of Na and K.

We obtain two bound constraints for W0325 and W0335, and only lower limits for cooler targets as the alkalies deplete below retrievable abundances. We note that the one anomalous lower limit at roughly 650K is W1639 whose temperature structure strongly deviates from the typical radiative-convective equilibrium. As a result it is not surprising to find the upper limit for the abundance of this target is systematically shifted from the remainder of our curve. Additionally the results for our three other objects with questionable abundance constraints (W2212, W1405, W1541) still show good agreement with the solar metallicity trend, though this may be a result of only obtaining upper limits for these targets.

Improved SNR and spectral resolution with JWST, particularly at the blue end of the Y band, and near roughly $1.2\mu m$ where the resonance features for Na and K peak, should allow us to probe cooler objects with far more depleted alkali abundances or

Table 2.5: ScCHIMERA Grid Model Ranges and Step Sizes

Parameter	Range	Step Size
T_{eff} [K]	300−950	50
log(g) [cgs]	3.0−5.5	0.5
[M/H]	-1−1	0.5
C/O	0.1−0.7	0.2
	0.7−0.9	0.05
$\log(K_{zz})$	2−8	2

uniquely constrain both Na and K independent of each other. In addition, improved NH_3 constraints on a larger number of Y-dwarfs may also allow us to directly confirm the presence of vertical disequilibrium mixing in the future.

2.5.4 Grid Model Fitting

While the retrieval-based approach is useful in its ability to place as little a priori information as possible into the atmospheric model, it is still useful to compare such results against a grid-based model. Grid models incorporate more assumptions and are presumably more self-consistent in that they often treat the atmosphere under radiative-convective-thermochemical equilibrium whereas our retrieval method makes no such assumptions. This is useful in the investigation of both missing model physics within the established grid models, and any possible nonphysical results from the retrieval method as we have seen with our evolutionary parameters.

We use a newly developed grid of self-consistent, cloud-free atmospheric models (Self-consistent CHIMERA, ScCHIMERA) (Piskorz *et al.*, 2018; Bonnefoy *et al.*, 2018), which utilizes the same underlying radiative transfer and opacity sources as the retrieval forward model. Briefly, the self-consistent model solves for layer mid-

point fluxes using the Toon *et al.* (1989) two stream source function approach. The model is iterated to radiative equilibrium using the Newton-Raphson method until there is zero net flux divergence throughout the column. Convection is implemented through a mixing length flux (e.g. Marley and Robinson, 2015). Line-by-line cross-sections are converted to R=100 correlated-K coefficients between 0.3 and 100μm (using 20 Gauss quadrature points per wavenumber-bin) utilizing the "resort-rebin" (Amundsen *et al.*, 2017) optical depth approach to speed up efficiency but to maintain accurate flux computations. The converged models are "post-processed" to an R=1000 (again with correlated-K). These moderate-resolution spectra are then convolved and binned to the data wavelength grid when undergoing fitting. The grid is generated as a function of T_{eff}, log(g), [M/H], the C/O ratio, and the vertical eddy diffusion K_{zz} (through the Zahnle and Marley (2014) quench-time scale framework). The grid model parameter ranges and step sizes are given in Table 2.5. Using `emcee` and an interpolating function (a variant of Python's `griddata` routine) we fit each object with this 5-dimensional grid, but have also experimented with different subsets of parameters (e.g., fitting for only log(g) and T_{eff} while fixing composition to solar).

Figure 2.6 shows an example comparison (for W0404) between the grid model solutions and the retrieval solutions. In this specific instance, T_{eff}, log(g), [M/H] and the radius-to-distance scaling are the free parameters of the grid with no quenching. From a visual standpoint, there are noticeable differences between the grid model fit and the retrieval fit. The best fitting grid model under fits the Y-band peak and overestimates the J-band peak by $\sim$10-20%, as well as the entire blue edge of the H-band. This issue of either overestimating the J-band, underestimating the Y and H bands, or both, is consistent across all of our objects. This result is not unique to our grid model, as previous work using other cloud-free grid models have had similar issues (Schneider *et al.*, 2015; Leggett *et al.*, 2017).

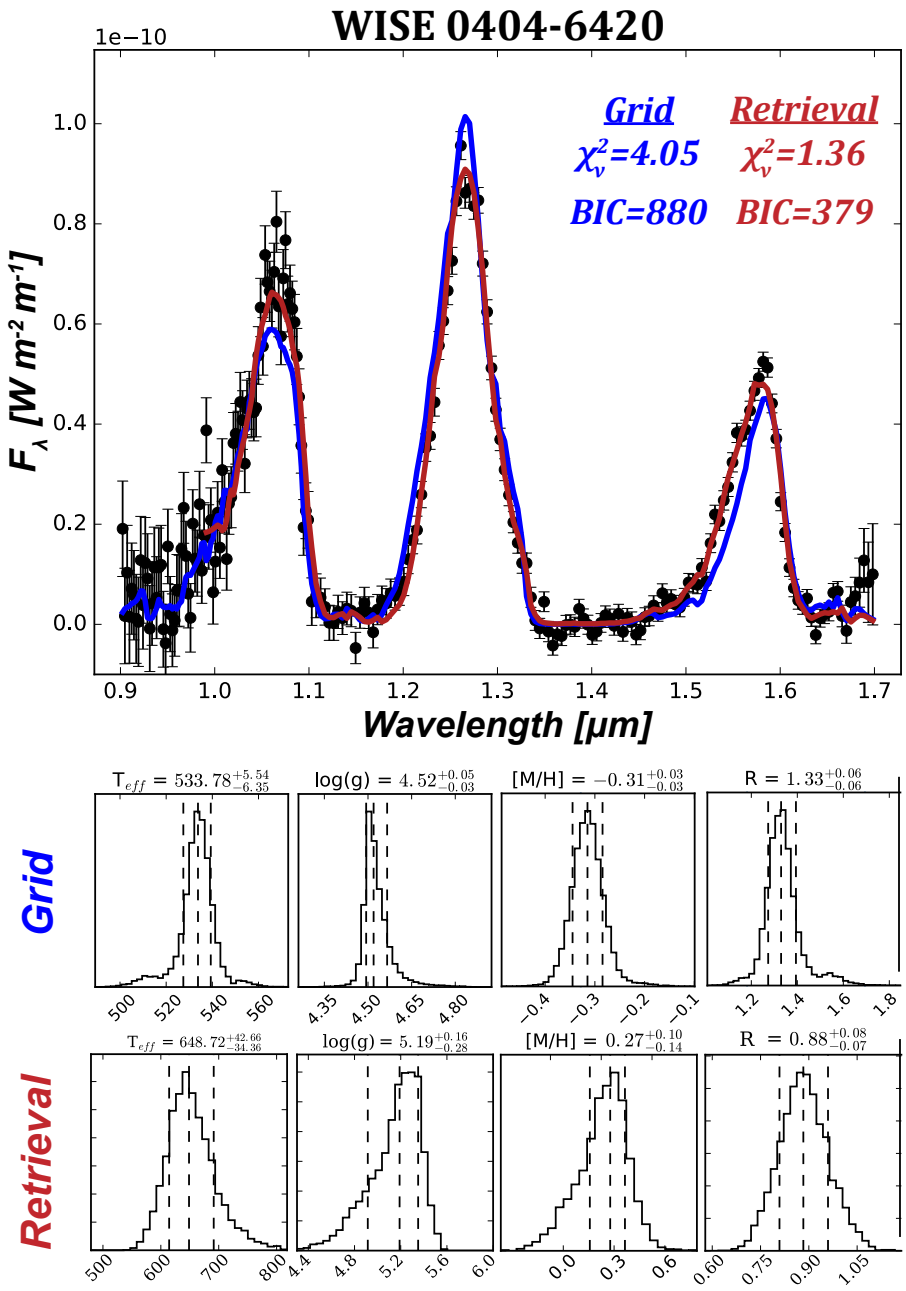

Figure 2.6: (Top) Best-fit grid-model (blue) and retrieval (red) results for W0404. With only 4 free parameters ($T_{\rm eff}$, log(g), [M/H] and R) the grid model struggles to well-fit the entire YJK-band spectra with systematic offsets in each band. Comparing the Bayesian Information Criterion (BIC) between both models suggests the retrieval method is highly preferred. (Bottom) Marginalized posteriors for the relevant free parameters in each model. The poor fit of the grid model often disagrees with the retrieval model and obtains nonphysical constraints.

The grid model best fit produces a $\chi^2/N = 4.05$ compared to the retrievals $\chi^2/N = 1.36$. We utilize the Bayesian information criterion (BIC) to determine the balance between improved fit and increased parameters and whether the retrieval parameters are indeed justified. The retrieval forward model includes 31 free parameters and 175 data points (we stop at 1μm due to constraints on the molecular cross-sections) giving a $BIC = 379$. The self-consistent grid fit has only 4 free parameters (in this example) and 212 data points (the grid model goes down to 0.9 μm) resulting in a $BIC = 880$. The $\Delta BIC = 501$ overwhelmingly favors the retrieval fit according the Jeffery's Scale (Kass and Raftery, 1995). Regardless of the number of free parameters we include in our grid model (including the vertical mixing and carbon-to-oxygen ratio dimensions), we often find similar misfits.

Figure 2.6 also compares the retrieval and grid-model constraints on effective temperature, gravity, metallicity, and radius. We find (consistent amongst our other objects) that the retrieval and grid models often disagree by at least several sigma in almost all model parameters. In the specific example of W0404, the grid model derived effective temperature disagrees with our retrieval result by over 100K, the gravity estimate is inconsistent to almost a full order of magnitude, the metallicity is sub-solar for the grid model yet super-solar for our retrieval, and the radius is inflated in the grid model fit.

For our other targets, the grid model often requires either unphysically high or low: radii, masses, and gravities for typical field brown dwarfs, as well as effective temperatures inconsistent with previously measured spectral types. A full database of all fits, and resulting model parameters, is available at our previously linked Zenodo site. This highlights the need for a retrieval methodology to fully utilize the information content contained in substellar atmospheric spectra in order to accurately characterize both current and future datasets.

2.6 JWST Simulations

JWST promises to revolutionize our knowledge of brown dwarf atmospheres due to: a vastly improved wavelength coverage across the near and mid infrared, combined with improved SNR and spectral resolution (Marley and Leggett, 2009). Here we take a preliminary look at the potential improvement in our retrieval parameters with JWST for a representative T9 object (W0404).

We take the best fitting model to the HST data for W0404 (that is our best-fit model with the parameters specified in Tables 3, 4, and associated figures) and simulate both Near InfraRed Spectrometer (NIRSpec) PRISM and Mid-InfraRed Instrument, Low-Resolution Spectroscopy (MIRI,LRS) observations using the JWST Exposure Time Calculator (ETC) v1.3. The largest 1.6" slit was chosen for the PRISM/CLEAR configuration and a slitless spectroscopy mode for MIRI LRS were chosen to minimize potential systematic slit-losses from the instrument. We set the integration time to obtain, somewhat arbitrarily, SNR$\approx$200 at the J-band peak within the PRISM mode and SNR's$\approx$10 over MIRI LRS. We found this was achievable with 15 minutes and 1 hour of exposure time on NIRSpec and MIRI respectively.

We then applied the same retrieval tools to this simulated data set, under the same exact model assumptions, comparing three cases: WFC3 only (this work), WFC3+MIRI LRS, and NIRSpec PRISM only (Figure 2.7). Figure 2.8 summarizes the constraints (red=WFC3 only, blue=WFC3+MIRI, green=NIRSpec only). It is clear that JWST will provide astounding improvements on the molecular abundances, gravity, and temperature profile. For example, we find that the H_2O abundance constraint improves from $\pm$0.1dex with WFC3 to roughly $\pm$0.06dex with WFC3 combined with an hour of MIRI LRS integration time, and better than $\pm$10% for only 15 minutes of NIRSpec integration time. These extremely tight constraints approach

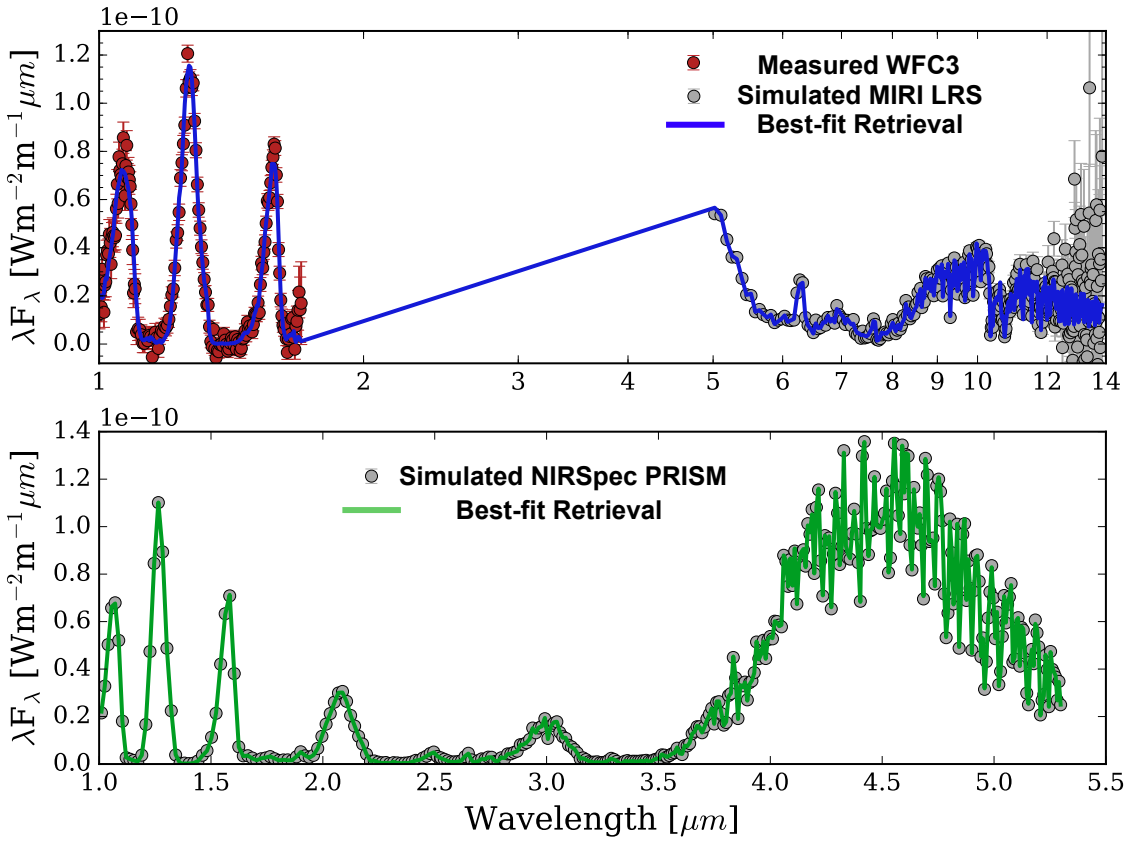

Figure 2.7: JWST Spectral Fits

Top: Best fit spectrum (blue) to a combined WFC3 observation (1-1.7μm, red) and JWST MIRI LRS simulation (5-14μm, grey). *Bottom:* best-fit spectrum (green) to a simulated JWST NIRSpec PRISM spectrum (grey). NIRSpec provides vastly improved SNR (200 vs. 10) for a much shorter exposure time (15mins vs 1hr) when compared to MIRI LRS.

the precision of remote solar-system quality science on brown dwarfs, and speak to the utility of JWST to well-characterize nearby substellar atmospheres in the future.

One caveat here is that this analysis makes the assumption that our model that best-fits the YJH bands of WFC3 is an accurate representation of the object's spectra at both longer wavelengths and higher spectral resolutions. Additionally, such an analysis does not account for any potential systematics, currently known or unknown,

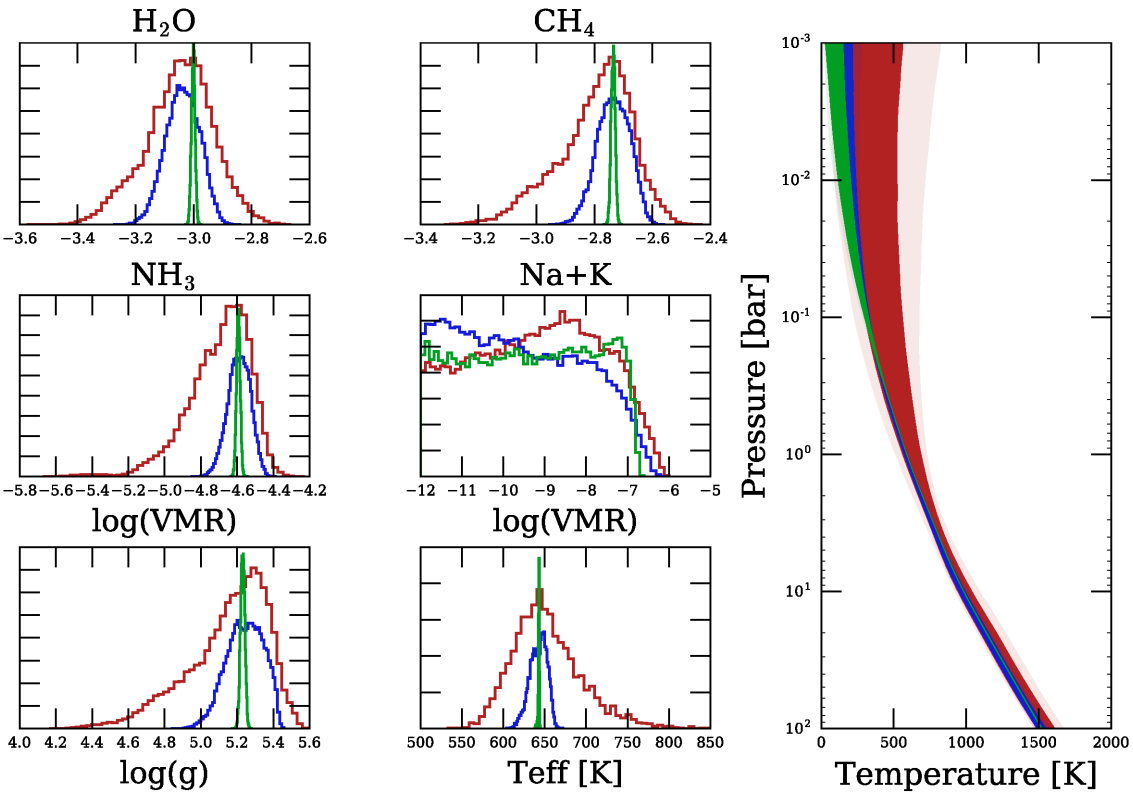

Figure 2.8: Best-fitting model parameters from our analysis of WFC3 spectra (red). Overlaid are the resulting JWST NIRCam PRISM datapoints and error estimates from the ETC (green). An additional retrieval using a combined WFC3 and MIRI LRS spectrum is also shown for comparison (blue). A NIRCam PRISM observation provides substantially higher precision on molecular abundances and atmospheric structure than a combined WFC3 and MIRI LSR spectrum for about a quarter of JWST exposure time.

that will impact the future performance of JWST that are not properly accounted for in the JWST ETC. These systematic biases between instruments, or within JWST itself, will lower the precision of constraints shown here. Despite these limitations, such an analysis provides an initial first step in understanding how well JWST will be able to constrain atmospheric properties on cool brown dwarfs.

2.7 Conclusions

We have extended the work of previous investigations using a well-vetted atmospheric retrieval approach into the cooler Y dwarf spectral class. This is done by comparing our model to a set of uniformly reduced, low-resolution WFC3 measurements for an ensemble of late-T and early-Y dwarfs. Such a methodology has provided the first direct constraints on the chemical composition of cool Y dwarfs and provides a foundational dataset that can be compared to future low-mass characterization work. Our main scientific results are as follows:

1. We are able to well-fit our ensemble of late-T and early-Y dwarfs with our retrieval model across the YJH bands as shown in Figure 2.1, Section 2.5. We find no systematic deviations from the data in our residuals. This is in contrast to typical grid modeling efforts which often miss key spectral features of these cooler objects.

2. Overall the retrieved temperature structures are consistent with radiative - convective equilibrium except in the marked case of W1639 whose peculiar Y band structure may be indicative of a non-radiative-convective equilibrium structure in Figure 2.1, Section 2.5.1. However, inconsistencies in derived evolutionary parameters may also indicate our model is not well adapted to explain the odd Y band structure.

3. For most of our objects, we obtain mass estimates that are consistent with field-age brown dwarfs but systematically smaller radii, and higher gravities than allowable with evolutionary models (see Figure 2.3, Section 2.5.2). We attempted a myriad of tests on both the observational data and our retrieval model to discover the cause of this deviation. Using a distance estimate from

another parallax program, we found that W2056's anomalously high gravity could be explained by a systematic bias in the distance estimate. If the distances are all systematically underestimated, this would explain both our high gravities and lower radii for the majority of our objects. More importantly this indicates how sensitive our retrieved results can be to small changes in distance estimates. The coldest Y dwarfs, W1405 and W1541's results are speculative at best given the retrieved masses and radii are inconsistent with known limits for field-age brown dwarfs.

4. We obtain for the first time, direct, bound constraints or upper limits on H_2O, CH_4, CO, CO_2, H_2S, NH_3, and Na+K for an ensemble of cool Y dwarfs (see Section 2.5.3). From these measurements we drive preliminary C/O and metallicity estimates that, when oxygen sequestering via chemical rainout of silicates is taken into account, are broadly consistent with the local FGK stellar population, albeit at slightly enhanced metallicity.

5. From these measurements we investigate chemical trends with T_{eff} which are diagnostic of the chemical mechanisms at work in the atmospheres of brown dwarfs. We find that H_2O and CH_4 are consistent with expected chemical equilibrium predictions and are not subject to either chemical rainout or vertical disequilibrium mixing. NH_3 may show a tentative trend with either pure chemical equilibrium or disequilibrium vertical mixing. Improved constraints from JWST would be more diagnostic of this trend and may be able to constrain the strength of mixing. Finally, Na+K shows a trend consistent with both chemical rainout and the results in Part II, as opposed to pure chemical equilibrium. This result confirms that the blue shift in the Y-J color photometry across the T/Y boundary is owed to the depletion of alkali metals.

6. We make predictions for future JWST observations for cool late-T and early-Y dwarf targets. We find that NIRSpec offers the best observing mode in order to do high-precision abundance measurements on near-by brown dwarfs, approaching that of current bulk solar-system quality measurements. Such high precision abundance measurements provide useful diagnostic for future modeling efforts to understand cool, substellar atmospheres.

2.8 Acknowledgements

We thank Roxana Lupu and Richard Freedman for continued development and support of their extensive opacity database which makes much of this work possible. We also thank Dan Foreman-Mackey for his publicly available EMCEE code and the useful plotting routine `corner.py`. We thank Adam Schneider, Mark Marley, Jennifer Patience, Laura Kreidberg, Michael Cushing, Jackey Faherty, Trent Dupuy, and Wanda Feng for the many comments, discussions, and tools which have improved this work. This research has benefited from the Y Dwarf Compendium maintained by Michael Cushing at https://sites.google.com/view/ydwarfcompendium/. This material is based upon work supported by the National Science Foundation under Grant No. AST-1615220.

Chapter 3

ACCELERATING ATMOSPHERIC RETRIEVAL WITH GRAPHICAL PROCESSING UNITS

3.1 Introduction

Over the past two decades, Graphical Processing Units (GPUs) have become an essential tool to solve increasingly complex, and computationally expensive, numerical problems. GPUs began to outpace development of Central Processing Units (CPUs) in terms of raw performance in the early 2000s. However, GPUs were initially designed as highly specialized pieces of hardware, and required a deep knowledge of either assembly languages, or later, translating one's problem into shader languages derived from C, such as OpenGL's Core Language (GLSL). Several scientific and mathematical fields took advantage of this new hardware to construct suites of algorithms for General-Purpose computing on GPUs (GPGPU), including: early work on ray tracing of light, photon mapping, data mining, and computer vision. Despite these breakthroughs, the technical expertise to program on these units remained a barrier-to-entry for those outside of the GPGPU working groups (for a review, Owens *et al.*, 2007).

Seeking to capitalize the market share for scientific GPGPU development, GPU manufacturers such as NVIDIA, and to a lesser extent AMD, have placed a large amount of research & development into making GPGPU programming more end-user friendly. One of the dominant software suites in this space has been NVIDIA's Compute Unified Device Architecture (CUDA), which was initially developed to support programming in the C language on GPUs (Buck, 2007). CUDA has since developed

into one of NVIDIA's flagship software products across multiple languages, and is used in a wide array of fields including: medical imaging, defense, computational finance, and, of course, astronomy (NVIDIA *et al.*, 2020).

The field of astronomy was one of the first to adopt GPGPU methods, with papers citing the pre-1.0 CUDA release notes in eager anticipation of new features such as improved floating point precision (Belleman *et al.*, 2008). As of this writing, over one thousand papers can be found on NASA's Astrophysical Data System that incorporate GPGPU methods into: magnetohydrodynamic models (Liska *et al.*, 2018), globular cluster evolution (Wang *et al.*, 2016), N-Body simulations (Nitadori and Aarseth, 2012; Wang *et al.*, 2015), galactic abundance measurements (Leung and Bovy, 2019), and MCMC sampling of high-dimensional parameter space for exoplanet lightcurve modeling (Parviainen, 2015).

One area of astronomy which can substantially benefit from GPGPU methods, but has yet to take full advantage of this hardware, is atmospheric retrieval of brown dwarfs and exoplanets. Retrievals are extremely computationally expensive to perform, even on some of the best CPUs available on the market. Though there are some notable exceptions in the literature (e.g. Malik *et al.*, 2017), this computational limitation of CPUs has restricted the scientific progress of understanding substellar atmospheres by preventing population-level atmospheric retrieval studies. By transferring part of the atmospheric retrieval calculations onto GPUs, not only can retrievals of individual objects be done more quickly, but more diagnostic tests can be performed over representative samples of the entire brown dwarf population. This improvement in computational speed then can directly translate into a better understanding of the entire population of substellar atmospheres.

In this chapter, I discuss my work on understanding the computational limitations of the CHIMERA retrieval model, implementing NVIDIA's CUDA software into the

python-based CHIMERA code, and diagnosing the improvement in runtime this provides. Section 3.2 provides a more detailed discussion of the step-by-step operations performed within CHIMERA in order to explain the true computational bottleneck. Discussion for how this bottleneck is addressed is then discussed in Section 3.3. Finally, I summarize this chapter's main findings in Section 3.4.

3.2 Radiative Transfer

Figure 3.1 provides a schematic representation of the CHIMERA retrieval model. Beginning from the left, an initial guess for the input parameters (gas VMR, temperature profiles, cloud model, gravity, etc.) are used to calculate the physical state of the atmosphere. This includes the gas VMR at each level (taken to be constant throughout this work), and the shape of the TP, and cloud profile. These inputs are then used, with an estimation for the interior heat below the atmosphere, to calculate the emergent, disk-integrated, 1D spectrum at high spectral resolution (R=10^5). This calculation is done as described in Appendix A of Lacis and Oinas (1991), where the radiative transfer is solved assuming the intralayer temperature gradient to be linear in Planck radiation, combined with a Gauss-Legendre standard quadrature solution.

To be explicit, the differential emission of a slab at some optical depth τ' is given by Equation A1 in Lacis and Oinas (1991) as,

$$dE(\mu) = B_\nu(\tau')e^{\tau/\mu}d\tau'/\mu \tag{3.1}$$

where μ=cos(θ) with θ the angle with respect to the vertical, and $B_\nu(\tau')$ is the Planck radiation. The linear dependence on the Planck radiation is explicitly,

$$B_\nu(\tau') = B_\nu(T_t) + \tau'/\tau \left(B_\nu(T_b) - B_\nu(T_t)\right). \tag{3.2}$$

with T_t and T_b being the temperature at the top and bottom layers respectively.

Making this assumption allows for the calculation of the upward intensity in closed form,

$$\begin{aligned} E(\mu) =& B_\nu(T_t) - B_\nu(T_b) + \\ & \left(B_\nu(T_b) - \mu/\tau \left[B_\nu(T_b) - B_\nu(T_t)\right]\right) \left(1 - e^{-\tau/\mu}\right). \end{aligned} \tag{3.3}$$

This provides the intensity with respect to emission angle μ, and is the equation used within the CHIMERA radiative transfer code. To integrate over these emission angles, the otherwise exponential integral is solved numerically using Gaussian quadrature via Equation A8 in Lacis and Oinas (1991),

$$E = \sum_{i=1}^{N} E(\mu_i)\mu_i w_i, \tag{3.4}$$

using N=4 different emission angles μ_i and their appropriate weights w_i. This is calculated for each wavelength ν and output as a high resolution model spectrum.

This spectrum is then used, with the observational spectrum, and the `emcee` package (Foreman-Mackey *et al.*, 2013), to solve for the posterior distribution on the input model parameters. This entire process is repeated anywhere from 20,000 to 100,000 times depending upon how long it takes for the walkers within the MCMC to converge upon the posterior.

To improve the runtime of this process, the most computationally expensive steps must be identified. Each step described above was timed for a full retrieval of Gliese 570D out to 20,000 iterations over the WFC3 0.9-1.7μm bandpass. The average time (to within an order of magnitude) that each step took running on ASU's Agave Cluster with 12 cores of Intel Xeon E5-2680 v4s with 2.4GHz base clock-speed is shown in Table 3.1. Processes that are only done once per retrieval, such as loading in each table of molecular cross sections, are omitted.

As shown, most steps outside the radiative transfer take a fraction of a second,

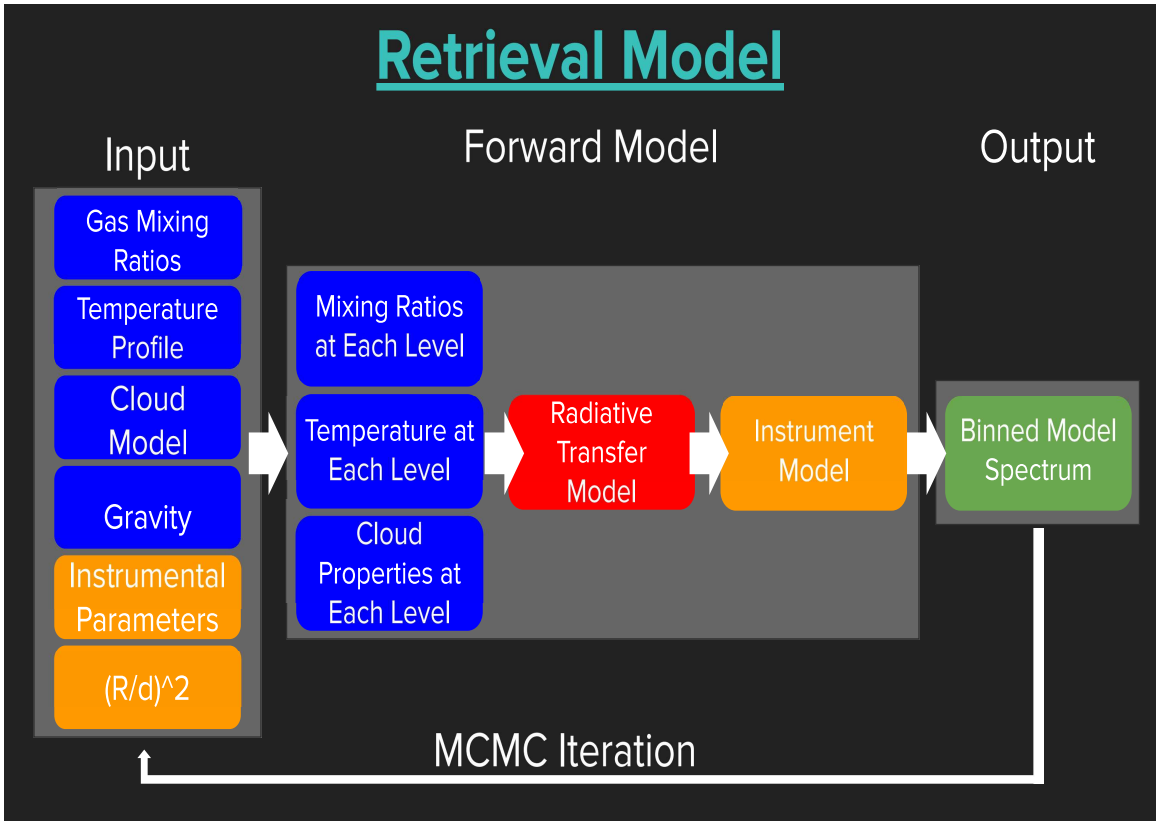

Figure 3.1: Flowchart of the CHIMERA Retrieval Model.

Table 3.1: Average Runtime for Each Step in a CHIMERA Retrieval

Step	Avg. Time [s]
MCMC Initialization	0.01
Array & Parameter Declaration	0.001
Radiative Transfer	1.5
Binning Spectrum	0.001-0.01
MCMC Step	0.01

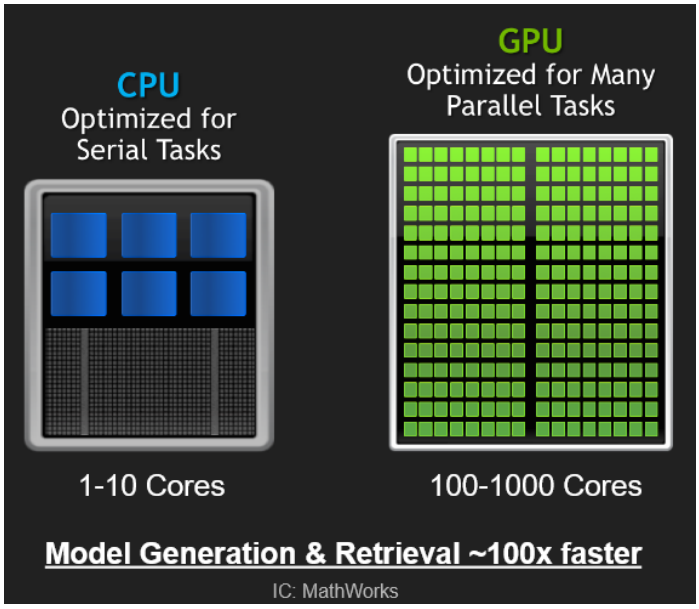

Figure 3.2: Schematic differences between a CPU and GPU. IC: https://www.mathworks.com/company/newsletters/articles/gpu-programming-in-matlab.html

with the radiative transfer dominating by two orders of magnitude. At these speeds, a single retrieval with a single set of priors takes just over 20 hours. While multiple retrievals can be run upon the cluster at once, this 20 hour runtime places strong logistical constraints on how many prior assumptions can be tested and/or how many targets can be analyzed. For this reason, the radiative transfer was targeted as the main portion of the retrieval model to take advantage of GPGPUs.

While not a surprise, confirmation that the radiative transfer is the bottleneck was important as not all runtime efficiency problems can be solved with a GPU. Figure 3.2 highlights an important fundamental difference in hardware between a standard CPU and GPU. In a single or multicore system, each individual CPU core is highly optimized for runtime of serial tasks with high clock speeds. GPUs, by comparison, require the ability to break any given problem into many smaller computations that can be worked on in parallel. Thus, even with lower core clock speeds compared to CPUs, GPUs can solve problems more quickly if given the right type of problem.

The main computational bottleneck of solving the radiative transfer in a spectroscopic retrieval is calculating the emergent flux for each independent wavelength sample individually. In the test carried out in Table 3.1, there were only 12 logical cores to compute the thousands of individual wavelength points for the R=10^5 model over the WFC3 bandpass. Since each wavelength is completely independent, that it it does not require any information from nearby wavelengths to compute the radiative transfer, the problem of multiwavelength radiative transfer is a highly parallelizable problem, and thus a natural fit to be placed upon a GPU.

An oversimplified attempt to quantify how much runtime could be saved is also shown in Figure 3.2. Since a typical GPU has ∼10-100 more cores than a CPU, an upper limit to the time saved would be anywhere between a factor of 1-2 orders of magnitude. The real runtime difference of course depends on the individual clock speeds, core speeds, and memory speeds of both the CPU and GPU being compared, and additional overheads of how memory is stored and processed. However, improving the runtime by even less than 1 order of magnitude would significantly help in better understanding substellar atmospheres. With this in mind, Section 3.3 details the specific implementation of this idea onto a private GPU cluster at ASU.

3.3 Numba

To support this work, 4 NVIDIA V100 GPUs with 32GB of memory each were ordered, installed, and are currently maintained by ASU's Residental Computing Facility. The specific incentives for choosing these cards were the high number of cores (5120), high amount of GPU memory to support the large molecular cross sections needed for atmospheric retrieval (32GB), and their out-of-the-box compatibility with various CUDA APIs.

There were several options to allow CHIMERA's radiative transfer to interface

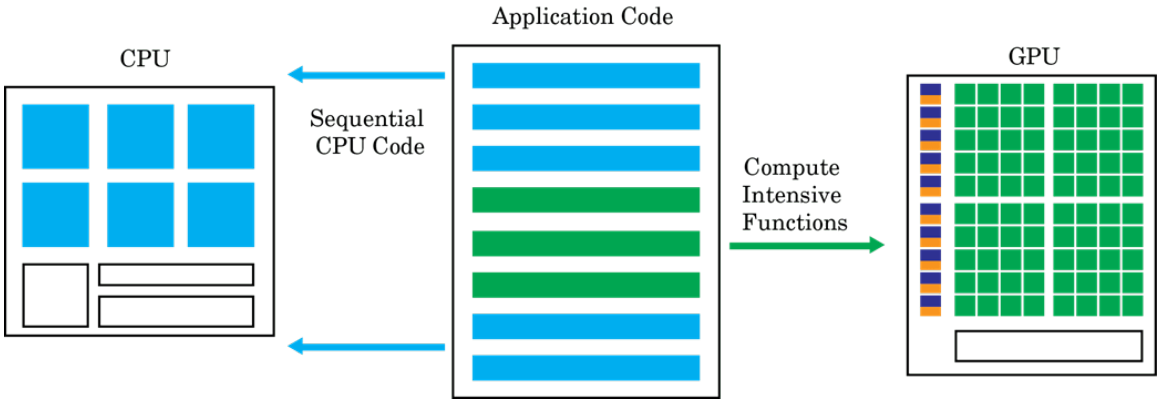

Figure 3.3: Schematic of the application of `Numba` into CHIMERA's radiative transfer. IC: https://www.mathworks.com/help/gpucoder/gs/gpu-prog-paradigm.html

with the CUDA API, each of which required differing approaches towards rewriting the radiative transfer. Though others were explored, such as rewriting most of the code to interface with Cython or other brdiges to C, the most straight-forward way was to utilize the Anaconda `Numba` package within Python itself. `Numba` is a general just-in-time (jit) compiler that allows almost arbitrary Python functions to be passed into assembly code and compiled just in time for execution (Lam *et al.*, 2015). The main benefit of this package is we are able to simply declare a `Numba` decorator over two important Python functions within the radiative transfer core, and the rest of the computational work is handled by both `Numba` and later processed on the GPU via the inbuilt CUDA API.

An illustration of how this was executed is shown in Figure 3.3. In this graphic, a majority of the code including the specific MCMC implementation, variable and array declaration, and visualization, were all carried out through the blue application code on CPUs. The compute intensive functions in our implementation were two specific functions. The first function is given the model input parameters shown in Figure 3.1. It then calculates the total optical depth due to the presence of the specified gasses

```
#****************************************************************
# FUNCTION: rad_2.py
#
# DESCRIPTION:
# Goes through each atmospheric level, interpolates cross sections
# and computes the total optical depth for the given VMR, TP profile,
# and gravity. Helper for rad_2. Uses Numba GPU package for speed.
# NOTE: Original 'rad_2.pro' IDL code is present here in the
# comments that lead into particular blocks of code.
#
#****************************************************************
#args: VMR,mmw,g0,kappa,fcloud,np.log10(Pgrid), np.log10(Tgrid), P, T, xsecarr[loc,:,:,:]


@guvectorize([(float64[:],float64,float64, float64, float64[:],float64[:],float64[:],
             float64[:],float64[:],float64[:,:,:],float64[:])],
             '(q),(),(),(),(p),(m),(n),(o),(o),(n,m,q)->(o)',
             target='cuda',nopython=True)
def xsec_interp_tau_gpu(VMR,mmw,g0,kappa, fCloud, logPgrid, logTgrid, Patm, Tatm,
                        xsec, dtau_tot):




@guvectorize([(float64, float64[:], float64[:],float64[:],float64[:], float64[:])],
             '(),(n),(n),(m),(m)->()',target='cuda',nopython=True)
def intensity_gpu(wno,T,ttau, ugauss, wts, F):  #note, it's returning "F" as a 1 element array
```

Figure 3.4: Code snippet of two radiative transfer core functions. The top, `xsec_interp_tau_gpu`, interpolates molecular cross sections and calculates the optical depth τ given the TP profile, gas abundances, and cloud model. The bottom, `intensity_gpu`, uses this optical depth to calculate the emergent, disk-integrated flux using our radiative transfer prescription in 3.2. The `@guvectorize` decorator over each function allows `Numba` to pass the computations to the GPU, given the function's input data types and array dimensions.

at each wavelength. The second function calculates the emergent, disk integrated flux using this optical depth for every wavelength as detailed in Section 3.2. Both functions use `Numba`'s `@guvectorize` decorator to pass the input `NumPy` arrays of varying dimensions into CUDA. A screenshot each of these functions as they appear in CHIMERA, including the `@guvectorize` decorator are shown in Figure 3.4.

With this implemented into CHIMERA, the same test of running a Gliese 570D model over the WFC3 bandpass of 0.9-1.7μm at R=10^5 as discussed in Section 3.2 was recomputed on a single NVIDIA V100 GPU. The average time for model generation

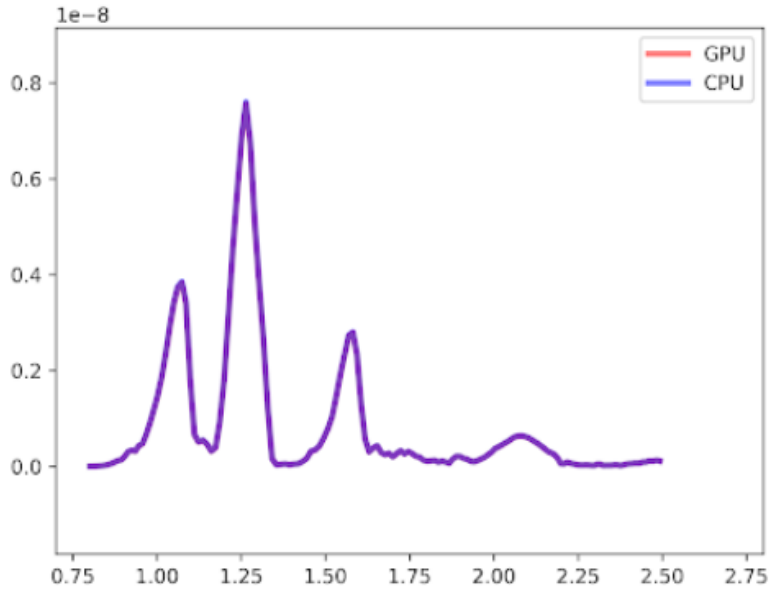

Figure 3.5: Spectrum of Gl 570D calculated using both a GPU and CPU. Both spectra are identical with the GPU calculation taking an order of magnitude less in runtime.

was ∼0.05 seconds and a total runtime for full retrieval of 33 minutes. This marks an improvement in the runtime by a factor of 36, directly in-line with simply considering the increase in the number of cores.

Figure 3.5 shows a representative test case of comparing the resultant spectra computed by the CPU and GPU retrieval code over the SpeX bandpass (Burgasser, 2014). Both spectra are identical by-eye and, through testing the various targets discussed in Chapter 4, have been shown to lead to identical science results when performing complete retrievals.

3.4 Summary & Conclusions

GPUs are amazing scientific tools that, when applied to the correct problems, can solve otherwise complex numerical issues with ease. Applying the technique of GPGPUs to future problems not only in the realm of atmospheric retrieval, but

astronomy as a whole, will be necessary to drive innovation as astronomical datasets become larger and more complex. In this thesis chapter I have:

1. Discussed how my own specific sub-field of atmospheric retrieval could strongly benefit from understanding and applying GPGPU techniques to computational challenges in atmospheric modeling.

2. Described a successful implementation of GPGPUs by placing CHIMERA within a NVIDIA CUDA framework through the Anaconda `Numba` package.

3. Have robustly tested this implementation to show that it provides the same scientific output while saving over an order of magnitude in computational runtime.

With this established, I now move on to implementing this approach on a much larger dataset of 50 late-T dwarfs in Chapter 4.

Chapter 4

A STATISTICAL CENSUS FROM 60 LATE-T DWARF RETRIEVALS

4.1 Abstract

The spectra of brown dwarfs are key to exploring the chemistry and physics that take place in their atmospheres. Late-T dwarf spectra are particularly diagnostic due to their relatively cloud-free atmospheres and deep molecular bands. With the use of powerful atmospheric retrieval tools applied to the spectra of these objects, direct constraints on molecular/atomic abundances, gravity, and vertical thermal profiles can be obtained enabling a broad exploration of the chemical/physical mechanisms operating in their atmospheres. We present a uniform retrieval analysis on low-resolution IRTF SpeX near-IR spectra of a sample of 50 T dwarfs, including new observations as part of a recent volume-limited survey. This analysis more than quadruples the sample of T dwarfs with retrieved temperature profiles and abundances (H_2O, CH_4, NH_3, K and subsequent C/O and metallicities). We are generally able to constrain effective temperatures to within 50K, volume mixing ratios for major species to within 0.25dex, atmospheric metallicities [M/H] to within 0.2, and C/O ratios to within 0.2. We compare our retrieved constraints on the thermal structure, chemistry, and gravities of these objects with predictions from self-consistent radiative-convective equilibrium models and find, in general though with substantial scatter, consistency

with solar composition chemistry and thermal profiles of the neighboring stellar FGK population. Objects with notable discrepancies between the two modeling techniques and potential mechanisms for their differences, be they related to modeling approach or physically motivated, are discussed more thoroughly in the text.

4.2 Introduction

Brown dwarfs are substellar objects whose masses are intermediate between the latest M-type stars and the most massive planets (Hayashi and Nakano, 1963; Shu, 1977; Becklin and Zuckerman, 1988; Rebolo *et al.*, 1995; Oppenheimer *et al.*, 1995; Saumon *et al.*, 2006). Similar to stars, brown dwarfs form from interstellar molecular gas cloud core collapse (Uehara and Inutsuka, 2000; Bate *et al.*, 2002; Krumholz *et al.*, 2005; Whitworth and Stamatellos, 2006; Chabrier *et al.*, 2007; Whitworth *et al.*, 2007; Hennebelle, 2012), but do not achieve masses high enough to sustain core H-fusion over their lifetime (Burrows *et al.*, 2001). As the effective temperatures of brown dwarfs are much cooler than those of stars (< 2500K), molecules and condensates form in their photospheres and dominate the spectral energy distribution. It is through analyses of these spectra that we are able to infer the nature of brown dwarf atmospheres and how they evolve overtime. Hence we are able to use them as unirradiated laboratories, which provides a valuable baseline for understanding extrasolar planet atmospheres.

Fundamental properties of brown dwarfs include their mass, radius, gravity, effective temperatures ($T_{\rm eff}$), and elemental abundances (see review in Kirkpatrick 2005; Marley and Robinson 2015). Robust masses can be derived through dynamical means (Dupuy and Liu, 2017) and radius is inferred via distance and bolometric luminosity. Determining gravity, effective temperatures, and abundances for brown dwarfs can be more challenging than it is for stars due to the lack of clear atomic lines for which

classic single or multi-line spectral analyses can be performed. As such, atmospheric models which properly incorporate molecules and condensate species play a more important role in these determinations.

A common modeling approach for determining these properties is through comparisons of observations to grids of model spectra computed with self-consistent one-dimensional radiative-convective equilibrium models (e.g., Allard *et al.* 1996; Marley *et al.* 1996; Burrows *et al.* 2001) or using more recent grid-fitting methods (Zhang *et al.*, 2021a,b). This approach typically relies upon the use of a priori physical and chemical assumptions such as thermochemical equilibrium, molecular/atomic abundances, assumed atmospheric chemistry paradigms, and 1D radiative-convective equilibrium (Burrows *et al.*, 2001; Marley and Robinson, 2015). These assumptions are made to reduce the dimensionality of the inference problem to just a handful of parameters such as $T_{\rm eff}$, $\log(g)$, and a composition parameter like metallicity $[M/H]$ (in some cases, alpha-element enhancement e.g. Husser *et al.*, 2013).

A few key issues arise with this method. First, the low model dimensionality restricts any inference solely to the dimensions specified for the pre-computed grid. Second, the choice of inference tool is often not rigorous and typically does not account for grid-interpolation uncertainties (e.g., often a simple chi-square type minimizer is combined with a multi-linear-type interpolater) and can result in artificially precise constraints. Thirdly, often times the overly restrictive assumptions lead to poor model spectra fits to the data (e.g., Patience *et al.* (2012)), leading one to question the validity of the self-consistent modeling assumptions. Zhang *et al.* (2021a,b) sought to remedy the second and third issues through the use of a modernized self-consistent grid (Marley *et al.* (2021b)) combined with the `Starfish` tool (Czekala *et al.* (2015b)), which attempts to account for the finite model grid spacing, interpolation uncertainties, and data-model misfits. However, such an approach is still restricted to a priori

physical assumptions within the grid itself.

A more flexible alternative known as atmospheric retrieval, has shown success in providing robust model-data fits to low resolution spectral observations of T and L dwarfs (Line *et al.*, 2014, 2015; Burningham *et al.*, 2017; Gonzales *et al.*, 2020). Originally developed to determine temperatures and abundances from spectral soundings of the Solar System planets (Fletcher *et al.*, 2007; Irwin *et al.*, 2008; Greathouse *et al.*, 2011), this technique relies on the use of a forward radiative transfer model that relaxes many of the self-consistent grid model assumptions at the expense of requiring many free parameters. The fundamental philosophy of the retrieval approach, in contrast to the grid approach, is that much of the physical/chemical mechanisms operating in low temperature atmospheres are not understood well enough to build accurate, fully self-consistent models. The aim of atmospheric retrieval is to directly determine, from the spectra the vertical temperature profiles and atmospheric composition. This approach has recently become prolific in the extrasolar planet atmosphere studies (e.g., see review by Madhusudhan (2019)).

Line *et al.* (2015) applied the atmospheric retrieval approach to low resolution SpeX data of the benchmark late-T dwarfs, Gl 570D and HD 3651B. Late-T dwarfs were specifically chosen to mitigate the impact of uncertain cloud properties and the presentation of strong molecular absorption features from water and methane. Using a radiative transfer forward model with $\sim$30 free parameters combined with Markov Chain Monte Carlo (MCMC) inference (Foreman-Mackey *et al.*, 2013), they were able to obtain bound constraints on the molecular mixing ratios for [H_2O, CH_4, NH_3 and Na+K], the vertical thermal profiles (temperature vs. pressure), gravity, and photometric radii (given the parallactic distances). The key findings were (1) that ammonia abundance could be constrained from low-resolution near-infrared spectra alone, a surprise given the lack of obvious visual spectral features (typical of

longer wavelengths Saumon *et al.* 2006 or higher resolutions (Canty *et al.*, 2015)); (2) the retrieved molecular (and alkali) abundances were consistent with self-consistent chemical predictions (albeit constant-with-altitude mixing ratios were assumed in the retrieval); (3) derived metallicities and carbon-to-oxygen ratios were consistent with their host star abundances; and (4) the vertical thermal temperature profiles agreed with radiative-convective equilibrium. Taken together, these findings lend support that the retrieval paradigm can be used as a complimentary tool to grid-modeling for inferring fundamental brown dwarf atmospheric properties.

Having validated the retrieval methodology against late-T benchmark systems, Line *et al.* (2017) performed a systematic retrieval analysis on the spectra of 11 late-T dwarfs (T7-T8, spanning 600 - 800K) available in the SpeX prism library (Burgasser, 2014). This uniform analysis found that (1) the large number of free parameters required in retrievals, compared to self-consistent grid models (27 vs. 4 parameters) is justified owing to their much better fits; (2) the T7/T8 atmospheres are cloud free (upper limits on the cloud optical depth of unity were obtained); (3) the temperature profiles for all objects were again consistent with radiative-convective equilibrium; (4) the retrieved gravities, radii, and inferred effective temperatures agreed with evolution model predictions; (5) abundances for ammonia, methane, and water were found to be constant with effective temperature but a strong decreasing trend in the alkali abundances was observed to occur with decreasing effective temperature; and (6) the late-T dwarf ensemble had somewhat lower metallicities and higher carbon-to-oxygen ratios than the local FGK stellar population. These findings provided a first look at the carbon-to-oxygen ratio and metallicities of a sample brown dwarfs as well as the first direct determination of the possible influence of alkali rainout on their abundances.

Building upon Line *et al.* (2015, 2017), Zalesky *et al.* (2019) extended the uni-

form retrieval analysis into the cooler Y-dwarfs. This sampled comprised eleven Y dwarfs and three T dwarfs as observed with the *Hubble Space Telescope*'s Wide Field Camera 3 (WFC3) (Schneider *et al.*, 2015). The conclusions were similar to the late-T results Line *et al.* (2017), finding that (1) the retrieved temperature profiles for most objects were consistent with radiative-convective equilibrium predictions; (2) water and methane abundances were consistent with equilibrium chemistry; (3) the ammonia abundances showed an upward rise with decreasing temperature, with scatter consistent with both equilibrium and quenched abundances; (4) constraints and/or upper limits on the alkali abundances consistent with rain-out predictions; (5) findings of very high gravities, pushing the limits of the evolution models; and (6) elemental abundance ratios broadly inline with those from the local FGK star population. They also compared the results of a self-consistent grid fit to the retrieval results finding that (1) the retrievals fit better and the large number of free parameters were justified, and (2) constraints on common parameters ($T_{\rm eff}$, $\log(g)$, metallicity, and radius) were inconsistent at 1σ.

Additional works by Burningham *et al.* (2017) and Gonzales *et al.* (2020) focused on determining the fundamental properties of L-dwarfs using similar retrieval methods. L-dwarfs are more complicated to characterize due to the presence of condensate clouds and additional higher temperature species (hydrides, oxides), and the reduced vertical grasp on the thermal structures. Overall these cloudy investigations showed that the retrieved temperature structures could be degenerate with the presence of clouds, but that plausible abundances of the hydrides/oxides could be retrieved, opening up the possibility of abundance determinations at higher temperatures.

In this work, we extend the late-T analysis in Line *et al.* (2017) to a broader sample of 50 T7-T9-dwarfs which were contained in a volume limited survey (Best *et al.* (2020)), including new IRTF SpeX spectroscopy (Zhang *et al.*, 2021a,b). Our work

here represents the largest uniform retrieval analysis on a nearly complete sample of late-T dwarfs, with a factor of 5 larger sample over the analysis in Line *et al.* (2017). As in the past papers of this series, we focus on late-T dwarfs as these have been shown to be largely free of influence from clouds and they present deep methane and water absorption features, enabling simultaneous carbon and oxygen constraints.

We follow closely the methodologies and analysis as in Line *et al.* (2017) and Zalesky *et al.* (2019). In Section 4.3, we briefly discuss the source of our data, and review our retrieval methodology in Section 4.4. Section 4.5 presents our retrieved constraints for our thermal structures (4.5.1), composition (4.5.2), and evolutionary parameters (4.5.3). Finally, we briefly summarize our findings in Section 4.6.

4.3 Data

Our entire dataset is derived from late-T dwarf IRTF SpeX prism observations (0.95 - 2.5 μm, R$\sim$120) largely described in (Zhang *et al.*, 2021a,b, see Table 3). There are a total of 55 objects with SpeX spectra with 39 available within the SpeX Prism Library, and 16 from our own observational campaigns. Briefly, the sample is comprised of objects from the volume-limited (d <25 pc) survey in Best *et al.* (2020) with our SpeX objects out to 20 pc. 54 of the 55 have well measured parallaxes and all spectra are flux calibrated using MKO H-band photometry. Our analysis, for uniformity purposes, also includes the 11 objects from Line *et al.* (2017). Due to low signal-to-noise, our final analysis excludes 5 objects, for a total of 50 in our analysis. This subset is highlighted in a color-magnitude diagram shown in Figure 4.1 with photometry and parallax measurements enumerated in Table 4.1. As in our past works we only analyze every 3rd spectral point as SpeX samples the line-spread shape with $\sim$2.5 pixels.

Table 4.1: Basic Properties of Our 50 Late-T Dwarfs

Name of Object	Spec. Type	$J_{\rm MKO}$ [mag]	$H_{\rm MKO}$ [mag]	$K_{\rm MKO}$ [mag]	Distance [pc]	J-Band Peak SNR
HD3651B	T7.5	$16.16^{+0.03}_{-0.03}$	$16.68^{+0.04}_{-0.04}$	$16.87^{+0.05}_{-0.05}$	$11.14^{+0.01}_{-0.01}$ **(4)**	73.7
WISE J004024.88+090054.8	T7	$16.13^{+0.01}_{-0.01}$	$16.56^{+0.02}_{-0.02}$	$16.55^{+0.05}_{-0.05}$	$14.01^{+0.53}_{-0.53}$ **(1)**	73.4
WISE J004945.61+215120.0PRZ0.5	T8	$17.63^{+0.13}_{-0.13}$	$18.09^{+0.14}_{-0.14}$	$18.06^{+0.14}_{-0.14}$	$24.81^{+1.48}_{-1.48}$ **(3)**	76.5
2MASS J00501994-3322402	T7	$15.65^{+0.1}_{-0.1}$	$16.04^{+0.1}_{-0.1}$	$15.91^{+0.1}_{-0.1}$	$10.57^{+0.27}_{-0.27}$ **(2)**	60.4
WISEPA J012333.21+414203.9	T7	$17.00^{+0.02}_{-0.02}$	$17.29^{+0.06}_{-0.06}$	$17.29^{+0.06}_{-0.06}$	$25.38^{+1.55}_{-1.55}$ **(1)**	67.7
WISEPC J022322.39-293258.1	T7.5	$17.1^{+0.05}_{-0.05}$	$17.3^{+0.11}_{-0.11}$	$17.59^{+0.08}_{-0.08}$	$12.39^{+0.4}_{-0.4}$ **(3)**	58.3
WISE J024124.73-365328.0	T7	$16.59^{+0.04}_{-0.04}$	$17.04^{+0.07}_{-0.07}$	N/A	$19.08^{+0.98}_{-0.98}$ **(3)**	66.1
PSO J043.5395+02.3995	T8	$15.92^{+0.01}_{-0.01}$	$16.29^{+0.02}_{-0.02}$	$16.73^{+0.05}_{-0.05}$	$6.84^{+0.07}_{-0.07}$ **(3)**	125.0
WISE J032547.72+083118.2	T7	$16.29^{+0.07}_{-0.07}$	$16.19^{+0.08}_{-0.08}$	$16.39^{+0.09}_{-0.09}$	$12.74^{+0.49}_{-0.49}$ **(3)**	66.1
2MASSI J0415195-093506	T8	$15.32^{+0.03}_{-0.03}$	$15.7^{+0.03}_{-0.03}$	$15.83^{+0.03}_{-0.03}$	$5.71^{+0.06}_{-0.06}$ **(2)**	223.0
WISEPA J045853.89+643452.9	T8.5	$17.13^{+0.07}_{-0.07}$	$17.45^{+0.11}_{-0.11}$	$17.74^{+0.1}_{-0.1}$	$9.16^{+0.3}_{-0.3}$ **(3)**	35.5
WISE J052126.29+102528.4	T7.5	$14.86^{+0.02}_{-0.02}$	$15.25^{+0.06}_{-0.06}$	$14.98^{+0.06}_{-0.06}$	$7.07^{+0.25}_{-0.25}$ **(1)**	93.8
UGPS J052127.27+364048.6	T8.5	$16.94^{+0.02}_{-0.02}$	$17.32^{+0.09}_{-0.09}$	$17.28^{+0.04}_{-0.04}$	$8.18^{+0.11}_{-0.11}$ **(3)**	60.5
WISE J061437.73+095135.0	T7	$16.43^{+0.02}_{-0.02}$	$16.64^{+0.06}_{-0.06}$	$16.49^{+0.06}_{-0.06}$	$17.61^{+0.62}_{-0.62}$ **(1)**	106.1
2MASSI J0727182+171001	T7	$15.19^{+0.03}_{-0.03}$	$15.67^{+0.03}_{-0.03}$	$16.69^{+0.03}_{-0.03}$	$8.89^{+0.07}_{-0.07}$ **(2)**	47.8
2MASS J07290002-3954043	T8pec	$15.66^{+0.08}_{-0.08}$	$16.05^{+0.1}_{-0.1}$	$16.5^{+0.1}_{-0.1}$	$7.92^{+0.52}_{-0.52}$ **(8)**	58.6
2MASS J09393548-2448279	T8	$15.61^{+0.09}_{-0.09}$	$15.96^{+0.09}_{-0.09}$	$16.83^{+0.09}_{-0.09}$	$5.34^{+0.13}_{-0.13}$ **(7)**	64.0
ULAS J102940.52+093514.6	T8	$17.28^{+0.01}_{-0.01}$	$17.63^{+0.01}_{-0.01}$	$17.64^{+0.02}_{-0.02}$	$14.6^{+0.36}_{-0.36}$ **(1)**	54.1
WISE J103907.73-160002.9	T7.5	$16.95^{+0.02}_{-0.02}$	$17.19^{+0.04}_{-0.04}$	$17.1^{+0.07}_{-0.07}$	$22.12^{+0.93}_{-0.93}$ **(1)**	35.6
WISE J105257.95-194250.2	T7.5	$16.84^{+0.02}_{-0.02}$	$16.99^{+0.06}_{-0.06}$	$17.07^{+0.06}_{-0.06}$	$14.73^{+0.48}_{-0.48}$ **(1)**	71.4
2MASS J11145133-2618235	T7.5	$15.52^{+0.05}_{0.05-}$	$15.82^{+0.05}_{-0.05}$	$16.54^{+0.05}_{-0.05}$	$5.58^{+0.04}_{-0.04}$ **(2)**	26.0
WISE J112438.12-042149.7	T7	$16.72^{+0.13}_{-0.13}$	16.37	16.32	$17.39^{+0.10}_{-0.10}$ **(1)**	85.4
2MASSI J1217110-031113	T7.5	$15.56^{+0.03}_{-0.03}$	$15.98^{+0.03}_{-0.03}$	$15.92^{+0.03}_{-0.03}$	$10.91^{+0.26}_{-0.26}$ **(5),(3)**	31.0
WISE J125448.52-072828.4	T8	$17.3^{+0.01}_{-0.01}$	$17.63^{+0.03}_{-0.03}$	$17.39^{+0.07}_{-0.07}$	$24.21^{+1.58}_{-1.58}$ **(1)**	25.0
WISE J125715.90+400854.2	T7	$16.88^{+0.02}_{-0.02}$	$17.12^{+0.06}_{-0.06}$	$17.16^{+0.07}_{-0.07}$	$17.51^{+0.55}_{-0.55}$ **(1)**	32.9
Ross 458C	T8	$16.69^{+0.02}_{-0.02}$	$17.01^{+0.04}_{-0.04}$	$16.9^{+0.06}_{-0.06}$	$11.51^{+0.02}_{-0.02}$ **(4)**	41.5
WISEPA J132233.66-234017.1	T8	$16.75^{+0.11}_{-0.11}$	$16.65^{+0.14}_{-0.14}$	$17.02^{+0.4}_{-0.4}$	$12.9^{+0.7}_{-0.7}$ **(3)**	31.5
ULAS J141623.94+134836.3	(sd)T7.5	$17.26^{+0.02}_{-0.02}$	$17.58^{+0.03}_{-0.03}$	$18.43^{+0.08}_{-0.08}$	$9.3^{+0.03}_{-0.03}$ **(4)**	52.0
WISEPC J145715.03+581510.2	T7	$16.82^{+0.02}_{-0.02}$	$17.16^{+0.06}_{-0.06}$	$17.22^{+0.07}_{-0.07}$	$21.41^{+2.61}_{-2.61}$ **(1)**	51.8
Gliese 570D	T7.5	$14.82^{+0.05}_{-0.05}$	$15.28^{+0.05}_{-0.05}$	$15.52^{+0.05}_{-0.05}$	5.88 **(4)**	31.7
PSO J224.3820+47.4057	T7	$17.1^{+0.02}_{-0.02}$	$17.43^{+0.06}_{-0.06}$	$17.06^{+0.06}_{-0.06}$	$20.2^{+1.22}_{-1.22}$ **(1)**	34.4
SDSS J150411.63+102718.4	T7	$16.51^{+0.01}_{-0.01}$	$16.99^{+0.05}_{-0.05}$	$17.12^{+0.08}_{-0.08}$	$21.69^{+0.71}_{-0.71}$ **(2)**	49.9
2MASSI J1553022+153236	T7	$15.34^{+0.03}_{-0.03}$	$15.76^{+0.03}_{-0.03}$	$15.94^{+0.03}_{-0.03}$	$13.32^{+0.16}_{-0.16}$ **(2)**	140.6
SDSS J162838.77+230821.1	T7	$16.25^{+0.03}_{-0.03}$	$16.72^{+0.03}_{-0.03}$	$16.63^{+0.03}_{-0.03}$	$13.32^{+0.16}_{-0.16}$ **(2)**	42.8
WISEPA J165311.05+444423.9	T8	$17.07^{+0.02}_{-0.02}$	$17.59^{+0.05}_{-0.05}$	$17.05^{+0.07}_{-0.07}$	$13.21^{+0.33}_{-0.33}$ **(3)**	38.7
WISEPA J171104.60+350036.8PRZ0.5	T8	$17.63^{+0.13}_{-0.13}$	$18.06^{+0.14}_{-0.14}$	$18.09^{+0.14}_{-0.14}$	$24.81^{+1.48}_{-1.48}$ **(3)**	32.1
WISEPA J174124.26+255319.5	T9	$16.18^{+0.02}_{-0.02}$	$16.31^{+0.04}_{-0.04}$	$17.02^{+0.2}_{-0.2}$	$4.67^{+0.06}_{-0.06}$ **(3)**	122.5
WISE J181329.40+283533.3	T8	$16.92^{+0.02}_{-0.02}$	$17.11^{+0.06}_{-0.06}$	$16.92^{+0.06}_{-0.06}$	$13.59^{+0.37}_{-0.37}$ **(1)**	54.2
WISEPA J185215.78+353716.3	T7	$16.33^{+0.02}_{-0.02}$	$16.72^{+0.06}_{-0.06}$	$16.5^{+0.06}_{-0.06}$	$15.06^{+0.66}_{-0.66}$	125.9
WISEPA J195905.66-333833.7	T8	$16.71^{+0.07}_{-0.07}$	$17.18^{+0.05}_{-0.05}$	$16.93^{+0.09}_{-0.09}$	$11.72^{+0.3}_{-0.3}$ **(3)**	60.2
WISE J200050.19+362950.1	T8	$15.44^{+0.01}_{-0.01}$	$16.13^{+0.04}_{-0.04}$	$15.85^{+0.01}_{-0.01}$	$7.62^{+0.17}_{-0.17}$ **(1)**	67.3
WISEPC J215751.38+265931.4	T7	$17.05^{+0.02}_{-0.02}$	$17.49^{+0.04}_{-0.04}$	$17.34^{+0.06}_{-0.06}$	$15.92^{+0.56}_{-0.56}$ **(1)**	87.0
WISEPC J220922.10-273439.5	T7	$16.6^{+0.02}_{-0.02}$	$16.95^{0.06+}_{-0.06}$	$17.35^{+0.06}_{-0.06}$	$13.81^{+0.72}_{-0.72}$ **(1)**	75.2
WISEPC J221354.69+091139.4	T7	$16.77^{+0.02}_{-0.02}$	$17.12^{+0.06}_{-0.06}$	$17.11^{+0.06}_{-0.06}$	$19.19^{+1.14}_{-1.14}$ **(1)**	77.0
WISEPC J222623.05+044003.9	T8	$16.90^{+0.02}_{-0.02}$	$17.24^{+0.09}_{-0.09}$	$17.45^{+0.07}_{-0.07}$	$18.38^{+1.99}_{-1.99}$ **(3)**	69.7
WISEPC J225540.74-311841.8	T8	$17.33^{+0.01}_{-0.01}$	$17.66^{+0.03}_{-0.03}$	$17.42^{+0.05}_{-0.05}$	$14.14^{+0.84}_{-0.84}$ **(3)**	50.6
WISEPC J231939.13-184404.3	T7.5	$17.56^{+0.02}_{-0.02}$	$17.95^{+0.05}_{-0.05}$	$18.26^{+0.08}_{-0.08}$	$11.75^{+0.43}_{-0.43}$ **(1)**	31.3
ULAS J232123.79+135454.9	T7.5	$16.72^{+0.03}_{-0.03}$	$17.15^{+0.03}_{-0.03}$	$17.16^{+0.01}_{-0.01}$	$11.96^{+0.34}_{-0.34}$ **(3)**	51.9
WISEPC J234026.62-074507.2	T7	$16.08^{+0.03}_{-0.03}$	$16.4^{+0.03}_{-0.03}$	$16.51^{+0.06}_{-0.06}$	$20.92^{+1.36}_{-1.36}$ **(3)**	95.9
WISEPC J234841.10-102844.4	T7	$16.63^{+0.02}_{-0.02}$	$16.99^{+0.06}_{-0.06}$	$16.84^{+0.06}_{-0.06}$	$14.79^{+0.83}_{-0.83}$ **(1)**	71.3

References for both spectral types and parallax distances in this table are (1) Best *et al.* (2020), (2) Dupuy and Liu (2012), (3) Kirkpatrick *et al.* (2019), (4) Gaia Collaboration *et al.* (2018), (5) Tinney *et al.* (2003), (6) Faherty *et al.* (2012), (7) Burgasser *et al.* (2008), (8) Faherty *et al.* (2012), (9) Leggett *et al.* (2012)

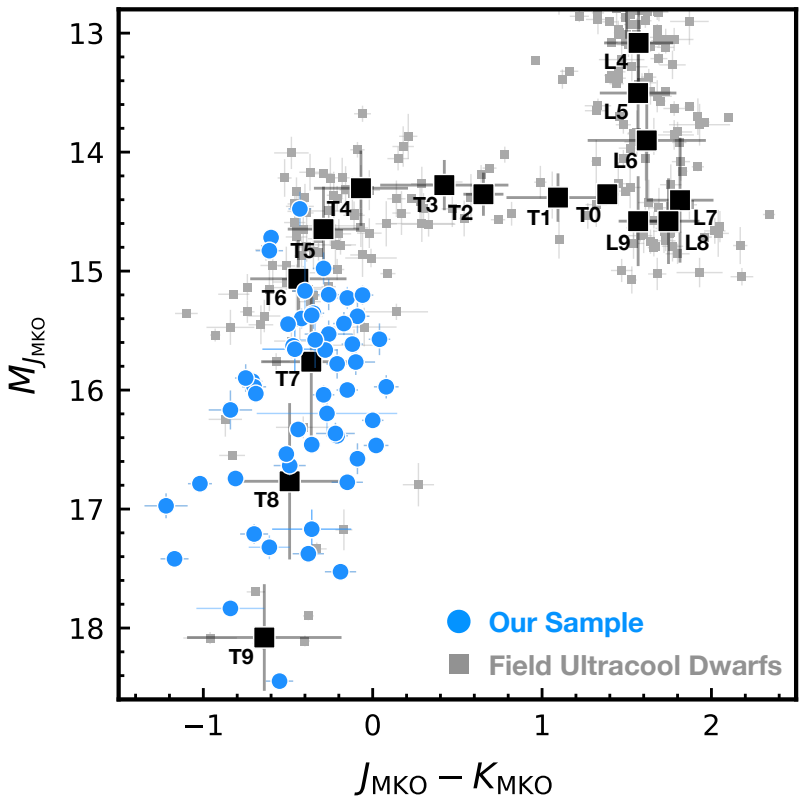

Figure 4.1: A color-magnitude diagram of a population of field brown dwarfs (Best *et al.*, 2018, 2020), and our sample of brown dwarfs from this study (T5-T9). This collective ensemble shows L and T dwarfs, in descending order from the top of the diagram to the bottom.

4.4 Methods

Our retrieval framework follows closely that described in Line *et al.* (2017) and Zalesky *et al.* (2019). The model computes the thermal emission spectrum of a brown dwarf and includes 31 free-parameters to describe the atmosphere: constant-with-altitude volume mixing ratios (VMR's) for: H_2O, CH_4, NH_3, CO, CO_2, H_2S, Na, and K (8 in total), gravity, radius-to-distance scale factor $(R/D)^2$, 15 independent temperature-pressure (TP) profile points implemented within a Gaussian-Process-like smoothing framework, and a simple cloud parameterization (Burrows *et al.*, 2006); summarized in Table 4.2.

Table 4.2: Retrieved Parameters

Parameter	Description
log (f_i)	log of the Volume Mixing Ratio (VMR) of a gas species that is constant with altitude. Gases that are considered include H_2O, CH_4, CO, CO_2, NH_3, K, and Na
log (g)	log of surface gravity [cm s^2]
$(R/D)^2$	Radius-to-distance scale factor [R_{Jup}/pc]
T_i	Temperature (in Kelvin) at a given pressure level
$\Delta\lambda$	Wavelength calibration uncertainty [nm]
b	errorbar inflation exponent
γ, β	TP-profile smoothing hyperparameters (eq. 5, Line *et al.* (2015))
κ_{P_0}, P_0, α	Cloud opacity profile parameters (eq. 1, (Line *et al.*, 2017), cloud base opacity, cloud base pressure, cloud fractional scale height)

Compared to our previous work we have made several adjustments to this model. We have separated the alkali constraints into distinct Na and K free parameters (as opposed to Na+K fixed at a solar ratio), removed H_2S due to low predicted abundances at these temperatures, and updated the alkali metal wing profiles (Allard *et al.*, 2016). All other opacity sources are identical to Line *et al.* (2017) and Zalesky *et al.* (2019). Model cross-section sampling is used at a constant R=10000, a resolution proven sufficient for interpreting SpeX brown dwarf observations (Line *et al.*, 2015). Parameter prior ranges are the same as those of Line *et al.* (2015) which are restated in Table 4.3. Fits were performed as in the mentioned previous studies using the `emcee` package (Foreman-Mackey *et al.*, 2013) with 224 walkers run out to 60,000 iterations. To assure convergence several test cases were ran to between 120K and 1 million iterations with no significant differences in model posteriors. `emcee`, like all

MCMC-based methods, requires an initial guess to initiate the walkers. The initial guess is based on a "Gaussian-ball" about a lose by-eye fit to the spectra of each object. The final solutions were found insensitive to the initial guess as was the case in previous publications.

To reduce computational runtime for such a large number of objects, our radiative transfer core (Appendix A in Lacis and Oinas (1991)) was rewritten to make use of GPUs. This was done using the Anaconda Numba `guvectorize` framework on NVIDIA Tesla V100 GPUs. Forward model times improved by a factor of $\sim$100 (0.01s or so per model, at an R=10,000 over the 0.95 - 2.5μm wavelength range). Given the limited memory of the GPUs (32 GB), we could only run up to 16 simultaneous CPU threads at a time. The overall computational improvement between this work and that of Line *et al.* (2017) is about a factor of 10 (about 6 hours to hit 60,000 iterations). GPU and CPU routines were tested to produce identical model spectra with no impact on any science results.

4.5 Results & Discussion

As it is largely uninformative to show the full posteriors, and discuss each individual object (available in the online version of this work), here we simply summarize

Table 4.3: Parameter Priors

Parameter	Prior
log (f_i)	$>$ -6, Σf_i=1
log (g), $(R/D)^2$	$M < 80 M_{Jup}$
$\Delta\lambda$	(-10 , 10)
10^b	$(0.01\times\min(\sigma_i^2)$, $100\times\max(\sigma_i^2))$
γ	Inverse Gamma($\Gamma(\gamma;\, \alpha,\, \beta)$), α=1, β= 5 $\times 10^{-5}$
$\log(\kappa_C)$, $\log(P_0)$, α	(-12, 0), (2.3, 2.8), [0,10)

the key results broken down by thermal structure, composition (molecular abundance trends/chemistry and elemental abundances), and evolutionary parameters.

Figures 4.2 and 4.3 provide a snapshot of the fits and temperature-pressure profiles, respectively, of a sub-sample of representative objects. The best fits and temperature profiles for all objects in our sample are provided at the end of this chapter (Figures 4.10 and 4.11). As has been discussed in previous papers in this series, the visual quality of the model fits in Figures 4.2 and 4.10 are substantially better than those by more traditional grid-based models, with residuals following only the uncertainty in the data itself with little other deviation.

Table 4.4 summarizes the nominal constraints for the key properties of individual objects. As in our past works, the effective temperatures are derived by integrating over an ensemble of best fits for each object, extrapolated out to between 0.7 - 20 μm, and radius is derived from the retrieved $(R/D)^2$ scale factor and the measured distances (from Table 4.1). The elemental C and O abundances are derived from the retrieved molecular abundances (more details below). When comparing the retrieved quantities to those predicted from self-consistent grids (given an effective temperature and gravity and assuming solar abundance chemistry and cloud free), we refer to those produced by the ScCHIMERA model Piskorz *et al.* (2018); Arcangeli *et al.* (2018); Mansfield *et al.* (2018); Kreidberg *et al.* (2018); Gharib-Nezhad and Line (2019); Zalesky *et al.* (2019); Colón *et al.* (2020); Beatty *et al.* (2020); Meisner *et al.* (2021), with additional eddy-mixing for the NH_3-N_2 and CO-CH_4 chemistry (Zahnle and Marley, 2014).

4.5.1 Thermal Structures

Late-T type brown dwarfs are ideal for temperature profile retrievals due to the lack of obscuring, optically thick condensate clouds that would otherwise limit the

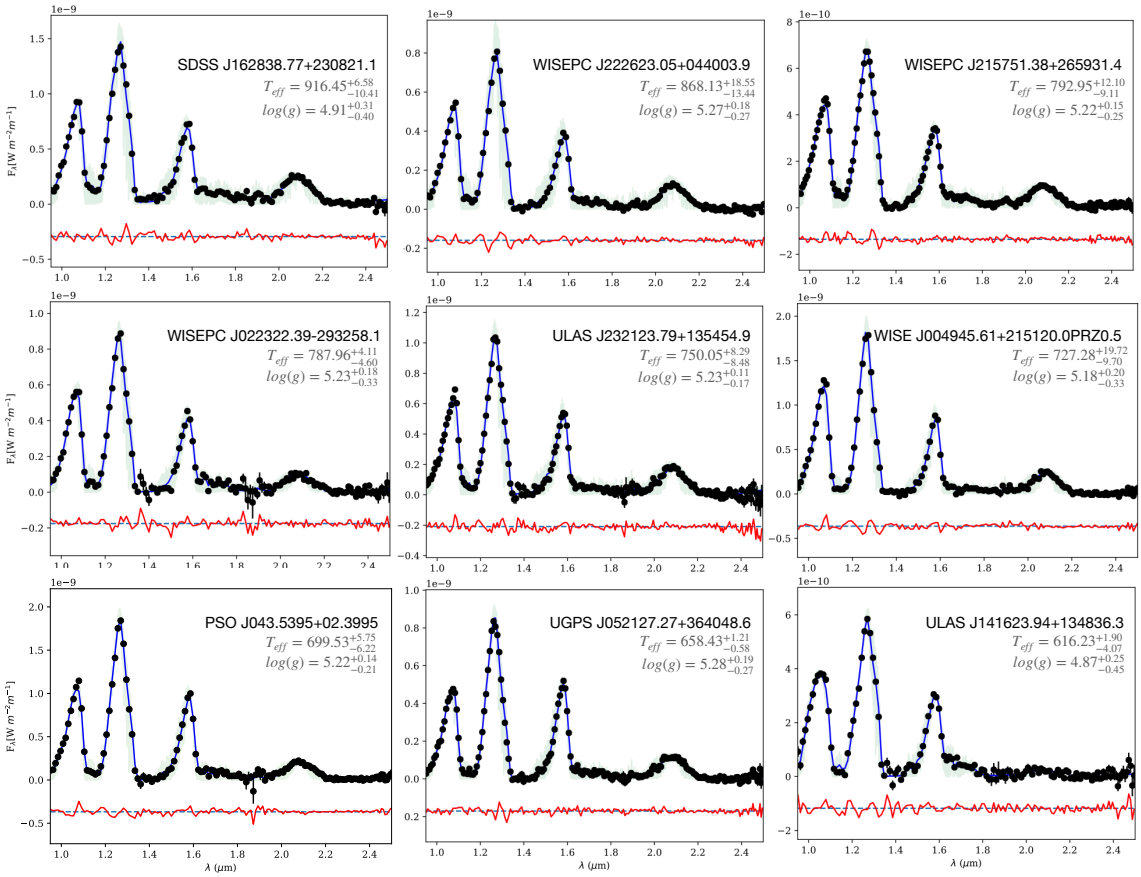

Figure 4.2: Subset of the data (black round points with errors) and resulting fit (binned best fit in blue, residuals about the dashed line below in red). In blue is a higher resolution (R∼25,000) representation of the best fit spectrum. The effective temperature and gravity constraints are given in the upper right hand corner of each panel.

range of pressures that could be probed via spectroscopy. The high degree of flexibility of the thermal profile parameterization allows us to compare thermal profiles derived directly from observational spectra against assumptions often made in more self-consistent models. Since the thermal structure is a reflection of the total energy balance, identifying similarities and differences between retrieved profiles and those predicted from 1D radiative-convective-thermochemical equilibrium (RCE) for such a large number of objects enables us to assess and quantify potential sources of heating outside of the standard RCE assumptions.

Figure 4.3 summarizes (see Appendix, Figure 4.11 for all objects in the sample) the retrieved thermal structures for nine representative objects (red) compared with 1D RCE predicted TP profiles (blue). Uncertainties for the RCE temperature profiles are derived by propagating uncertainties in the retrieved log(g), $T_{\rm eff}$, metallicity and C/O. Overlaid for context are condensation curves for several notable condensate species (Morley *et al.*, 2012, 2014). As in previous studies we reiterate that our SpeX observations largely probe only the region between 0.1 and 10bars with the rest of the profile's constraints being largely dependent upon the smoothing prior; any structure outside this range should be interpreted with caution.

We find that the uncertainties on the retrieved profiles are similar to previous studies, with 1σ errors on the order of 100K with larger deviations being owed to larger uncertainties on the spectra themselves (Line *et al.*, 2015, 2017; Zalesky *et al.*, 2019). While some objects appear to be in agreement with the assumption of 1D RCE to 2σ (see WISEPC J0223 in Figure 4.3, middle left) 18 objects are discrepant with the 1D RCE predicted profiles. There is a systematic offset whereby the retrieved profiles for a given $T_{\rm eff}$and log(g) are hotter (at a given pressure) than the corresponding 1D RCE predicted profiles. In addition to this systematic offset, 9 objects display an interesting "kink" in the profiles near the 10bar pressure level.

We first tested if the overall offset was physical or a simple result of over or under-constraining either model. To make clear, the error bounds for the grid model are calculated by taking the constraints from the retrieval model and propagating them into error bounds for the grid's thermal profile using several key parameters: $T_{\rm eff}$, log(g), metallicity, C/O, as well as a reasonable range of K_{zz} values for late-T dwarfs. We tested the robustness of these constraints by artificially inflating the errors of the retrieval results by 1σ to see if the resulting thermal profiles would then overlap. Inflating the errors in this way removed the evidence of any kink structure near 10bars.

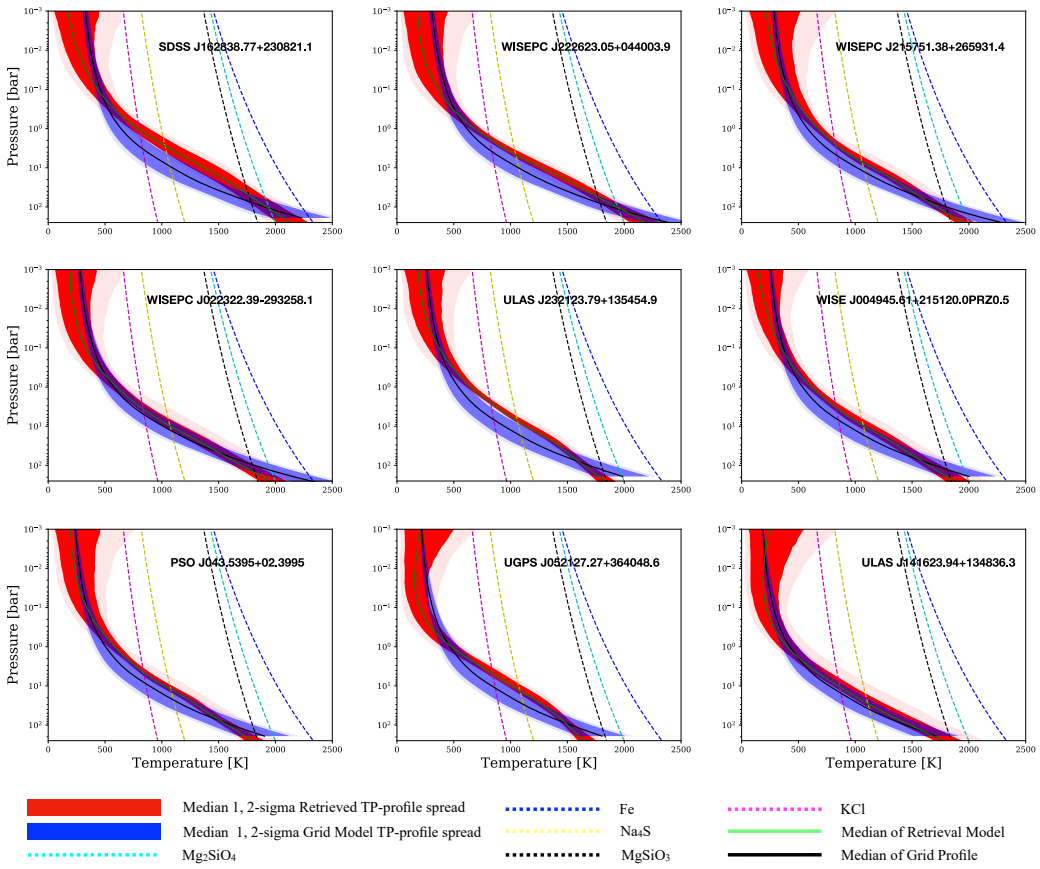

Figure 4.3: TP-profiles of representative T dwarfs of our collection of 50 objects. The thermal profiles indicated here are of the retrieved objects (in red), and of grid models (in blue, see text) that they closely compared to based on their similarities in a mix of T_{eff}, log(g), C/O, and metallicity parameters. For each of the thermals profiles, both 1 and 2σ confidence intervals are shown. Equilibrium condensation curves of Mg_2SiO_4, Fe, $MaSiO_3$, Na_2S, and K are shown by the cyan, blue, black, yellow, and magenta dashed lines, respectively.

As this pressure range is near the edge of the contribution functions that our spectra probe, the presence of such a feature should be interpreted with caution.

The most likely reason for the retrieval profiles being systematically hotter than the 1D RCE profiles is owed to how $T_{eff}$is computed in the retrieval model coupled with the grid-based models being forced onto RCE. As explained in previous papers, a sample of several thousand spectra are taken from the posterior and propagated out to roughly 20μm. This flux is then integrated and $T_{eff}$is computed from L_{Bol}.

However, its important to note that a majority of the output flux for these T dwarfs lie at longer wavelengths outside the range of our SpeX dataset. Since we cannot detect molecules such as CO or CO_2 in our SpeX data, these major absorptive species at longer wavelengths may not be properly included in these models which stretch out to 20μm. Therefore the result may be an over-estimate for the flux and thereby $T_{\rm eff}$. This estimate for $T_{\rm eff}$is then used as an input into the 1D RCE model which, while at similar $T_{\rm eff}$, may be limited by being forced onto a strict 1D RCE prescription for the PT profile. Another complicating factor is that, as shown in Figure 4.8 and discussed in Section 4.5.3, some objects can be offset by several hundred kelvin depending upon the choice for priors on log(g).

If we assume the offset is physically motivated, then it might be possible that these late-T dwarfs may be impacted by the presence of iron-silicate condensate clouds. To test this we calculated the cloud column optical depth, τ_{cld} by integrating the random draws of our retrieved opacity profile from our cloud model. Figure 4.9 shows the result for two representative objects (all targets available in the online version), where the most likely values of τ_{cld} are far below unity. This suggests that optically thick clouds do not strongly affect our dataset. Even targets such as ROSS 458C, which has been seen in previous works to better fit grid-based models that incorporate these clouds (Burgasser *et al.*, 2010; Burningham *et al.*, 2011; Morley *et al.*, 2012), still strongly favors a cloud-free retrieval result.

Additionally, these targets may have additional heating mechanisms in their atmospheres that could be driving the system away from pure radiative-convective equilibrium. However it seems more likely that differences in the physical and chemical assumptions between the 1D RCE models and retrieval can bias the thermal profile using the same $T_{\rm eff}$.

4.5.2 Atmospheric Composition

Molecular Abundances

A key goal of this investigation is to develop a large, diagnostic dataset of retrieved molecular abundances across the late-T spectral class to serve as a baseline unirradiated comparison for directly imaged and transiting exoplanets. For these objects, species such as H_2O, CH_4, NH_3, and K are the most readily accessible over the SpeX wavelength range. The change in the abundances of these gases with $T_{\rm eff}$are diagnostic of the driving physical and chemical processes in brown dwarf atmospheres (Burrows and Sharp, 1999; Lodders and Fegley, 2002; Sharp and Burrows, 2007).

Figure 4.4 shows the behavior of the retrieved molecular abundances with temperature combined with the retrieved Y-dwarf molecular abundances from Zalesky *et al.* (2019) (cyan). Overlaid for context are predictions from the 1D RCE models over a range of atmospheric metallicity and C/O ratios. Unless labeled otherwise each curve assumes a solar composition ([M/H]=0, C/O=0.55). To compute effective atmospheric abundances from the 1D RCE models, gas volume-mixing-ratios (VMRs) are averaged over the 1 - 30bar pressure levels based on the range of pressure levels probed by the SpeX spectra. The exact retrieved abundances for all 50 objects are enumerated in the Appendix under Table 4.4. We find that the precision of our constraints is slightly improved relative to Zalesky *et al.* (2019) as expected from the increase in quality of data. For all species we find that our abundances are constrained to within $\sim$0.25dex at 1σ.

For both H_2O (top left) and CH_4 (lower left) there is a trend of decreasing abundance with higher $T_{\rm eff}$, consistent with what was found in Zalesky *et al.* (2019). We are able to confirm that this trend extends beyond two late-T dwarfs and continues with increasing temperature though there is considerable spread. For H_2O, this

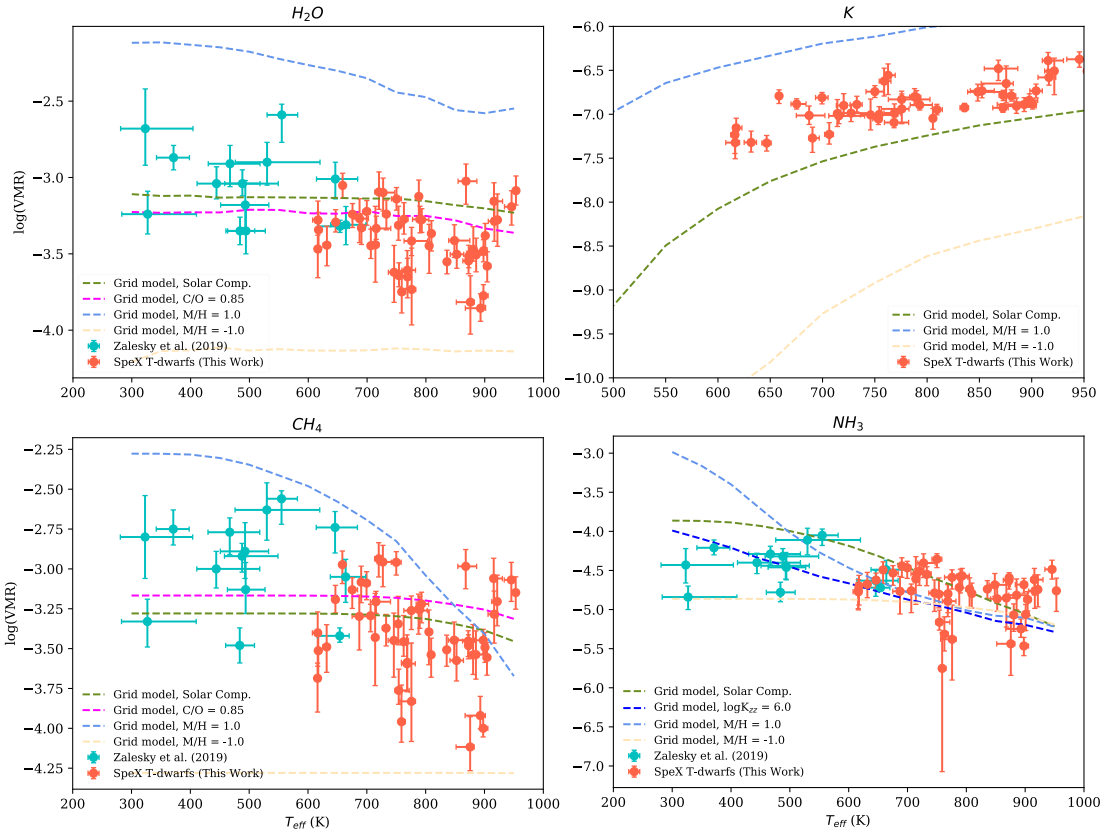

Figure 4.4: Molecular abundances (expressed as log of the VMRs) of H_2O, CH_4, NH_3, and K plotted against T_{eff} for T dwarfs from this study (color:tomato) and brown dwarfs from Zalesky *et al.* (2019). For K, objects from Zalesky *et al.* (2019) are not included because that work considered Na+K as one alkali species, whereas herein we are treating them as individual species. The four sub-plots show how the molecular and alkali abundances of each species varies with T_{eff}. All the modelled molecular abundance trends are defined by log(g) = 5.0 and solar composition (M/H = 0.0, C/O = 0.5), and we assume equilibrium chemistry unless otherwise specified. We observe that the overall trends of water, methane, and ammonia are consistent with solar chemistry curve models.

spread is consistent with what is expected for these objects between a metallicity of 0.1 to 10 times solar and various C/O ratios as shown. As there is no known physical mechanism for why these two populations should be disparate in their water content, and given the error bounds and sampling size of the Y-dwarfs, it seems likely that such a trend is a result of low-sampling from this population. Future studies which could retrieve higher precision ($\sim$0.25dex) water abundances for brown dwarfs between 300-700K would strongly help either confirm or deny such a trend with T_{eff}.

For CH_4, most objects are within the predicted ranges of from the grid model. However, there are interestingly several objects with T_{eff}between 900-1000K which deviate from this assumption. This would require either anonymously high C/O ratios (some well-above 1.0), high metallicities, or both when compared to the curves from the grid model. These objects must be interpreted with caution for two reasons. First is that only 4 objects lie above the expectations from the grid model at only 1σ. Second, we emphasize such curves do not represent all possible combinations of parameter space. Despite this, there may be physical motivation for finding objects with anomalously high CH_4 abundances near 900K. It has been well studied that L and T dwarfs have both theoretical and observational evidence for the presence of CO in their photospheres driven by disequilibrium convective mixing (Noll *et al.*, 1997; Oppenheimer *et al.*, 1998; Saumon *et al.*, 2003; Golimowski *et al.*, 2004; Burgasser *et al.*, 2006b; Geballe *et al.*, 2009; Sorahana and Yamamura, 2012; Leggett *et al.*, 2012). More recently, Miles *et al.* (2020) found that the CO constraints for several brown dwarfs between 250-700K suggest that at lower temperatures ($\sim$250K) there is evidence for stronger mixing (higher CO, less CH_4) and at higher temperatures ($\sim$700K) there is evidence for reduced mixing strength (less CO, more CH_4). It is possible that we could be seeing objects that follow such a trend up to higher temperatures, however given the low number of objects in our sample and the precision

of our constraints, this is largely inconclusive. There is a wealth of available early T and L spectral class objects to study to confirm such a trend, but have the added complication of obscuring condensate clouds which is beyond the scope of this work.

We find that the retrieved NH_3 abundances are largely consistent with grid model expectations, with the exception of 9 objects which show additional NH_3 near 900K. This result is surprising given that the onset of ammonia is the defining feature of the Y-dwarf spectral class. While again this could be a result of small number sampling, it is possible that this could be evidence for enhanced mixing strength at higher temperatures resulting in an excess of NH_3 compared to expectations from equilibrium. While Miles *et al.* (2020) found no evidence for enhanced mixing at these temperatures, disequilibrium abundances of NH_3 have been detected in the past (Saumon *et al.*, 2007; Geballe *et al.*, 2009; Leggett *et al.*, 2010, 2015).

As was found in Part II and III, there is a strong systematic trend of decreasing potassium between the late-T to early-Y spectral types as a result of equilibrium rainout chemistry removing aluminium and silicate reserves near 1300K, leading to a delayed depletion of Na+K closer to $T_{eff}\sim$700K where they condense into KCl and Na_2S. Figure 4.4 shows the the trend with our larger sample which continues to indicate a steadly decreasing trend with decreasing T_{eff}, with potassium abundances falling roughly 1 dex between -6.5 and -7.5 log(VMR) consistent with what was found in Parts II and III. We do not show the results from the Y dwarfs here as in that work, Na and K were treated as a single gas with most objects only providing upper limits.

While we are not able to fully explain the observed abundance trends with standard 1D RCE assumptions, it may indicate that some underlying physical or chemical process is not being taken into account in these models. Regardless, this sample of retrieved abundances provides a unique dataset to further explore the chemistry of

sub-stellar atmospheres.

Metallicity & Elemental Ratios

In addition to the molecular composition of a brown dwarf atmosphere, the total elemental abundance inventory, and ratios between those abundances, can assist in placing brown dwarfs in a larger context with their stellar and planetary-mass cousins. Stars and field brown dwarfs are expected to form via fragmentation and core-collapse of a molecular cloud. Thus one would expect their elemental inventories to be highly similar. In contrast, planets that are formed in disks might have a completely different elemental composition due to a wide variety of processing mechanisms, differential ice-lines and thus elemental ratios within the disk, and/or migration of the planet within the disk (e.g. Öberg *et al.*, 2011; Helling *et al.*, 2014). These mechanisms can change the elemental composition to range from anywhere from stellar composition (Fortney *et al.*, 2013; Mordasini *et al.*, 2016), to vastly different metal enrichment, and/or to have completely different C/O ratios, sometimes several factors greater or lesser than the host star (Madhusudhan *et al.*, 2014; Eistrup *et al.*, 2016). Identifying at what masses this dramatic compositional shift may occur for a large sample of brown dwarfs can better place brown dwarfs as a whole in a larger astronomical context.

As noted in previous studies in this series, the bulk of the metals found in brown dwarf atmospheres with $T_{\rm eff} \leq 1000$K are largely comprised of C and O contained in the water and methane content with a smaller amount of N stored in NH_3. The metallicity is computed as,

$$[M/H] = log(\frac{(M/H)_{\rm Tdwarf}}{(M/H)_{\rm solar}}) \tag{4.1}$$

where the metallicity of the T dwarf is taken to be the summation of the number

of elemental species included in the retrieval model. The C/O ratio is taken as,

$$\frac{C}{O} = \frac{\Sigma C}{\Sigma O} \sim \frac{CH_4 + CO + CO_2}{H_2O + CO + 2CO_2}. \tag{4.2}$$

Figure 4.5 shows the [M/H] compared against our computed C/O for both this study and those objects in Zalesky *et al.* (2019). For context a representative sample of local FGK stars are overlaid (dark red) (Hinkel *et al.*, 2014). As in Parts II and III, we note that we additionally weight our water abundance by a factor of 1.3 to account of the loss of oxygen to condensate rainout species such as enstatite and forsterite (Fegley and Lodders, 1994). We find that, in agreement with previous papers in this series, the broad-scale metallicities and C/O ratios for our brown dwarfs largely match both in value and in distribution that of the local FGK stellar population. The new population (largely green-orange color) seems to fill in the gap between our two previous late-T and early-Y populations. Additionally, we performed a two-dimensional, two-sample, Kolmogorov–Smirnov test and found a p-value of 0.18 between the brown dwarf and stellar populations (Press *et al.*, 1992). This suggests that our measurements display no statistically significant difference from the local FGK population. Though there is considerable scatter, there is a slight positive correlation between metallicity and $T_{\rm eff}$.

4.5.3 Effective Temperature & Gravity

A brown dwarf's effective temperature and gravity are highly diagnostic of both its age and evolutionary history (Burrows *et al.*, 2001; Baraffe *et al.*, 2003; Saumon and Marley, 2008). Given that our sample should be comprised of largely field-age brown dwarfs, deviations in the these parameters from evolutionary models serves as both a sanity-check for our retrieval model, but may also serve as a sign of youth if a particularly low surface gravity is found.

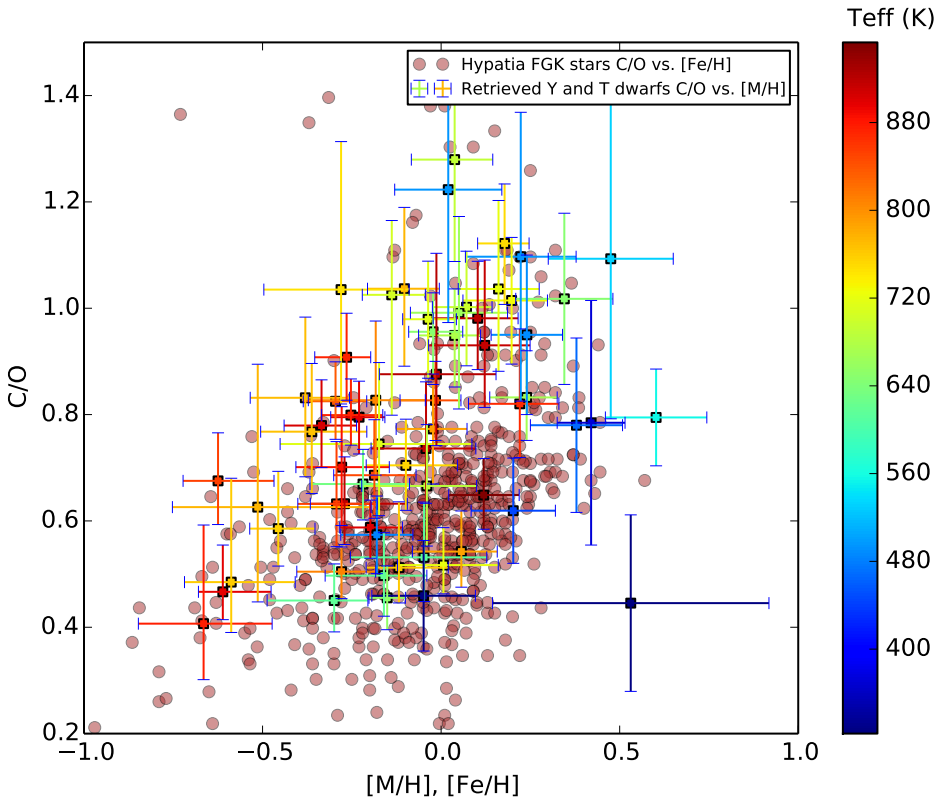

Figure 4.5: Bulk metallicity vs. C/O of our Y and T dwarfs ensemble. The brown dwarfs are color-coded according to their effective temperatures. For comparison with field stars, we overplot the brown dwarfs (C/O vs. [M/H]) with Hypatia FGK stars(C/O vs. [Fe/H]) that are within comparable parallax distances ($\leq$ 30 pc) to that of the brown dwarfs. The two populations have highly similar distributions owed to their similar formation environments.

Figure 4.6 shows our sample of late-T objects (orange) against results from Zalesky *et al.* (2019) (cyan). Over-plotted are evolutionary cooling curves for several different ages (blue-dashed, Marley et al. 2021, in prep). A large and extensive discussion for why the population from Zalesky *et al.* (2019) have anomalously high gravities is given in that paper.

Here we focus on our sample, which for a roughly forty objects agree with being near 1-3Gyr at 1σ. However, seven T dwarfs appear to have lower surface gravity values compared to the rest of the objects by several sigma with ages of near 0.1Gyr.

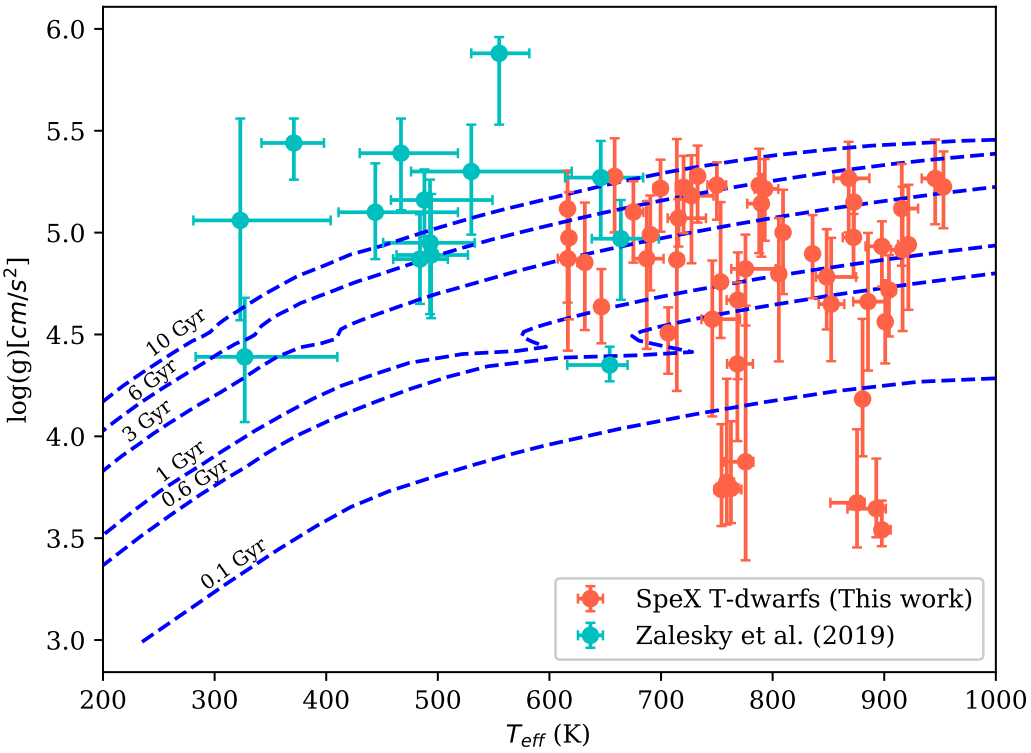

Figure 4.6: T_{eff} vs. log(g) for our collection of early Y dwarfs and late-T dwarfs. Here we notice that we almost have a handful of T dwarfs with low surface gravity values while Y dwarfs tend to have higher gravity values. Based on evolutionary models from (Marley et al. (2020), in prep) (shown by blue dashed curves), T dwarfs having the lowest log g values would be relatively young (∼100 Myr) while Y dwarfs having the highest log g would be relatively old (∼12 Gyr). Most of the objects above the 10 Gyr curve are considered atypical although their high gravities can be justified by the logic that under-estimations of gravities that are done in grid models (Schneider *et al.*, 2015; Zalesky *et al.*, 2019).

Additionally several objects are within 1σ of being consistent with a 10Gyr age. Both of these ages are unusual given our sample and necessitate a sanity check of our retrieval model.

The seven youngest objects are WISE J1254, PSO-J224, ROSS-458C, WISE-J1257, WISE-J1322, WISE-J1959, and WISE J0325. All the aforementioned T dwarfs, with the exception of ROSS-458C, have relatively low water and methane abundances. Furthermore, all seven of these T dwarfs have very low ammonia abundances. This observation of brown dwarfs exhibiting low gravities *and* metallicites is highly atypical (Helling and Casewell, 2014; Yuan *et al.*, 2011; Helling and Casewell, 2014). To test the credibility of the surface gravity constraint, we conducted an experiment on both the lowest gravity object (WISE 0325) and on one of our two highest gravity objects (2MASS 0729) by varying their gravity priors.

Metallicity - Surface Gravity Relationship

In this test we took a representative object that had both a relatively high and low log(g) constraint. The low-gravity object, WISE 0325, was used to perform a retrieval with a "full" log(g) prior range of $0 \leq \log(g) \leq 6$ compared to a retrieval done with a "constrained" log(g) prior range of $4.3 \leq \log(g) \leq 6$. The high-gravity object, 2MASS 0729, was set to $0 \leq \log(g) \leq 4.3$ while the full range was maintained at $0 \leq \log(g) \leq 6$. In the constrained cases, the gravity ranges were deliberately restricted to lower and higher gravity ranges to see how the retrieval results changed if forced to be in agreement with the system's likely true age.

Figure 4.7 shows stair-pairs plots for both object's molecular abundance and gravity constraints in both the constrained (red) and unconstrained (blue) test cases. The constraint on log(g) shows a strong several-sigma offset between the two cases and importantly that the posterior in the constrained case is highly non-Gaussian as it is

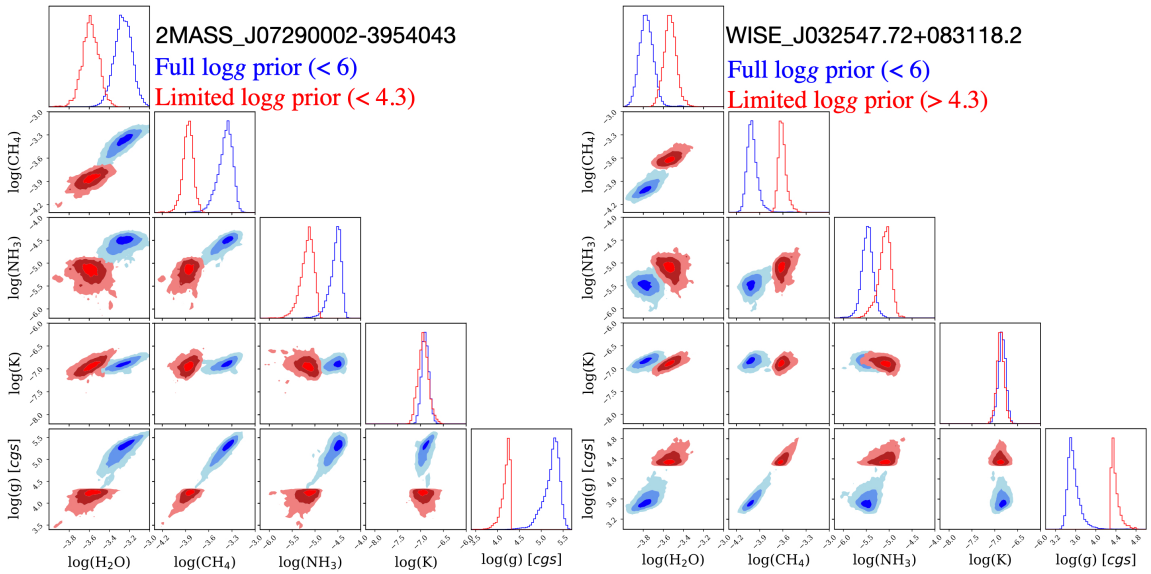

Figure 4.7: Corner plot posteriors of 2MASS-J072290002 (highest gravity object) and WISE-J032547.72 (lowest gravity object). This is based on a test of constraining priori ranges of gravity for the two objects. Gravity range restrictions affect gravity's correlation with the other gas species. Limited logg priors' results for surface gravity lean more toward full log(g) priors' results.

pushing up against the limit of the prior. This indicates that, despite being "guided" to a lower/higher gravity in-line with field-age expectations, the spectrum itself has features which favor a higher/lower gravity than the priors allow.

Alterations in gravity prior ranges also impact the posteriors of other species like water, ammonia, and methane as the parts of the spectra where gravity would be most constraining are the same regions where the absorption of these gases are most prominent. Potassium notably appears to be insignificantly affected by changes in gravity. This is likely because potassium absorption features only affect a small portion of the spectrum between 0.95-2.5 μm, mostly in the Y and J bandpasses. This high correlation between gravity and metallicity also impacts the constraints on the thermal profiles as well. as shown in Figure 4.8.

Though a large majority of our objects are within reasonable expectations for field age brown dwarfs, the age estimates from several of these objects are highly

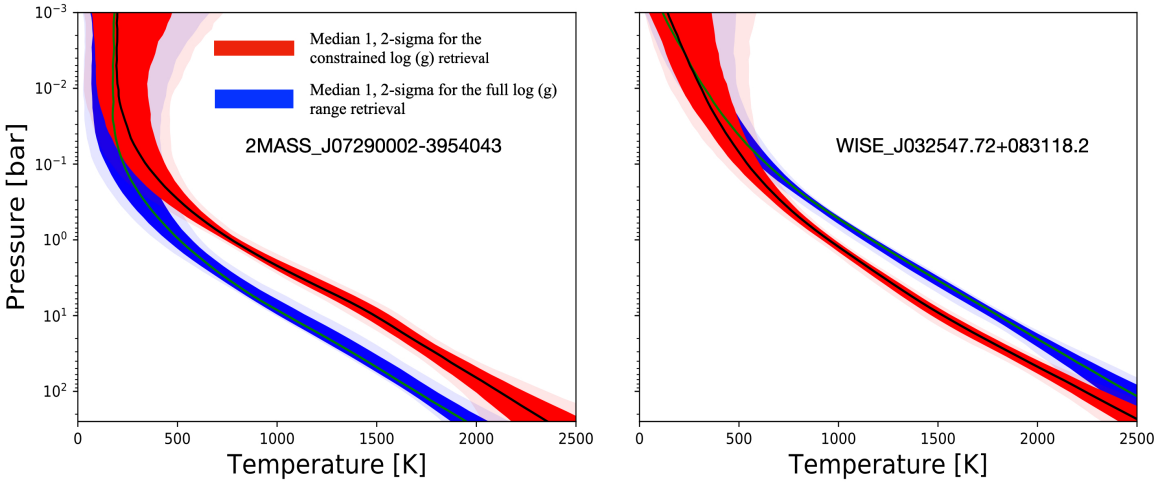

Figure 4.8: TP-profiles comparisons of limited and full logg ranges retrievals for 2MASS-J07290002 and WISE-J032547. Restrictions in gravity ranges influence the shape of thermal profiles.

nonphysical being either less than 0.1Gyr or older than the age of the Universe in the most extreme cases. These results show that retrievals, 1D RCE models, and comparison/sanity checks between both are needed to fully understand the atmospheres of brown dwarfs. One area this is possible is with different types of benchmark systems, where either metallicity or age is constrained. In our sample we have three systems which are in a binary (ROSS 458B,HD 3651B) or quaternary (Gliese 570D), all of which are within 1σ for their stellar companion's age and metallicity, giving confidence to the reliability of our retrieval results despite the many caveats of using this technique.

4.6 Summary & Conclusions

Below we list the key conclusions of our analysis:

1. For most of our sample, we find that the retrieved thermal structures are in agreement with with predictions from self-consistent grid based approaches (Figure 4.11). However, 18 objects have retrieved thermal profiles that are much hotter, at roughly 2σ, than the grid models. Though possibly physical in origin,

it is more likely owed to the different physical and chemical assumptions in each model. Longer wavelength information, namely beyond 2.5 microns where most of the flux is, would significantly help in testing if this is the true cause of the discrepancy.

2. In addition to the thermal profiles, the highlight of this work is the retrieval of abundance constraints for the major atmospheric molecular species [H_2O, CH_4, NH_3, K] with a precision of roughly 0.25dex at 1σ (Figure 4.4, Table 4.4). For a majority of our sample, we find that H_2O, CH_4, and NH_3 are consistent with expectations from equilibrium chemistry. There are however, a small subset of objects which do not fit these trends. There are four objects with elevated CH_4 and roughly ten with elevated NH_3 constraints. Though it may be a simple result of small number sampling, there is literature showing that objects near this temperature range may begin to show signs of elevated CH_4 and NH_3 due to non-equilibrium vertical mixing. Developing a larger sample of earlier T dwarfs (T_{eff}>900K) requires accurately taking into consideration a realistic cloud model into our retrieval framework, but would show if this trend continues into higher temperatures. Finally we note that our sample helps confirm previous findings that the depletion of Na and K near 500-600K owed to the chemical rainout of species like enstatite and forsterite is present.

3. Using the retrieved molecular abundances we are able to infer the atmospheric metallicity and C/O ratio. We find that the distribution of our 50 targets is broadly consistent with measurements of the local stellar FGK population. Though there is substantial scatter, there also is a slight positive correlation between atmospheric metallicity and effective temperature.

4. We compare our constraints on both $T_{eff}$and log(g) to expectations from evo-

lutionary models and previous results of Y dwarfs (Figure 4.6). For a majority of objects, we find them to be consistent with expectations of typical field age brown dwarfs. However we also find several outliers that have unphysically old and young ages. We preformed several tests in which we altered the priors on our retrieval model to "guide" these objects to more physically realistic ages. Despite these efforts, we found that the resulting posteriors were highly non-Gaussian and were clustered near the limit of the new prior ranges. This indicates that there is some as yet undetermined feature in the spectra which favors these anomalous ages. Given that these age estimate are likely incorrect, this result highlights the importance of complimenting such retrieval studies with more traditional grid models.

This uniform atmospheric retrieval analysis of 50 T dwarfs provides a large and unique dataset of retrieved thermal profiles, gravities, and atmospheric abundances which offer insight into the physical and chemical mechanisms at work in their atmospheres. This dataset now can serve as a baseline for comparisons between other stars and planets to place brown dwarfs in a holistic astronomical context.

4.7 Acknowledgements

The retrieval analysis work is supported by the National Science Foundation under Grant No. 1615220. JZ acknowledges funding from a NASA FINESST grant. This research has benefited from the SpeX Prism Spectral Libraries, maintained by Adam Burgasser at, http://pono.ucsd.edu/ adam/browndwarfs/spexprism. The research shown herein acknowledges use of the Hypatia Catalog Database, an online compilation of stellar abundance data as described in Hinkel *et al.* (2014).

Table 4.4: Retrieved Atmospheric Abundances and Derived Parameters

Object	T_{eff}[K]	log(g) [cgs]	R [R_J]	H_2O [VMR]	CH_4 [VMR]	NH_3 [VMR]	K [VMR]	[M/H]	C/O
HD3651B	$715.57^{+24.68}_{-9.65}$	$5.07^{+0.09}_{-0.14}$	$1.17^{+0.10}_{-0.10}$	$-3.33^{+0.08}_{-0.07}$	$-3.21^{+0.07}_{-0.07}$	$-4.54^{+0.07}_{-0.09}$	$-7.02^{+0.07}_{-0.09}$	$-0.04^{+0.08}_{-0.07}$	$0.98^{+0.11}_{-0.11}$
WISE-J0040	$885.44^{+18.84}_{-13.25}$	$4.66^{+0.34}_{-0.34}$	$0.97^{+0.10}_{-0.09}$	$-3.51^{+0.34}_{-0.11}$	$-3.54^{+0.15}_{-0.15}$	$-4.82^{+0.21}_{-0.19}$	$-6.91^{+0.09}_{-0.08}$	$-0.35^{+0.14}_{-0.13}$	$0.70^{+0.11}_{-0.11}$
WISE-J0049	$727.28^{+19.72}_{-9.70}$	$5.18^{+0.20}_{-0.33}$	$0.81^{+0.07}_{-0.07}$	$-3.09^{+0.09}_{-0.12}$	$-2.96^{+0.15}_{-0.10}$	$-4.40^{+0.12}_{-0.19}$	$-6.99^{+0.09}_{-0.10}$	$0.14^{+0.10}_{-0.14}$	$1.01^{+0.12}_{-0.12}$
2MASS-J0050	$945.64^{+5.83}_{-12.09}$	$5.26^{+0.22}_{-0.19}$	$0.75^{+0.05}_{-0.04}$	$-3.19^{+0.10}_{-0.12}$	$-3.07^{+0.11}_{-0.14}$	$-4.49^{+0.12}_{-0.13}$	$-6.37^{+0.08}_{-0.09}$	$0.10^{+0.11}_{-0.12}$	$0.98^{+0.11}_{-0.10}$
WISE-PAJ0123	$872.83^{+3.15}_{-3.97}$	$5.15^{+0.11}_{-0.15}$	$1.02^{+0.07}_{-0.06}$	$-3.51^{+0.07}_{-0.08}$	$-3.48^{+0.07}_{-0.08}$	$-4.59^{+0.06}_{-0.08}$	$-6.78^{+0.06}_{-0.06}$	$-0.31^{+0.09}_{-0.08}$	$0.80^{+0.07}_{-0.06}$
WISE-J0223	$787.96^{+4.11}_{-4.60}$	$5.23^{+0.18}_{-0.33}$	$0.81^{+0.09}_{-0.10}$	$-3.12^{+0.11}_{-0.13}$	$-3.25^{+0.09}_{-0.15}$	$-4.72^{+0.15}_{-0.26}$	$-6.80^{+0.09}_{-0.10}$	$-0.02^{+0.10}_{-0.14}$	$0.54^{+0.08}_{-0.07}$
WISE-J0241	$835.78^{+3.82}_{-4.32}$	$4.90^{+0.19}_{-0.22}$	$1.06^{+0.05}_{-0.05}$	$-3.55^{+0.08}_{-0.08}$	$-3.51^{+0.09}_{-0.10}$	$-4.74^{+0.11}_{-0.12}$	$-6.93^{+0.05}_{-0.04}$	$-0.36^{+0.09}_{-0.09}$	$0.82^{+0.07}_{-0.07}$
PSO-J043	$699.53^{+5.75}_{-6.22}$	$5.22^{+0.14}_{-0.21}$	$0.84^{+0.06}_{-0.06}$	$-3.22^{+0.07}_{-0.09}$	$-3.09^{+0.07}_{-0.10}$	$-4.47^{+0.08}_{-0.14}$	$-6.81^{+0.06}_{-0.07}$	$0.02^{+0.07}_{-0.10}$	$1.00^{+0.10}_{-0.11}$
WISE-J0325	$897.80^{+7.93}_{-3.47}$	$3.54^{+0.13}_{-0.08}$	$0.94^{+0.06}_{-0.05}$	$-3.77^{+0.07}_{-0.07}$	$-4.00^{+0.07}_{-0.06}$	$-5.47^{+0.11}_{-0.12}$	$-6.84^{+0.08}_{-0.08}$	$-0.69^{+0.14}_{-0.07}$	$0.47^{+0.09}_{-0.05}$
2MASS-J0415	$675.24^{+8.95}_{-5.38}$	$5.10^{+0.15}_{-0.25}$	$0.94^{+0.06}_{-0.06}$	$-3.24^{+0.07}_{-0.09}$	$-3.13^{+0.08}_{-0.12}$	$-4.53^{+0.09}_{-0.16}$	$-6.88^{+0.06}_{-0.06}$	$-0.02^{+0.07}_{-0.10}$	$0.96^{+0.09}_{-0.10}$
WISE-PCJ0458	$616.50^{+4.15}_{-9.05}$	$4.87^{+0.25}_{-0.45}$	$1.15^{+0.14}_{-0.13}$	$-3.28^{+0.12}_{-0.19}$	$-3.40^{+0.13}_{-0.21}$	$-4.77^{+0.16}_{-0.23}$	$-7.32^{+0.14}_{-0.18}$	$-0.05^{+0.18}_{-0.21}$	$0.53^{+0.10}_{-0.08}$
UGPS-J0521	$658.43^{+1.21}_{-0.58}$	$5.28^{+0.19}_{-0.27}$	$0.74^{+0.04}_{-0.05}$	$-3.05^{+0.08}_{-0.08}$	$-2.97^{+0.09}_{-0.12}$	$-4.49^{+0.10}_{-0.17}$	$-6.79^{+0.07}_{-0.09}$	$0.24^{+0.09}_{-0.10}$	$0.83^{+0.09}_{-0.08}$
WISE-J0521	$880.60^{+4.15}_{-3.15}$	$4.18^{+0.39}_{-0.28}$	$0.85^{+0.03}_{-0.05}$	$-3.47^{+0.15}_{-0.08}$	$-3.54^{+0.19}_{-0.12}$	$-5.07^{+0.14}_{-0.21}$	$-6.79^{+0.07}_{-0.06}$	$-0.27^{+0.18}_{-0.10}$	$0.63^{+0.09}_{-0.08}$
WISE-J0614	$897.89^{+4.22}_{-14.69}$	$4.93^{+0.12}_{-0.20}$	$1.22^{+0.09}_{-0.09}$	$-3.48^{+0.07}_{-0.07}$	$-3.45^{+0.07}_{-0.09}$	$-4.68^{+0.08}_{-0.11}$	$-6.86^{+0.06}_{-0.05}$	$-0.29^{+0.07}_{-0.08}$	$0.79^{+0.07}_{-0.07}$
2MASS-J0727	$953.07^{+3.34}_{-1.80}$	$5.23^{+0.17}_{-0.20}$	$0.76^{+0.05}_{-0.04}$	$-3.09^{+0.10}_{-0.09}$	$-3.15^{+0.10}_{-0.10}$	$-4.76^{+0.10}_{-0.26}$	$-6.51^{+0.08}_{-0.10}$	$0.05^{+0.10}_{-0.10}$	$0.65^{+0.07}_{-0.06}$
2MASS-J0729	$719.36^{+6.39}_{-5.10}$	$5.28^{+0.15}_{-0.23}$	$0.82^{+0.10}_{-0.09}$	$-3.24^{+0.09}_{-0.10}$	$-3.37^{+0.09}_{-0.11}$	$-4.55^{+0.10}_{-0.15}$	$-6.89^{+0.09}_{-0.09}$	$0.01^{+0.15}_{-0.13}$	$0.52^{+0.05}_{-0.07}$
2MASS-J0939	$631.72^{+5.13}_{-6.67}$	$4.85^{+0.29}_{-0.33}$	$1.01^{+0.06}_{-0.06}$	$-3.44^{+0.12}_{-0.13}$	$-3.49^{+0.14}_{-0.16}$	$-4.68^{+0.15}_{-0.17}$	$-7.32^{+0.13}_{-0.11}$	$-0.29^{+0.13}_{-0.15}$	$0.67^{+0.07}_{-0.07}$

Table 4.4: Retrieved Atmospheric Abundances and Derived Parameters

Object	T_{eff}[K]	log(g) [cgs]	R [R_J]	H_2O [VMR]	CH_4 [VMR]	NH_3 [VMR]	K [VMR]	[M/H]	C/O
ULAS-J1029	$690.39^{+6.46}_{-3.34}$	$4.99^{+0.19}_{-0.27}$	$1.04^{+0.09}_{-0.09}$	$-3.33^{+0.09}_{-0.11}$	$-3.08^{+0.10}_{-0.13}$	$-4.44^{+0.10}_{-0.15}$	$-7.27^{+0.12}_{-0.16}$	$-0.01^{+0.11}_{-0.12}$	$1.28^{+0.18}_{-0.19}$
WISE-J1039	$745.93^{+24.79}_{-9.72}$	$4.58^{+0.29}_{-0.48}$	$1.46^{+0.26}_{-0.23}$	$-3.62^{+0.18}_{-0.20}$	$-3.45^{+0.17}_{-0.23}$	$-4.79^{+0.17}_{-0.24}$	$-7.01^{+0.18}_{-0.17}$	$-0.33^{+0.19}_{-0.22}$	$1.03^{+0.28}_{-0.21}$
WISE-J105257	$768.40^{+13.94}_{-9.22}$	$4.36^{+0.40}_{-0.38}$	$1.04^{+0.07}_{-0.07}$	$-3.61^{+0.13}_{-0.12}$	$-3.59^{+0.18}_{-0.17}$	$-4.89^{+0.21}_{-0.20}$	$-7.09^{+0.06}_{-0.06}$	$-0.43^{+0.16}_{-0.15}$	$0.77^{+0.13}_{-0.12}$
2MASS-J1114	$617.46^{+5.43}_{-2.78}$	$4.97^{+0.22}_{-0.40}$	$1.01^{+0.11}_{-0.11}$	$-3.34^{+0.11}_{-0.15}$	$-3.51^{+0.11}_{-0.19}$	$-4.70^{+0.14}_{-0.24}$	$-7.16^{+0.11}_{-0.15}$	$-0.24^{+0.12}_{-0.17}$	$0.50^{+0.08}_{-0.08}$
2MASS-J1217	$775.64^{+27.09}_{-12.75}$	$4.82^{+0.17}_{-0.28}$	$1.30^{+0.12}_{-0.12}$	$-3.42^{+0.09}_{-0.10}$	$-3.26^{+0.09}_{-0.12}$	$-4.59^{+0.10}_{-0.15}$	$-6.83^{+0.09}_{-0.07}$	$-0.16^{+0.10}_{-0.10}$	$1.03^{+0.15}_{-0.15}$
WISE-J1124	$848.44^{+26.25}_{-9.67}$	$4.78^{+0.23}_{-0.26}$	$0.99^{+0.10}_{-0.07}$	$-3.41^{+0.10}_{-0.11}$	$-3.45^{+0.11}_{-0.12}$	$-4.68^{+0.15}_{-0.15}$	$-6.75^{+0.09}_{-0.10}$	$-0.25^{+0.12}_{-0.11}$	$0.83^{+0.07}_{-0.08}$
WISE-J1254	$875.62^{+6.77}_{-23.90}$	$3.81^{+0.46}_{-0.28}$	$0.95^{+0.26}_{-0.13}$	$-3.80^{+0.19}_{-0.19}$	$-4.02^{+0.21}_{-0.16}$	$-5.36^{+0.28}_{-0.46}$	$-6.66^{+0.17}_{-0.18}$	$-0.75^{+0.19}_{-0.18}$	$0.41^{+0.19}_{-0.11}$
WISE-J1257	$758.90^{+6.54}_{-4.72}$	$3.77^{+0.51}_{-0.21}$	$0.89^{+0.18}_{-0.09}$	$-3.75^{+0.14}_{-0.14}$	$-3.96^{+0.23}_{-0.13}$	$-5.75^{+0.46}_{-1.32}$	$-6.62^{+0.15}_{-0.17}$	$-0.67^{+0.19}_{-0.13}$	$0.48^{+0.19}_{-0.09}$
ROSS458C	$762.64^{+6.85}_{-1.81}$	$3.74^{+0.33}_{-0.17}$	$0.87^{+0.09}_{-0.05}$	$-3.27^{+0.11}_{-0.10}$	$-3.46^{+0.16}_{-0.09}$	$-5.31^{+0.22}_{-0.21}$	$-6.56^{+0.13}_{-0.22}$	$-0.20^{+0.14}_{-0.09}$	$0.51^{+0.12}_{-0.07}$
WISE-J1322	$775.78^{+6.91}_{-19.53}$	$3.87^{+0.77}_{-0.48}$	$1.17^{+0.33}_{-0.22}$	$-3.73^{+0.27}_{-0.23}$	$-3.83^{+0.36}_{-0.25}$	$-5.38^{+0.44}_{-0.52}$	$-6.94^{+0.17}_{-0.17}$	$-0.59^{+0.32}_{-0.23}$	$0.62^{+0.27}_{-0.18}$
ULAS-J1416	$616.23^{+1.90}_{-4.07}$	$5.12^{+0.19}_{-0.46}$	$0.93^{+0.07}_{-0.06}$	$-3.47^{+0.09}_{-0.19}$	$-3.69^{+0.09}_{-0.21}$	$-4.76^{+0.11}_{-0.23}$	$-7.23^{+0.10}_{-0.21}$	$-0.38^{+0.09}_{-0.19}$	$0.45^{+0.07}_{-0.06}$
WISE-J1457	$768.75^{+5.59}_{-10.00}$	$4.67^{+0.23}_{-0.39}$	$1.38^{+0.22}_{-0.19}$	$-3.65^{+0.12}_{-0.14}$	$-3.59^{+0.12}_{-0.18}$	$-4.80^{+0.13}_{-0.24}$	$-6.99^{+0.10}_{-0.09}$	$-0.44^{+0.12}_{-0.16}$	$0.83^{+0.15}_{-0.15}$
Gliese 570D	$789.90\ ^{+4.05}_{-12.67}$	$5.14^{+0.14}_{-0.26}$	$0.95^{+0.09}_{-0.11}$	$-3.27^{+0.09}_{-0.09}$	$-3.25^{+0.08}_{-0.12}$	$-4.58^{+0.10}_{-0.21}$	$-6.81^{+0.08}_{-0.07}$	$-0.02^{+0.10}_{-0.10}$	$0.77^{+0.08}_{-0.10}$
PSO-J224	$892.88^{+8.55}_{-25.81}$	$3.64^{+0.25}_{-0.14}$	$0.91^{+0.07}_{-0.06}$	$-3.86^{+0.09}_{-0.09}$	$-3.92^{+0.12}_{-0.08}$	$-5.25^{+0.13}_{-0.11}$	$-6.89^{+0.08}_{-0.08}$	$-0.62^{+0.16}_{-0.10}$	$0.68^{+0.09}_{-0.08}$
SDSS-1504	$872.47^{+5.04}_{-9.67}$	$4.98^{+0.12}_{-0.20}$	$1.22^{+0.08}_{-0.07}$	$-3.55^{+0.06}_{-0.08}$	$-3.45^{+0.06}_{-0.10}$	$-4.63^{+0.07}_{-0.11}$	$-6.93^{+0.05}_{-0.05}$	$-0.32^{+0.07}_{-0.09}$	$0.91^{+0.08}_{-0.08}$
2MASS-J1553	$900.88^{+2.03}_{-1.83}$	$4.56^{+0.20}_{-0.20}$	$1.13^{+0.06}_{-0.06}$	$-3.38^{+0.08}_{-0.08}$	$-3.49^{+0.09}_{-0.09}$	$-5.06^{+0.13}_{-0.21}$	$-6.60^{+0.06}_{-0.14}$	$-0.27^{+0.09}_{-0.09}$	$0.58^{+0.05}_{-0.06}$
SDSS-J16283	$916.45^{+6.58}_{-10.41}$	$4.91^{+0.31}_{-0.40}$	$0.83^{+0.07}_{-0.06}$	$-3.29^{+0.12}_{-0.13}$	$-3.28^{+0.15}_{-0.18}$	$-4.76^{+0.20}_{-0.22}$	$-6.58^{+0.09}_{-0.09}$	$-0.11^{+0.14}_{-0.16}$	$0.73^{+0.13}_{-0.10}$

Table 4.4: Retrieved Atmospheric Abundances and Derived Parameters

Object	T_{eff}[K]	log(g) [cgs]	R [R_J]	H_2O [VMR]	CH_4 [VMR]	NH_3 [VMR]	K [VMR]	[M/H]	C/O
WISE-J1653	$687.22^{+15.06}_{-12.25}$	$4.87^{+0.28}_{-0.44}$	$1.03^{+0.12}_{-0.13}$	$-3.27^{+0.13}_{-0.16}$	$-3.30^{+0.13}_{-0.21}$	$-4.77^{+0.19}_{-0.29}$	$-7.01^{+0.11}_{-0.10}$	$-0.11^{+0.14}_{-0.19}$	$0.66^{+0.12}_{-0.11}$
WISE-PAJ1711	$805.55^{+2.76}_{-1.80}$	$4.80^{+0.27}_{-0.43}$	$1.17^{+0.23}_{-0.15}$	$-3.45^{+0.14}_{-0.18}$	$-3.40^{+0.14}_{-0.21}$	$-4.74^{+0.14}_{-0.24}$	$-7.05^{+0.11}_{-0.12}$	$-0.24^{+0.14}_{-0.19}$	$0.82^{+0.15}_{-0.14}$
WISE-PAJ1741	$646.58^{+4.26}_{-4.58}$	$4.64^{+0.18}_{-0.18}$	$0.84^{+0.03}_{-0.04}$	$-3.29^{+0.08}_{-0.06}$	$-3.19^{+0.09}_{-0.08}$	$-4.62^{+0.09}_{-0.10}$	$-7.33^{+0.09}_{-0.09}$	$-0.08^{+0.08}_{-0.07}$	$0.95^{+0.07}_{-0.08}$
WISE-J1813	$706.42^{+4.04}_{-4.45}$	$4.51^{+0.13}_{-0.20}$	$2.04^{+0.19}_{-0.35}$	$-3.45^{+0.11}_{-0.08}$	$-3.29^{+0.07}_{-0.10}$	$-4.76^{+0.09}_{-0.27}$	$-7.23^{+0.13}_{-0.11}$	$-0.19^{+0.09}_{-0.08}$	$1.02^{+0.14}_{-0.23}$
WISEPA J1852	$915.71^{+14.64}_{-5.53}$	$5.12^{+0.22}_{-0.28}$	$0.80^{+0.10}_{-0.05}$	$-3.16^{+0.12}_{-0.15}$	$-3.06^{+0.13}_{-0.15}$	$-4.62^{+0.14}_{-0.20}$	$-6.38^{+0.09}_{-0.13}$	$0.06^{+0.13}_{-0.16}$	$0.93^{+0.16}_{-0.12}$
WISE-PAJ1959	$754.21^{+17.80}_{-6.23}$	$3.74^{+0.32}_{-0.18}$	$0.91^{+0.07}_{-0.06}$	$-3.64^{+0.08}_{-0.07}$	$-3.76^{+0.07}_{-0.13}$	$-5.16^{+0.15}_{-0.10}$	$-7.00^{+0.09}_{-0.09}$	$-0.53^{+0.11}_{-0.08}$	$0.58^{+0.11}_{-0.07}$
WISE-J2000	$753.40^{+3.29}_{-5.34}$	$4.76^{+0.39}_{-0.27}$	$0.90^{+0.06}_{-0.05}$	$-3.31^{+0.12}_{-0.10}$	$-3.34^{+0.17}_{-0.13}$	$-4.80^{+0.21}_{-0.17}$	$-7.05^{+0.07}_{-0.06}$	$-0.17^{+0.15}_{-0.11}$	$0.70^{+0.09}_{-0.08}$
WISE-PCJ2157	$792.95^{+12.10}_{-9.11}$	$5.22^{+0.15}_{-0.25}$	$0.83^{+0.05}_{-0.05}$	$-3.27^{+0.07}_{-0.08}$	$-3.22^{+0.07}_{-0.12}$	$-4.57^{+0.10}_{-0.15}$	$-6.89^{+0.06}_{-0.06}$	$-0.02^{+0.07}_{-0.10}$	$0.85^{+0.06}_{-0.07}$
WISE-PCJ2209	$809.34^{+5.18}_{-4.03}$	$5.00^{+0.21}_{-0.30}$	$0.90^{+0.05}_{-0.04}$	$-3.37^{+0.08}_{-0.12}$	$-3.54^{+0.10}_{-0.14}$	$-4.79^{+0.13}_{-0.19}$	$-6.95^{+0.06}_{-0.06}$	$-0.28^{+0.10}_{-0.13}$	$0.50^{+0.05}_{-0.05}$
WISE-J2213	$852.44^{+11.78}_{-11.13}$	$4.65^{+0.33}_{-0.28}$	$0.96^{+0.09}_{-0.06}$	$-3.50^{+0.10}_{-0.09}$	$-3.57^{+0.14}_{-0.13}$	$-4.86^{+0.20}_{-0.16}$	$-6.73^{+0.07}_{-0.08}$	$-0.36^{+0.12}_{-0.11}$	$0.63^{+0.12}_{-0.08}$
WISE-J2226	$868.13^{+18.55}_{-13.44}$	$5.27^{+0.18}_{-0.27}$	$0.78^{+0.09}_{-0.06}$	$-3.02^{+0.11}_{-0.15}$	$-2.98^{+0.11}_{-0.14}$	$-4.85^{+0.24}_{-0.37}$	$-6.48^{+0.09}_{-0.14}$	$0.16^{+0.11}_{-0.14}$	$0.82^{+0.14}_{-0.10}$
WISE-J2255	$720.23^{+3.48}_{-7.03}$	$5.22^{+0.15}_{-0.23}$	$0.89^{+0.11}_{-0.10}$	$-3.09^{+0.12}_{-0.11}$	$-2.94^{+0.10}_{-0.11}$	$-4.51^{+0.11}_{-0.18}$	$-6.90^{+0.13}_{-0.12}$	$0.16^{+0.11}_{-0.11}$	$1.04^{+0.17}_{-0.15}$
WISE-J2319	$714.16^{+5.82}_{-2.84}$	$4.87^{+0.59}_{-0.64}$	$0.62^{+0.09}_{-0.07}$	$-3.44^{+0.25}_{-0.25}$	$-3.43^{+0.28}_{-0.30}$	$-4.61^{+0.29}_{-0.32}$	$-6.99^{+0.16}_{-0.15}$	$-0.24^{+0.26}_{-0.28}$	$0.74^{+0.15}_{-0.13}$
ULAS-J2321	$750.05^{+8.29}_{-8.48}$	$5.23^{+0.11}_{-0.17}$	$0.90^{+0.06}_{-0.07}$	$-3.14^{+0.07}_{-0.07}$	$-2.96^{+0.07}_{-0.08}$	$-4.36^{+0.07}_{-0.11}$	$-6.74^{+0.07}_{-0.07}$	$0.13^{+0.07}_{-0.08}$	$1.12^{+0.11}_{-0.11}$
WISE-J2340	$904.21^{+5.96}_{-5.98}$	$4.72^{+0.17}_{-0.23}$	$1.47^{+0.14}_{-0.11}$	$-3.58^{+0.09}_{-0.10}$	$-3.56^{+0.09}_{-0.11}$	$-4.87^{+0.10}_{-0.15}$	$-6.73^{+0.08}_{-0.08}$	$-0.40^{+0.10}_{-0.11}$	$0.78^{+0.09}_{-0.08}$
WISE-J2348	$921.60^{+1.08}_{-9.23}$	$4.94^{+0.29}_{-0.32}$	$0.77^{+0.20}_{-0.07}$	$-3.28^{+0.17}_{-0.17}$	$-3.20^{+0.17}_{-0.15}$	$-4.74^{+0.19}_{-0.22}$	$-6.51^{+0.15}_{-0.27}$	$-0.07^{+0.17}_{-0.16}$	$0.87^{+0.23}_{-0.13}$

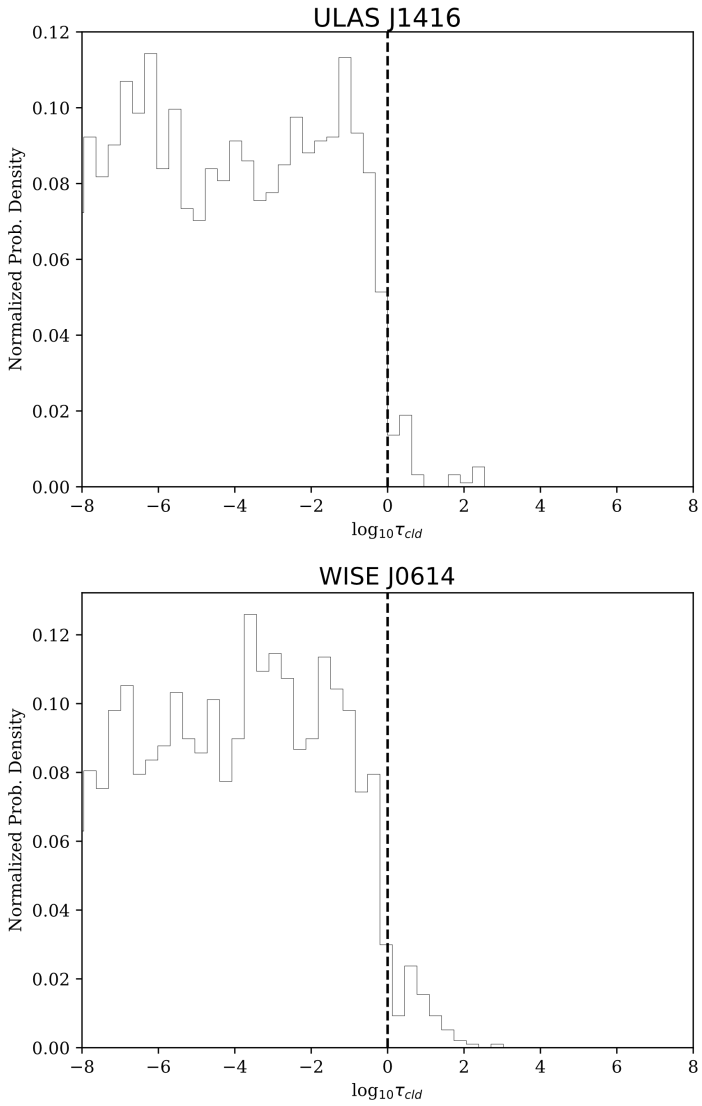

Figure 4.9: Cloud column optical depth (τ_{cld}) posteriors for two different representative targets of our 50 target sample. The optical depth is calculated by integrating the retrieved opacity profile. The central dashed line indicates where τ_{cld}=1. The histograms sharply decline as we approach this value, suggesting that the data are not affected by optically thick clouds. Profiles for all 50 objects are available in the online version of this work.

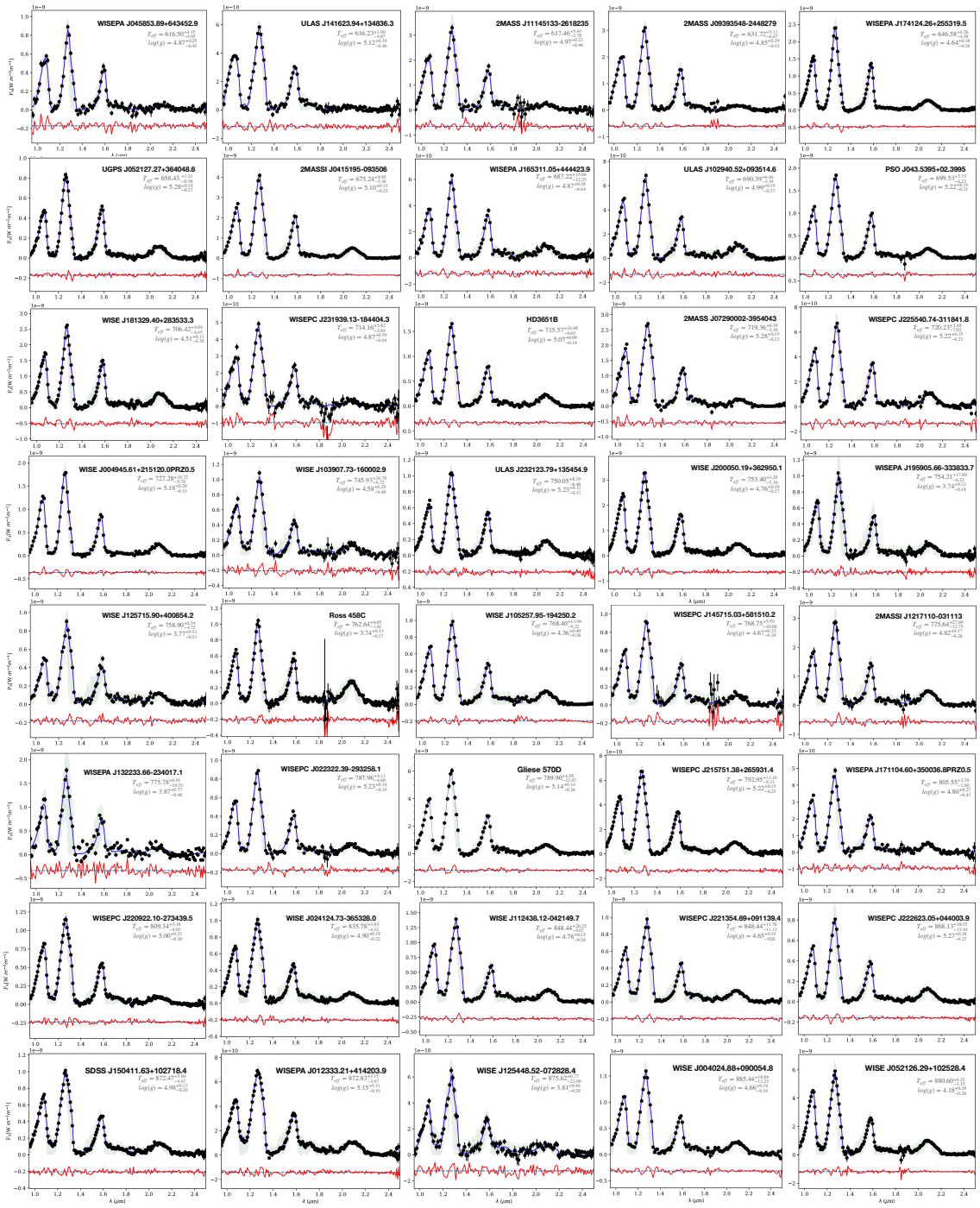
WISEPA J045853.89+643452.9
ULAS J141623.94+134836.3
2MASS J11145133-2618235
2MASS J09393548-2448279
WISEPA J174124.26+255319.5
UGPS J052127.27+364048.6
2MASSI J0415195-093506
WISEPA J165311.05+444423.9
ULAS J102940.52+093514.6
PSO J043.5395+02.3995
WISE J181329.40+283533.3
WISEPC J231939.13-184404.3
HD3651B
2MASS J07290002-3954043
WISEPC J225540.74-311841.8
WISE J004945.61+215120.0PRZ0.5
WISE J103907.73-160002.9
ULAS J232123.79+135454.9
WISE J200050.19+362950.1
WISEPA J195905.66-333833.7
WISE J125715.90+400854.2
Ross 458C
WISE J105257.95-194250.2
WISEPC J145715.03+581510.2
2MASSI J1217110-031113
WISEPA J132233.66-234017.1
WISEPC J022322.39-293258.1
Gliese 570D
WISEPC J215751.38+265931.4
WISEPA J171104.60+350036.8PRZ0.5
WISEPC J220922.10-273439.5
WISE J024124.73-365328.0
WISE J112438.12-042149.7
WISEPC J221354.69+091139.4
WISEPC J222623.05+044003.9
SDSS J150411.63+102718.4
WISEPA J012333.21+414203.9
WISE J125448.52-072828.4
WISE J004024.88+090054.8
WISE J052126.29+102528.4
λ (μm)
F_λ (W m⁻² m⁻¹)

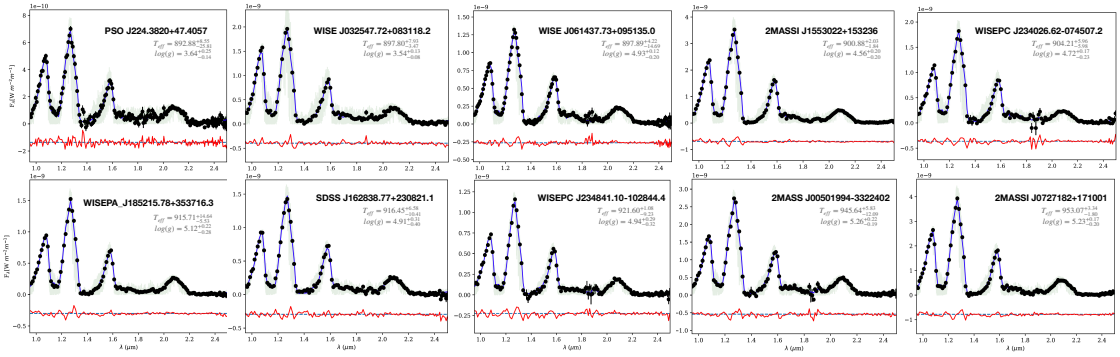

Figure 4.10: A continuation of Figure 4.2 showing the SpeX spectra (black), best-fit spectra (blue) and residuals (red) for all objects in our sample.

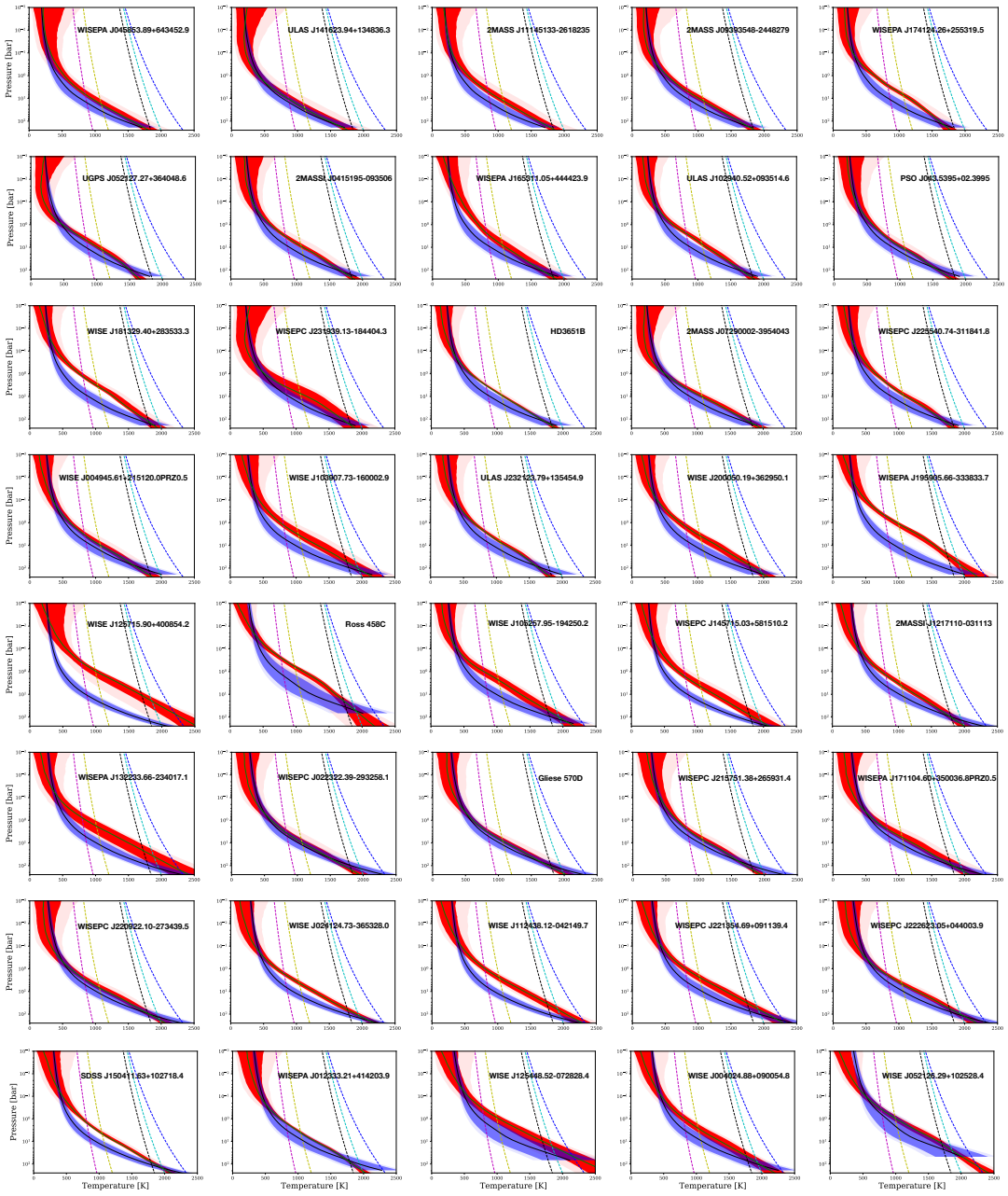
WISEPA J045853.89+643452.9
ULAS J141623.94+134836.3
2MASS J11145133-2618235
2MASS J09393548-2448279
WISEPA J174124.26+255319.5
UGPS J052127.27+364048.6
2MASSI J0415195-093506
WISEPA J165071.05+444423.9
ULAS J102940.52+093514.6
PSO J093.5395+02.3995
WISE J181329.40+283533.3
WISEPC J231939.13-184404.3
HD3651B
2MASS J07290002-3954043
WISEPC J225540.74-311841.8
WISE J004945.61+215120.0PRZ0.5
WISE J103907.73-160002.9
ULAS J232123.79+135454.9
WISE J200050.19+362950.1
WISEPA J195905.66-333833.7
WISE J125715.90+400854.2
Ross 458C
WISE J105257.95-194250.2
WISEPC J145715.03+581510.2
2MASSI J1217110-031113
WISEPA J132223.66-234017.1
WISEPC J022322.39-293258.1
Gliese 570D
WISEPC J213751.38+265931.4
WISEPA J171104.60+350036.8PRZ0.5
WISEPC J220922.10-273439.5
WISE J024124.73-365328.0
WISE J112438.12-042149.7
WISEPC J221354.69+091139.4
WISEPC J222623.05+044003.9
SDSS J150411.63+102718.4
WISEPA J012333.21+414203.9
WISE J123448.52-072828.4
WISE J004024.88+090054.8
WISE J052126.29+102528.4
Pressure [bar]
Temperature [K]

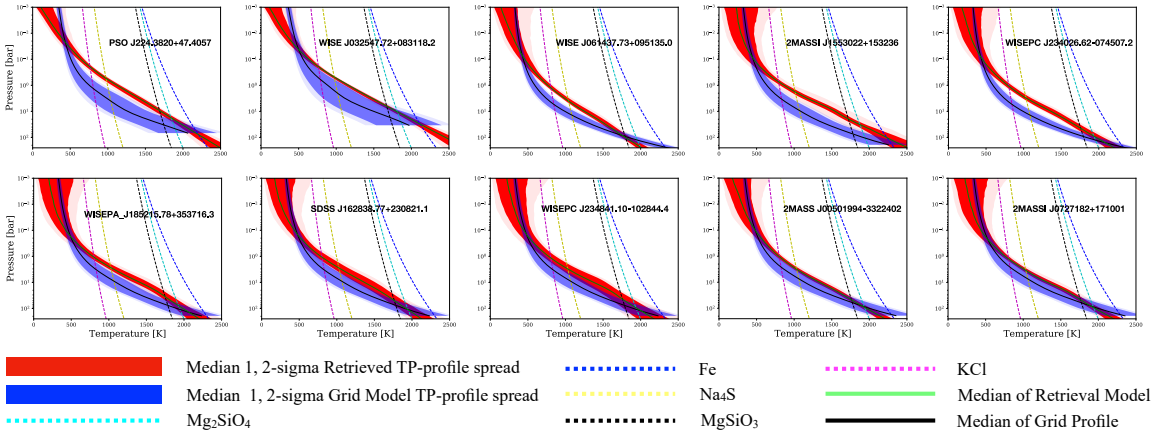

Figure 4.11: A continuation of Figure 4.3 showing the retrieved (red) and grid-model (blue) PT profiles, overlaid with relevant condensate curves, for all objects in our sample.

Chapter 5

CONCLUSION & FUTURE DIRECTIONS

This thesis presents both a uniform atmospheric retrieval analysis of ultra-cool brown dwarfs, and a technical discussion on how atmospheric retrieval can be improved with graphical processing units. Future efforts to combine these techniques will be fundamental to developing a better understanding of brown dwarf atmospheres, and their place in the continuity between stellar and planetary objects.

Chapter 2 details a study of 11 ultra-cool Y dwarfs, provides a foundational dataset of constraints on their physical and chemical atmospheric properties, and compares such results with both other modeling methods and expectations from current and future JWST observations. Chapter 3 establishes a computational tool that allows retrievals to not only perform faster, but opens up the possibility of population-level atmospheric retrieval studies of substellar atmospheres. Chapter 4 leverages this tool to study 50 different late-T dwarfs, and further the foundational dataset begun in Chapter 2.

There are several avenues of exploration which form a natural continuation from the work presented here. The first, and most obvious extension is to continue using the same atmospheric retrieval analysis into the hotter early-T and L dwarf classes. These objects have been historically difficult to characterize due to the presence of iron-silicate condensate cloud species in their photospheres (e.g. Marley and Robinson, 2015). Several improvements to address this problem have been made to CHIMERA including modifying the radiative transfer to account for multiple scattering in the atmosphere to enable an implementation of the Ackerman and Marley (2001) cloud model, and the addition of several other TP profile parameterizations from the liter-

ature (e.g. Madhusudhan and Seager, 2009). Though such work has yet to be carried out, the SpeX database offers an abundance of ideal early-T and L dwarf spectra to carry out an analysis similar to Chapter 4 on the hotter spectral classes.

Continuing to focus on the L dwarf class, another project could be to apply CHIMERA to the extreme subset of unusually red L-dwarfs. Though red J-K colors are typically an indicator of youth, a small subset of objects have evidence that they are much older, requiring an atmospheric explanation for their colors and spectra. In addition, these objects often overlap planetary-mass objects in several color-mag and color-color spaces making them ideal targets to characterize for comparison with the observed exoplanet population. Recent literature has found success in using atmospheric retrieval to fit the entire spectrum of a single red L dwarf (Burningham *et al.*, 2021). As the these red L Dwarfs have been observed more readily in the literature compared to other objects, there is a wealth of publicly available spectra and photometry that has yet to be analyzed with GPU-accelerated atmospheric retrieval.

Another avenue of work could involve retrieval studies of brown dwarfs in young ($\lesssim$100Myr) moving groups. Moving groups provide two key constraints of having both a well-defined age, and such objects should have similar bulk metallicities as they formed in the same environment. These two constraints can strongly anchor atmospheric models and provide valuable laboratories for improvements in cloud prescriptions, non-equilibrium chemistry, or other novel ideas. There are dozens of young moving group brown dwarfs spanning the full range of L and T dwarfs. Since such an analysis would require a population-level study, this area of research is also ripe for exploration with the GPU-accelerated version of CHIMERA.

A final project could involve using retrievals to look at the coolest brown dwarf known, WISE-0855. This object is part of an approved JWST Cycle 1 GO program which will obtain high quality spectra which may prove diagnostic on both the pres-

ence of water ice clouds thought to be present in the coolest brown dwarfs (Morley *et al.*, 2014), and any variability associated with these clouds. Using a mix of complementary grid-based and retrieval models to holistically understand the full spectrum of this object would provide a strong anchor in a temperature regime which straddles the coolest brown dwarf and exoplanet population.

With these future prospects, amplified with the wealth of future JWST observations on the horizon, I hope this thesis has provided a small, but focused, flicker of light in what are often the hazy, cloudy, and dim atmospheres of brown dwarfs.

Ackerman, A. S. and M. S. Marley, "Precipitating Condensation Clouds in Substellar Atmospheres", ApJ, **556**, 872–884 (2001).

Allard, F., P. H. Hauschildt, I. Baraffe and G. Chabrier, "Synthetic Spectra and Mass Determination of the Brown Dwarf GI 229B", ApJL, **465**, L123 (1996).

Allard, F., D. Homeier and B. Freytag, "Models of very-low-mass stars, brown dwarfs and exoplanets", Philosophical Transactions of the Royal Society of London Series A **370**, 2765–2777 (2012).

Allard, N. F., F. Spiegelman and J. F. Kielkopf, "K-H_2 line shapes for the spectra of cool brown dwarfs", A&A, **589**, A21 (2016).

Amundsen, D. S., P. Tremblin, J. Manners, I. Baraffe and N. J. Mayne, "Treatment of overlapping gaseous absorption with the correlated-k method in hot Jupiter and brown dwarf atmosphere models", A&A, **598**, A97 (2017).

Arcangeli, J., J.-M. Désert, M. R. Line, J. L. Bean, V. Parmentier, K. B. Stevenson, L. Kreidberg, J. J. Fortney, M. Mansfield and A. P. Showman, "H^- Opacity and Water Dissociation in the Dayside Atmosphere of the Very Hot Gas Giant WASP-18b", ApJL, **855**, 2, L30 (2018).

Baraffe, I., G. Chabrier, T. S. Barman, F. Allard and P. H. Hauschildt, "Evolutionary models for cool brown dwarfs and extrasolar giant planets. The case of HD 209458", A&A, **402**, 701–712 (2003).

Bate, M. R., I. A. Bonnell and V. Bromm, "The formation mechanism of brown dwarfs", MNRAS, **332**, 3, L65–L68 (2002).

Bate, M. R., I. A. Bonnell and V. Bromm, "The formation of a star cluster: predicting the properties of stars and brown dwarfs", MNRAS, **339**, 577–599 (2003).

Baudino, J.-L., P. Mollière, O. Venot, P. Tremblin, B. Bézard and P.-O. Lagage, "Toward the Analysis of JWST Exoplanet Spectra: Identifying Troublesome Model Parameters", ApJ, **850**, 150 (2017).

Bean, J. L., C. Sneden, P. H. Hauschildt, C. M. Johns-Krull and G. F. Benedict, "Accurate M Dwarf Metallicities from Spectral Synthesis: A Critical Test of Model Atmospheres", ApJ, **652**, 1604–1616 (2006).

Beatty, T. G., I. Wong, T. Fetherolf, M. R. Line, A. Shporer, K. G. Stassun, G. R. Ricker, S. Seager, J. N. Winn, J. M. Jenkins, D. R. Louie, J. E. Schlieder, L. Sha, P. Tenenbaum and D. A. Yahalomi, "The TESS Phase Curve of KELT-1b Suggests a High Dayside Albedo", arXiv e-prints p. arXiv:2006.10292 (2020).

Becklin, E. E. and B. Zuckerman, "A low-temperature companion to a white dwarf star", Nature, **336**, 656–658 (1988).

Beichman, C., C. R. Gelino, J. D. Kirkpatrick, M. C. Cushing, S. Dodson-Robinson, M. S. Marley, C. V. Morley and E. L. Wright, "WISE Y Dwarfs as Probes of the Brown Dwarf-Exoplanet Connection", ApJ, **783**, 68 (2014).

Belleman, R. G., J. Bédorf and S. F. Portegies Zwart, "High performance direct gravitational n-body simulations on graphics processing units ii: An implementation in cuda", New Astronomy **13**, 2, 103–112, URL https://www.sciencedirect.com/science/article/pii/S1384107607000760 (2008).

Benneke, B. and S. Seager, "Atmospheric Retrieval for Super-Earths: Uniquely Constraining the Atmospheric Composition with Transmission Spectroscopy", ApJ, **753**, 100 (2012).

Best, W. M. J., M. C. Liu, E. A. Magnier and T. J. Dupuy, "The Hawaii Infrared Parallax Program. IV. A Comprehensive Parallax Survey of L0-T8 Dwarfs with UKIRT", AJ, **159**, 6, 257 (2020).

Best, W. M. J., E. A. Magnier, M. C. Liu, K. M. Aller, Z. Zhang, W. S. Burgett, K. C. Chambers, P. Draper, H. Flewelling, N. Kaiser, R. P. Kudritzki, N. Metcalfe, J. L. Tonry, R. J. Wainscoat and C. Waters, "Photometry and Proper Motions of M, L, and T Dwarfs from the Pan-STARRS1 3π Survey", ApJS, **234**, 1, 1 (2018).

Bonnefoy, M., K. Perraut, A. M. Lagrange, P. Delorme, A. Vigan, M. Line, L. Rodet, C. Ginski, D. Mourard, G. D. Marleau, M. Samland, P. Tremblin, R. Ligi, F. Cantalloube, P. Mollière, B. Charnay, M. Kuzuhara, M. Janson, C. Morley, D. Homeier, V. D'Orazi, H. Klahr, C. Mordasini, B. Lavie, J. L. Baudino, H. Beust, S. Peretti, A. Musso Bartucci, D. Mesa, B. Bézard, A. Boccaletti, R. Galicher, J. Hagelberg, S. Desidera, B. Biller, A. L. Maire, F. Allard, S. Borgniet, J. Lannier, N. Meunier, M. Desort, E. Alecian, G. Chauvin, M. Langlois, T. Henning, L. Mugnier, D. Mouillet, R. Gratton, T. Brandt, M. Mc Elwain, J. L. Beuzit, M. Tamura, Y. Hori, W. Brandner, E. Buenzli, A. Cheetham, M. Cudel, M. Feldt, M. Kasper, M. Keppler, T. Kopytova, M. Meyer, C. Perrot, D. Rouan, G. Salter, T. Schmidt, E. Sissa, A. Zurlo, F. Wildi, P. Blanchard, V. De Caprio, A. Delboulbé, D. Maurel, T. Moulin, A. Pavlov, P. Rabou, J. Ramos, R. Roelfsema, G. Rousset, E. Stadler, F. Rigal and L. Weber, "The GJ 504 system revisited. Combining interferometric, radial velocity, and high contrast imaging data", A&A, **618**, A63 (2018).

Boss, A. P., "Formation of Planetary-Mass Objects by Protostellar Collapse and Fragmentation", ApJ, **551**, L167–L170 (2001).

Buck, I., "Gpu computing with nvidia cuda", in "ACM SIGGRAPH 2007 Courses", SIGGRAPH '07, p. 6–es (Association for Computing Machinery, New York, NY, USA, 2007), URL https://doi.org/10.1145/1281500.1281647.

Burgasser, A. J., "The SpeX Prism Library: 1000+ low-resolution, near-infrared spectra of ultracool M, L, T and Y dwarfs", in "Astronomical Society of India Conference Series", vol. 11 of *Astronomical Society of India Conference Series* (2014).

Burgasser, A. J., T. R. Geballe, S. K. Leggett, J. D. Kirkpatrick and D. A. Golimowski, "A Unified Near-Infrared Spectral Classification Scheme for T Dwarfs", ApJ, **637**, 1067–1093 (2006a).

Burgasser, A. J., J. D. Kirkpatrick, K. L. Cruz, I. N. Reid, S. K. Leggett, J. Liebert, A. Burrows and M. E. Brown, "Hubble Space Telescope NICMOS Observations of T Dwarfs: Brown Dwarf Multiplicity and New Probes of the L/T Transition", ApJS, **166**, 2, 585–612 (2006b).

Burgasser, A. J., R. A. Simcoe, J. J. Bochanski, D. Saumon, E. E. Mamajek, M. C. Cushing, M. S. Marley, C. McMurtry, J. L. Pipher and W. J. Forrest, "Clouds in the Coldest Brown Dwarfs: Fire Spectroscopy of Ross 458C", ApJ, **725**, 2, 1405–1420 (2010).

Burgasser, A. J., C. G. Tinney, M. C. Cushing, D. Saumon, M. S. Marley, C. S. Bennett and J. D. Kirkpatrick, "2MASS J09393548-2448279: The Coldest and Least Luminous Brown Dwarf Binary Known?", ApJL, **689**, 1, L53 (2008).

Burningham, B., J. K. Faherty, E. C. Gonzales, M. S. Marley, C. Visscher, R. Lupu, J. Gaarn, M. Fabienne Bieger, R. Freedman and D. Saumon, "Cloud busting: enstatite and quartz clouds in the atmosphere of 2M2224-0158", MNRAS, **506**, 2, 1944–1961 (2021).

Burningham, B., S. K. Leggett, D. Homeier, D. Saumon, P. W. Lucas, D. J. Pinfield, C. G. Tinney, F. Allard, M. S. Marley, H. R. A. Jones, D. N. Murray, M. Ishii, A. Day-Jones, J. Gomes and Z. H. Zhang, "The properties of the T8.5p dwarf Ross 458C", MNRAS, **414**, 4, 3590–3598 (2011).

Burningham, B., M. S. Marley, M. R. Line, R. Lupu, C. Visscher, C. V. Morley, D. Saumon and R. Freedman, "Retrieval of atmospheric properties of cloudy l dwarfs", Monthly Notices of the Royal Astronomical Society **470**, 1, 1177–1197 (2017).

Burrows, A., W. B. Hubbard, J. I. Lunine and J. Liebert, "The theory of brown dwarfs and extrasolar giant planets", Reviews of Modern Physics **73**, 719–765 (2001).

Burrows, A. and C. M. Sharp, "Chemical Equilibrium Abundances in Brown Dwarf and Extrasolar Giant Planet Atmospheres", ApJ, **512**, 843–863 (1999).

Burrows, A., D. Sudarsky and I. Hubeny, "Theory for the Secondary Eclipse Fluxes, Spectra, Atmospheres, and Light Curves of Transiting Extrasolar Giant Planets", ApJ, **650**, 1140–1149 (2006).

Canty, J. I., P. W. Lucas, S. N. Yurchenko, J. Tennyson, S. K. Leggett, C. G. Tinney, H. R. A. Jones, B. Burningham, D. J. Pinfield and R. L. Smart, "Methane and ammonia in the near-infrared spectra of late-T dwarfs", MNRAS, **450**, 1, 454–480 (2015).

Chabrier, G., I. Baraffe, F. Selsis, T. S. Barman, P. Hennebelle and Y. Alibert, "Gaseous Planets, Protostars, and Young Brown Dwarfs: Birth and Fate", in "Protostars and Planets V", edited by B. Reipurth, D. Jewitt and K. Keil, p. 623 (2007).

Colón, K. D., L. Kreidberg, M. Line, L. Welbanks, N. Madhusudhan, T. Beatty, P. Tamburo, K. B. Stevenson, A. Mandell, J. E. Rodriguez, T. Barclay, E. D. Lopez, K. G. Stassun, D. Angerhausen, J. J. Fortney, D. J. James, J. Pepper, J. P. Ahlers, P. Plavchan, S. Awiphan, C. Kotnik, K. K. McLeod, G. Murawski, H. Chotani, D. LeBrun, W. Matzko, D. Rea, M. Vidaurri, S. Webster, J. K. Williams, L. Sheraden Cox, N. Tan and E. A. Gilbert, "An Unusual Transmission Spectrum for the Sub-Saturn KELT-11b Suggestive of a Sub-Solar Water Abundance", arXiv e-prints p. arXiv:2005.05153 (2020).

Cottaar, M., K. R. Covey, M. R. Meyer, D. L. Nidever, K. G. Stassun, J. B. Foster, J. C. Tan, S. D. Chojnowski, N. da Rio, K. M. Flaherty, P. M. Frinchaboy, M. Skrutskie, S. R. Majewski, J. C. Wilson and G. Zasowski, "IN-SYNC I: Homogeneous Stellar Parameters from High-resolution APOGEE Spectra for Thousands of Pre-main Sequence Stars", ApJ, **794**, 2, 125 (2014).

Cruz, K. L., J. D. Kirkpatrick and A. J. Burgasser, "Young L Dwarfs Identified in the Field: A Preliminary Low-Gravity, Optical Spectral Sequence from L0 to L5", AJ, **137**, 3345–3357 (2009).

Cushing, M. C., K. K. Hardegree-Ullman, J. L. Trucks, C. V. Morley, J. E. Gizis, M. S. Marley, J. J. Fortney, J. D. Kirkpatrick, C. R. Gelino, G. N. Mace and S. J. Carey, "The First Detection of Photometric Variability in a Y Dwarf: WISE J140518.39+553421.3", ApJ, **823**, 152 (2016).

Cushing, M. C., J. D. Kirkpatrick, C. R. Gelino, R. L. Griffith, M. F. Skrutskie, A. Mainzer, K. A. Marsh, C. A. Beichman, A. J. Burgasser, L. A. Prato, R. A. Simcoe, M. S. Marley, D. Saumon, R. S. Freedman, P. R. Eisenhardt and E. L. Wright, "The Discovery of Y Dwarfs using Data from the Wide-field Infrared Survey Explorer (WISE)", ApJ, **743**, 50 (2011).

Cushing, M. C., J. D. Kirkpatrick, C. R. Gelino, G. N. Mace, M. F. Skrutskie and A. Gould, "Three New Cool Brown Dwarfs Discovered with the Wide-field Infrared Survey Explorer (WISE) and an Improved Spectrum of the Y0 Dwarf WISE J041022.71+150248.4", AJ, **147**, 113 (2014).

Cushing, M. C., M. S. Marley, D. Saumon, B. C. Kelly, W. D. Vacca, J. T. Rayner, R. S. Freedman, K. Lodders and T. L. Roellig, "Atmospheric Parameters of Field L and T Dwarfs", ApJ, **678**, 1372–1395 (2008).

Cushing, M. C., J. T. Rayner and W. D. Vacca, "An Infrared Spectroscopic Sequence of M, L, and T Dwarfs", ApJ, **623**, 1115–1140 (2005).

Czekala, I., S. M. Andrews, K. S. Mandel, D. W. Hogg and G. M. Green, "Constructing a Flexible Likelihood Function for Spectroscopic Inference", ApJ, **812**, 2, 128 (2015a).

Czekala, I., S. M. Andrews, K. S. Mandel, D. W. Hogg and G. M. Green, "Starfish: Robust spectroscopic inference tools", (2015b).

Dupuy, T. J. and M. C. Liu, "The Hawaii Infrared Parallax Program. I. Ultracool Binaries and the L/T Transition", ApJS, **201**, 19 (2012).

Dupuy, T. J. and M. C. Liu, "Individual Dynamical Masses of Ultracool Dwarfs", ApJS, **231**, 2, 15 (2017).

Eistrup, C., C. Walsh and E. F. van Dishoeck, "Setting the volatile composition of (exo)planet-building material. Does chemical evolution in disk midplanes matter?", A&A, **595**, A83 (2016).

Faherty, J. K., A. J. Burgasser, F. M. Walter, N. Van der Bliek, M. M. Shara, K. L. Cruz, A. A. West, F. J. Vrba and G. Anglada-Escudé, "The Brown Dwarf Kinematics Project (BDKP). III. Parallaxes for 70 Ultracool Dwarfs", ApJ, **752**, 1, 56 (2012).

Fegley, B., Jr. and K. Lodders, "Chemical models of the deep atmospheres of Jupiter and Saturn", Icarus, **110**, 117–154 (1994).

Fegley, B., Jr. and K. Lodders, "Atmospheric Chemistry of the Brown Dwarf Gliese 229B: Thermochemical Equilibrium Predictions", ApJL, **472**, L37 (1996).

Filippazzo, J. C., E. L. Rice, J. Faherty, K. L. Cruz, M. M. Van Gordon and D. L. Looper, "Fundamental Parameters and Spectral Energy Distributions of Young and Field Age Objects with Masses Spanning the Stellar to Planetary Regime", ApJ, **810**, 158 (2015).

Fletcher, L. N., P. G. J. Irwin, N. A. Teanby, G. S. Orton, P. D. Parrish, R. de Kok, C. Howett, S. B. Calcutt, N. Bowles and F. W. Taylor, "Characterising Saturn's vertical temperature structure from Cassini/CIRS", Icarus, **189**, 457–478 (2007).

Foreman-Mackey, D., D. W. Hogg, D. Lang and J. Goodman, "emcee: The MCMC Hammer", PASP, **125**, 306 (2013).

Fortney, J. J., C. Mordasini, N. Nettelmann, E. M.-R. Kempton, T. P. Greene and K. Zahnle, "A Framework for Characterizing the Atmospheres of Low-mass Low-density Transiting Planets", ApJ, **775**, 80 (2013).

Freedman, R. S., J. Lustig-Yaeger, J. J. Fortney, R. E. Lupu, M. S. Marley and K. Lodders, "Gaseous Mean Opacities for Giant Planet and Ultracool Dwarf Atmospheres over a Range of Metallicities and Temperatures", ApJS, **214**, 25 (2014).

Freedman, R. S., M. S. Marley and K. Lodders, "Line and Mean Opacities for Ultracool Dwarfs and Extrasolar Planets", ApJS, **174**, 504–513 (2008).

Gaia Collaboration, A. G. A. Brown, A. Vallenari, T. Prusti, J. H. J. de Bruijne, C. Babusiaux, C. A. L. Bailer-Jones, M. Biermann, D. W. Evans, L. Eyer, F. Jansen, C. Jordi, S. A. Klioner, U. Lammers, L. Lindegren, X. Luri, F. Mignard, C. Panem, D. Pourbaix, S. Randich, P. Sartoretti, H. I. Siddiqui, C. Soubiran, F. van Leeuwen, N. A. Walton, F. Arenou, U. Bastian, M. Cropper, R. Drimmel, D. Katz, M. G. Lattanzi, J. Bakker, C. Cacciari, J. Castañeda, L. Chaoul,

N. Cheek, F. De Angeli, C. Fabricius, R. Guerra, B. Holl, E. Masana, R. Messineo, N. Mowlavi, K. Nienartowicz, P. Panuzzo, J. Portell, M. Riello, G. M. Seabroke, P. Tanga, F. Thévenin, G. Gracia-Abril, G. Comoretto, M. Garcia-Reinaldos, D. Teyssier, M. Altmann, R. Andrae, M. Audard, I. Bellas-Velidis, K. Benson, J. Berthier, R. Blomme, P. Burgess, G. Busso, B. Carry, A. Cellino, G. Clementini, M. Clotet, O. Creevey, M. Davidson, J. De Ridder, L. Delchambre, A. Dell'Oro, C. Ducourant, J. Fernández-Hernández, M. Fouesneau, Y. Frémat, L. Galluccio, M. García-Torres, J. González-Núñez, J. J. González-Vidal, E. Gosset, L. P. Guy, J. L. Halbwachs, N. C. Hambly, D. L. Harrison, J. Hernández, D. Hestroffer, S. T. Hodgkin, A. Hutton, G. Jasniewicz, A. Jean-Antoine-Piccolo, S. Jordan, A. J. Korn, A. Krone-Martins, A. C. Lanzafame, T. Lebzelter, W. Löffler, M. Manteiga, P. M. Marrese, J. M. Martín-Fleitas, A. Moitinho, A. Mora, K. Muinonen, J. Osinde, E. Pancino, T. Pauwels, J. M. Petit, A. Recio-Blanco, P. J. Richards, L. Rimoldini, A. C. Robin, L. M. Sarro, C. Siopis, M. Smith, A. Sozzetti, M. Süveges, J. Torra, W. van Reeven, U. Abbas, A. Abreu Aramburu, S. Accart, C. Aerts, G. Altavilla, M. A. Álvarez, R. Alvarez, J. Alves, R. I. Anderson, A. H. Andrei, E. Anglada Varela, E. Antiche, T. Antoja, B. Arcay, T. L. Astraatmadja, N. Bach, S. G. Baker, L. Balaguer-Núñez, P. Balm, C. Barache, C. Barata, D. Barbato, F. Barblan, P. S. Barklem, D. Barrado, M. Barros, M. A. Barstow, S. Bartholomé Muñoz, J. L. Bassilana, U. Becciani, M. Bellazzini, A. Berihuete, S. Bertone, L. Bianchi, O. Bienaymé, S. Blanco-Cuaresma, T. Boch, C. Boeche, A. Bombrun, R. Borrachero, D. Bossini, S. Bouquillon, G. Bourda, A. Bragaglia, L. Bramante, M. A. Breddels, A. Bressan, N. Brouillet, T. Brüsemeister, E. Brugaletta, B. Bucciarelli, A. Burlacu, D. Busonero, A. G. Butkevich, R. Buzzi, E. Caffau, R. Cancelliere, G. Cannizzaro, T. Cantat-Gaudin, R. Carballo, T. Carlucci, J. M. Carrasco, L. Casamiquela, M. Castellani, A. Castro-Ginard, P. Charlot, L. Chemin, A. Chiavassa, G. Cocozza, G. Costigan, S. Cowell, F. Crifo, M. Crosta, C. Crowley, J. Cuypers, C. Dafonte, Y. Damerdji, A. Dapergolas, P. David, M. David, P. de Laverny, F. De Luise, R. De March, D. de Martino, R. de Souza, A. de Torres, J. Debosscher, E. del Pozo, M. Delbo, A. Delgado, H. E. Delgado, P. Di Matteo, S. Diakite, C. Diener, E. Distefano, C. Dolding, P. Drazinos, J. Durán, B. Edvardsson, H. Enke, K. Eriksson, P. Esquej, G. Eynard Bontemps, C. Fabre, M. Fabrizio, S. Faigler, A. J. Falcão, M. Farràs Casas, L. Federici, G. Fedorets, P. Fernique, F. Figueras, F. Filippi, K. Findeisen, A. Fonti, E. Fraile, M. Fraser, B. Frézouls, M. Gai, S. Galleti, D. Garabato, F. García-Sedano, A. Garofalo, N. Garralda, A. Gavel, P. Gavras, J. Gerssen, R. Geyer, P. Giacobbe, G. Gilmore, S. Girona, G. Giuffrida, F. Glass, M. Gomes, M. Granvik, A. Gueguen, A. Guerrier, J. Guiraud, R. Gutiérrez-Sánchez, R. Haigron, D. Hatzidimitriou, M. Hauser, M. Haywood, U. Heiter, A. Helmi, J. Heu, T. Hilger, D. Hobbs, W. Hofmann, G. Holland, H. E. Huckle, A. Hypki, V. Icardi, K. Janßen, G. Jevardat de Fombelle, P. G. Jonker, Á. L. Juhász, F. Julbe, A. Karampelas, A. Kewley, J. Klar, A. Kochoska, R. Kohley, K. Kolenberg, M. Kontizas, E. Kontizas, S. E. Koposov, G. Kordopatis, Z. Kostrzewa-Rutkowska, P. Koubsky, S. Lambert, A. F. Lanza, Y. Lasne, J. B. Lavigne, Y. Le Fustec, C. Le Poncin-Lafitte, Y. Lebreton, S. Leccia, N. Leclerc, I. Lecoeur-Taibi, H. Lenhardt, F. Leroux, S. Liao, E. Licata, H. E. P. Lindstrøm, T. A. Lister, E. Livanou, A. Lobel, M. López, S. Managau, R. G. Mann, G. Mantelet, O. Marchal, J. M. Marchant, M. Marconi, S. Marinoni, G. Marschalkó,

D. J. Marshall, M. Martino, G. Marton, N. Mary, D. Massari, G. Matijevič, T. Mazeh, P. J. McMillan, S. Messina, D. Michalik, N. R. Millar, D. Molina, R. Molinaro, L. Molnár, P. Montegriffo, R. Mor, R. Morbidelli, T. Morel, D. Morris, A. F. Mulone, T. Muraveva, I. Musella, G. Nelemans, L. Nicastro, L. Noval, W. O'Mullane, C. Ordénovic, D. Ordóñez-Blanco, P. Osborne, C. Pagani, I. Pagano, F. Pailler, H. Palacin, L. Palaversa, A. Panahi, M. Pawlak, A. M. Piersimoni, F. X. Pineau, E. Plachy, G. Plum, E. Poggio, E. Poujoulet, A. Prša, L. Pulone, E. Racero, S. Ragaini, N. Rambaux, M. Ramos-Lerate, S. Regibo, C. Reylé, F. Riclet, V. Ripepi, A. Riva, A. Rivard, G. Rixon, T. Roegiers, M. Roelens, M. Romero-Gómez, N. Rowell, F. Royer, L. Ruiz-Dern, G. Sadowski, T. Sagristà Sellés, J. Sahlmann, J. Salgado, E. Salguero, N. Sanna, T. Santana-Ros, M. Sarasso, H. Savietto, M. Schultheis, E. Sciacca, M. Segol, J. C. Segovia, D. Ségransan, I. C. Shih, L. Siltala, A. F. Silva, R. L. Smart, K. W. Smith, E. Solano, F. Solitro, R. Sordo, S. Soria Nieto, J. Souchay, A. Spagna, F. Spoto, U. Stampa, I. A. Steele, H. Steidelmüller, C. A. Stephenson, H. Stoev, F. F. Suess, J. Surdej, L. Szabados, E. Szegedi-Elek, D. Tapiador, F. Taris, G. Tauran, M. B. Taylor, R. Teixeira, D. Terrett, P. Teyssand ier, W. Thuillot, A. Titarenko, F. Torra Clotet, C. Turon, A. Ulla, E. Utrilla, S. Uzzi, M. Vaillant, G. Valentini, V. Valette, A. van Elteren, E. Van Hemelryck, M. van Leeuwen, M. Vaschetto, A. Vecchiato, J. Veljanoski, Y. Viala, D. Vicente, S. Vogt, C. von Essen, H. Voss, V. Votruba, S. Voutsinas, G. Walmsley, M. Weiler, O. Wertz, T. Wevers, Ł. Wyrzykowski, A. Yoldas, M. Žerjal, H. Ziaeepour, J. Zorec, S. Zschocke, S. Zucker, C. Zurbach and T. Zwitter, "Gaia Data Release 2. Summary of the contents and survey properties", A&A, **616**, A1 (2018).

Geballe, T. R., D. Saumon, D. A. Golimowski, S. K. Leggett, M. S. Marley and K. S. Noll, "Spectroscopic Detection of Carbon Monoxide in Two Late-Type T Dwarfs", ApJ, **695**, 2, 844–854 (2009).

Gharib-Nezhad, E. and M. R. Line, "The Influence of H_2O Pressure Broadening in High-metallicity Exoplanet Atmospheres", ApJ, **872**, 1, 27 (2019).

Golimowski, D. A., S. K. Leggett, M. S. Marley, X. Fan, T. R. Geballe, G. R. Knapp, F. J. Vrba, A. A. Henden, C. B. Luginbuhl, H. H. Guetter, J. A. Munn, B. Canzian, W. Zheng, Z. I. Tsvetanov, K. Chiu, K. Glazebrook, E. A. Hoversten, D. P. Schneider and J. Brinkmann, "L' and M' Photometry of Ultracool Dwarfs", AJ, **127**, 6, 3516–3536 (2004).

Gonzales, E. C., B. Burningham, J. K. Faherty, C. Cleary, C. Visscher, M. S. Marley, R. Lupu and R. Freedman, "Retrieval of the d/sdL7+T7.5p Binary SDSS J1416+1348AB", ApJ, **905**, 1, 46 (2020).

Greathouse, T. K., M. Richter, J. Lacy, J. Moses, G. Orton, T. Encrenaz, H. B. Hammel and D. Jaffe, "A spatially resolved high spectral resolution study of Neptune's stratosphere", Icarus, **214**, 2, 606–621 (2011).

Hayashi, C. and T. Nakano, "Evolution of Stars of Small Masses in the Pre-Main-Sequence Stages", Progress of Theoretical Physics **30**, 460–474 (1963).

Helling, C. and S. Casewell, "Atmospheres of brown dwarfs", A&A Rv, **22**, 80 (2014).

Helling, C., P. Woitke, P. B. Rimmer, I. Kamp, W.-F. Thi and R. Meijerink, "Disk Evolution, Element Abundances and Cloud Properties of Young Gas Giant Planets", Life **4**, 142–173 (2014).

Hennebelle, P., "Formation of Low-Mass Stars and Brown Dwarfs", in "EAS Publications Series", edited by C. Reylé, C. Charbonnel and M. Schultheis, vol. 57 of *EAS Publications Series*, pp. 91–127 (2012).

Hinkel, N. R., F. X. Timmes, P. A. Young, M. D. Pagano and M. C. Turnbull, "Stellar Abundances in the Solar Neighborhood: The Hypatia Catalog", AJ, **148**, 54 (2014).

Husser, T. O., S. Wende-von Berg, S. Dreizler, D. Homeier, A. Reiners, T. Barman and P. H. Hauschildt, "A new extensive library of PHOENIX stellar atmospheres and synthetic spectra", A&A, **553**, A6 (2013).

Irwin, P. G. J., N. A. Teanby, R. de Kok, L. N. Fletcher, C. J. A. Howett, C. C. C. Tsang, C. F. Wilson, S. B. Calcutt, C. A. Nixon and P. D. Parrish, "The NEMESIS planetary atmosphere radiative transfer and retrieval tool", JQSRT, **109**, 1136–1150 (2008).

Kass, R. E. and A. E. Raftery, "Bayes factors", Journal of the American Statistical Association **90**, 430, 773–795 (1995).

Kirkpatrick, J. D., "New spectral types l and t", Annual Review of Astronomy and Astrophysics **43**, 1, 195–245 (2005).

Kirkpatrick, J. D., "New Spectral Types L and T", ARA&A, **43**, 1, 195–245 (2005).

Kirkpatrick, J. D., M. C. Cushing, C. R. Gelino, R. L. Griffith, M. F. Skrutskie, K. A. Marsh, E. L. Wright, A. Mainzer, P. R. Eisenhardt, I. S. McLean, M. A. Thompson, J. M. Bauer, D. J. Benford, C. R. Bridge, S. E. Lake, S. M. Petty, S. A. Stanford, C.-W. Tsai, V. Bailey, C. A. Beichman, J. S. Bloom, J. J. Bochanski, A. J. Burgasser, P. L. Capak, K. L. Cruz, P. M. Hinz, J. S. Kartaltepe, R. P. Knox, S. Manohar, D. Masters, M. Morales-Calderón, L. A. Prato, T. J. Rodigas, M. Salvato, S. D. Schurr, N. Z. Scoville, R. A. Simcoe, K. R. Stapelfeldt, D. Stern, N. D. Stock and W. D. Vacca, "The First Hundred Brown Dwarfs Discovered by the Wide-field Infrared Survey Explorer (WISE)", The Astrophysical Journal Supplement Series **197**, 19 (2011).

Kirkpatrick, J. D., C. R. Gelino, M. C. Cushing, G. N. Mace, R. L. Griffith, M. F. Skrutskie, K. A. Marsh, E. L. Wright, P. R. Eisenhardt, I. S. McLean, A. K. Mainzer, A. J. Burgasser, C. G. Tinney, S. Parker and G. Salter, "Further Defining Spectral Type "Y" and Exploring the Low-mass End of the Field Brown Dwarf Mass Function", ApJ, **753**, 156 (2012).

Kirkpatrick, J. D., E. C. Martin, R. L. Smart, A. J. Cayago, C. A. Beichman, F. Marocco, C. R. Gelino, J. K. Faherty, M. C. Cushing, A. C. Schneider, G. N. Mace, C. G. Tinney, E. L. Wright, P. J. Lowrance, J. G. Ingalls, F. J. Vrba, J. A. Munn, S. E. Dahm and I. S. McLean, "Preliminary Trigonometric Parallaxes of 184 Late-T and Y Dwarfs and an Analysis of the Field Substellar Mass Function into the "Planetary" Mass Regime", The Astrophysical Journal Supplement Series **240**, 19 (2019).

Kirkpatrick, J. D., I. N. Reid, J. Liebert, R. M. Cutri, B. Nelson, C. A. Beichman, C. C. Dahn, D. G. Monet, J. E. Gizis and M. F. Skrutskie, "Dwarfs Cooler than "M": The Definition of Spectral Type "L" Using Discoveries from the 2 Micron All-Sky Survey (2MASS)", ApJ, **519**, 802–833 (1999).

Knapp, G. R., S. K. Leggett, X. Fan, M. S. Marley, T. R. Geballe, D. A. Golimowski, D. Finkbeiner, J. E. Gunn, J. Hennawi, Z. Ivezić, R. H. Lupton, D. J. Schlegel, M. A. Strauss, Z. I. Tsvetanov, K. Chiu, E. A. Hoversten, K. Glazebrook, W. Zheng, M. Hendrickson, C. C. Williams, A. Uomoto, F. J. Vrba, A. A. Henden, C. B. Luginbuhl, H. H. Guetter, J. A. Munn, B. Canzian, D. P. Schneider and J. Brinkmann, "Near-Infrared Photometry and Spectroscopy of L and T Dwarfs: The Effects of Temperature, Clouds, and Gravity", AJ, **127**, 6, 3553–3578 (2004).

Kreidberg, L., M. R. Line, D. Thorngren, C. V. Morley and K. B. Stevenson, "Water, High-altitude Condensates, and Possible Methane Depletion in the Atmosphere of the Warm Super-Neptune WASP-107b", ApJL, **858**, 1, L6 (2018).

Krumholz, M. R., C. F. McKee and R. I. Klein, "The formation of stars by gravitational collapse rather than competitive accretion", Nature, **438**, 7066, 332–334 (2005).

Kumar, S. S., "The Structure of Stars of Very Low Mass.", ApJ, **137**, 1121 (1963).

Lacis, A. A. and V. Oinas, "A description of the correlated-k distribution method for modelling nongray gaseous absorption, thermal emission, and multiple scattering in vertically inhomogeneous atmospheres", J. Geophys. Res.,**96**, 9027–9064 (1991).

Lam, S. K., A. Pitrou and S. Seibert, "Numba: A llvm-based python jit compiler", in "Proceedings of the Second Workshop on the LLVM Compiler Infrastructure in HPC", pp. 1–6 (2015).

Leconte, J., "Why Compositional Convection Cannot Explain Substellar Objects Sharp Spectral-type Transitions", ApJL, **853**, L30 (2018).

Lee, J.-M., L. N. Fletcher and P. G. J. Irwin, "Optimal estimation retrievals of the atmospheric structure and composition of HD 189733b from secondary eclipse spectroscopy", MNRAS, **420**, 170–182 (2012).

Leggett, S. K., B. Burningham, D. Saumon, M. S. Marley, S. J. Warren, R. L. Smart, H. R. A. Jones, P. W. Lucas, D. J. Pinfield and M. Tamura, "Mid-Infrared Photometry of Cold Brown Dwarfs: Diversity in Age, Mass, and Metallicity", ApJ, **710**, 1627–1640 (2010).

Leggett, S. K., M. C. Cushing, K. K. Hardegree-Ullman, J. L. Trucks, M. S. Marley, C. V. Morley, D. Saumon, S. J. Carey, J. J. Fortney, C. R. Gelino, J. E. Gizis, J. D. Kirkpatrick and G. N. Mace, "Observed Variability at 1 and 4 μm in the Y0 Brown Dwarf WISEP J173835.52+273258.9", ApJ, **830**, 141 (2016a).

Leggett, S. K., C. V. Morley, M. S. Marley and D. Saumon, "Near-infrared Photometry of Y Dwarfs: Low Ammonia Abundance and the Onset of Water Clouds", ApJ, **799**, 37 (2015).

Leggett, S. K., C. V. Morley, M. S. Marley, D. Saumon, J. J. Fortney and C. Visscher, "A Comparison of Near-infrared Photometry and Spectra for Y Dwarfs with a New Generation of Cool Cloudy Models", ApJ, **763**, 130 (2013).

Leggett, S. K., D. Saumon, M. S. Marley, K. Lodders, J. Canty, P. Lucas, R. L. Smart, C. G. Tinney, D. Homeier, F. Allard, B. Burningham, A. Day-Jones, B. Fegley, M. Ishii, H. R. A. Jones, F. Marocco, D. J. Pinfield and M. Tamura, "The Properties of the 500 K Dwarf UGPS J072227.51-054031.2 and a Study of the Far-red Flux of Cold Brown Dwarfs", ApJ, **748**, 2, 74 (2012).

Leggett, S. K., D. Saumon, M. S. Marley, K. Lodders, J. Canty, P. Lucas, R. L. Smart, C. G. Tinney, D. Homeier, F. Allard, B. Burningham, A. Day-Jones, B. Fegley, M. Ishii, H. R. A. Jones, F. Marocco, D. J. Pinfield and M. Tamura, "THE PROPERTIES OF THE 500 k DWARF UGPS j072227.51–054031.2 AND a STUDY OF THE FAR-RED FLUX OF COLD BROWN DWARFS", The Astrophysical Journal **748**, 2, 74, URL

Leggett, S. K., P. Tremblin, T. L. Esplin, K. L. Luhman and C. V. Morley, "The Y-type Brown Dwarfs: Estimates of Mass and Age from New Astrometry, Homogenized Photometry, and Near-infrared Spectroscopy", ApJ, **842**, 118 (2017).

Leggett, S. K., P. Tremblin, D. Saumon, M. S. Marley, C. V. Morley, D. S. Amundsen, I. Baraffe and G. Chabrier, "Near-infrared Spectroscopy of the Y0 WISEP J173835.52+273258.9 and the Y1 WISE J035000.32-565830.2: The Importance of Non-equilibrium Chemistry", ApJ, **824**, 2 (2016b).

Leung, H. W. and J. Bovy, "Deep learning of multi-element abundances from high-resolution spectroscopic data", MNRAS, **483**, 3, 3255–3277 (2019).

Line, M. R., J. J. Fortney, M. S. Marley and S. Sorahana, "A Data-driven Approach for Retrieving Temperatures and Abundances in Brown Dwarf Atmospheres", ApJ, **793** (2014).

Line, M. R., M. S. Marley, M. C. Liu, B. Burningham, C. V. Morley, N. R. Hinkel, J. Teske, J. J. Fortney, R. Freedman and R. Lupu, "Uniform Atmospheric Retrieval Analysis of Ultracool Dwarfs. II. Properties of 11 T dwarfs", ApJ, **848**, 83 (2017).

Line, M. R., J. Teske, B. Burningham, J. J. Fortney and M. S. Marley, "Uniform Atmospheric Retrieval Analysis of Ultracool Dwarfs. I. Characterizing Benchmarks, Gl 570D and HD 3651B", ApJ, **807**, 183 (2015).

Line, M. R., X. Zhang, G. Vasisht, V. Natraj, P. Chen and Y. L. Yung, "Information Content of Exoplanetary Transit Spectra: An Initial Look", ApJ, **749**, 93 (2012).

Liska, M., C. Hesp, A. Tchekhovskoy, A. Ingram, M. van der Klis and S. Markoff, "Formation of precessing jets by tilted black hole discs in 3D general relativistic MHD simulations", MNRAS, **474**, 1, L81–L85 (2018).

Liu, M. C., T. J. Dupuy, B. P. Bowler, S. K. Leggett and W. M. J. Best, "Two Extraordinary Substellar Binaries at the T/Y Transition and the Y-band Fluxes of the Coolest Brown Dwarfs", ApJ, **758**, 57 (2012).

Lodders, K., "Solar System Abundances and Condensation Temperatures of the Elements", ApJ, **591**, 1220–1247 (2003).

Lodders, K. and B. Fegley, "Atmospheric Chemistry in Giant Planets, Brown Dwarfs, and Low-Mass Dwarf Stars. I. Carbon, Nitrogen, and Oxygen", Icarus, **155**, 393–424 (2002).

Lodieu, N., V. J. S. Béjar and R. Rebolo, "GTC OSIRIS z-band imaging of Y dwarfs", A&A, **550**, L2 (2013).

Luhman, K. L. and T. L. Esplin, "The Spectral Energy Distribution of the Coldest Known Brown Dwarf", AJ, **152**, 78 (2016).

Mace, G. N., J. D. Kirkpatrick, M. C. Cushing, C. R. Gelino, R. L. Griffith, M. F. Skrutskie, K. A. Marsh, E. L. Wright, P. R. Eisenhardt, I. S. McLean, M. A. Thompson, K. Mix, V. Bailey, C. A. Beichman, J. S. Bloom, A. J. Burgasser, J. J. Fortney, P. M. Hinz, R. P. Knox, P. J. Lowrance, M. S. Marley, C. V. Morley, T. J. Rodigas, D. Saumon, S. S. Sheppard and N. D. Stock, "A Study of the Diverse T Dwarf Population Revealed by WISE", The Astrophysical Journal Supplement Series **205**, 6 (2013).

Madhusudhan, N., "Exoplanetary Atmospheres: Thermal Inversions and Self-consistent Models", in "Radiative Signatures from the Cosmos", edited by K. Werner, C. Stehle, T. Rauch and T. Lanz, vol. 519 of *Astronomical Society of the Pacific Conference Series*, p. 129 (2019).

Madhusudhan, N., M. A. Amin and G. M. Kennedy, "Toward Chemical Constraints on Hot Jupiter Migration", ApJL, **794**, L12 (2014).

Madhusudhan, N. and S. Seager, "A Temperature and Abundance Retrieval Method for Exoplanet Atmospheres", ApJ, **707**, 1, 24–39 (2009).

Madhusudhan, N. and S. Seager, "High Metallicity and Non-equilibrium Chemistry in the Dayside Atmosphere of hot-Neptune GJ 436b", ApJ, **729**, 41 (2011).

Malik, M., L. Grosheintz, J. M. Mendonça, S. L. Grimm, B. Lavie, D. Kitzmann, S.-M. Tsai, A. Burrows, L. Kreidberg, M. Bedell, J. L. Bean, K. B. Stevenson and K. Heng, "HELIOS: An Open-source, GPU-accelerated Radiative Transfer Code for Self-consistent Exoplanetary Atmospheres", AJ, **153**, 2, 56 (2017).

Mann, A. W., G. A. Feiden, E. Gaidos, T. Boyajian and K. von Braun, "How to Constrain Your M Dwarf: Measuring Effective Temperature, Bolometric Luminosity, Mass, and Radius", ApJ, **804**, 64 (2015).

Mansfield, M., J. L. Bean, M. R. Line, V. Parmentier, L. Kreidberg, J.-M. Désert, J. J. Fortney, K. B. Stevenson, J. Arcangeli and D. Dragomir, "An HST/WFC3 Thermal Emission Spectrum of the Hot Jupiter HAT-P-7b", AJ, **156**, 1, 10 (2018).

Marley, M. S. and S. K. Leggett, "The Future of Ultracool Dwarf Science with JWST", Astrophysics and Space Science Proceedings **10**, 101 (2009).

Marley, M. S. and T. D. Robinson, "On the Cool Side: Modeling the Atmospheres of Brown Dwarfs and Giant Planets", ARA&A, **53**, 279–323 (2015).

Marley, M. S., D. Saumon, J. J. Fortney, C. Morley, R. E. Lupu, R. Freedman and C. Visscher, "Sonora: A New Generation Model Atmosphere Grid for Brown Dwarfs and Young Extrasolar Giant Planets", in "American Astronomical Society Meeting Abstracts #230", vol. 230 of *American Astronomical Society Meeting Abstracts*, p. 315.07 (2017).

Marley, M. S., D. Saumon and C. Goldblatt, "A Patchy Cloud Model for the L to T Dwarf Transition", ApJL, **723**, 1, L117–L121 (2010).

Marley, M. S., D. Saumon, T. Guillot, R. S. Freedman, W. B. Hubbard, A. Burrows and J. I. Lunine, "Atmospheric, Evolutionary, and Spectral Models of the Brown Dwarf Gliese 229 B", Science **272**, 1919–1921 (1996).

Marley, M. S., D. Saumon, C. Visscher, R. Lupu, R. Freedman, C. Morley, J. J. Fortney, C. Seay, A. J. R. W. Smith, D. J. Teal and R. Wang, "The Sonora Brown Dwarf Atmosphere and Evolution Models. I. Model Description and Application to Cloudless Atmospheres in Rainout Chemical Equilibrium", ApJ, **920**, 2, 85 (2021a).

Marley, M. S., D. Saumon, C. Visscher, R. Lupu, R. Freedman, C. Morley, J. J. Fortney, C. Seay, A. J. R. W. Smith, D. J. Teal and R. Wang, "The Sonora Brown Dwarf Atmosphere and Evolution Models I. Model Description and Application to Cloudless Atmospheres in Rainout Chemical Equilibrium", arXiv e-prints p. arXiv:2107.07434 (2021b).

Marley, M. S., S. Seager, D. Saumon, K. Lodders, A. S. Ackerman, R. S. Freedman and X. Fan, "Clouds and Chemistry: Ultracool Dwarf Atmospheric Properties from Optical and Infrared Colors", ApJ, **568**, 335–342 (2002).

Martin, E. C., J. D. Kirkpatrick, C. A. Beichman, R. L. Smart, J. K. Faherty, C. R. Gelino, M. C. Cushing, A. C. Schneider, E. L. Wright, P. Lowrance, J. Ingalls, C. G. Tinney, I. S. McLean, S. E. Logsdon and J. Lebreton, "Y Dwarf Trigonometric Parallaxes from the Spitzer Space Telescope", ApJ, **867**, 109 (2018).

Meisner, A. M., A. C. Schneider, A. J. Burgasser, F. Marocco, M. R. Line, J. K. Faherty, J. D. Kirkpatrick, D. Caselden, M. J. Kuchner, C. R. Gelino, J. Gagne, C. Theissen, R. Gerasimov, C. Aganze, C.-C. Hsu, J. P. Wisniewski, S. L. Casewell, D. C. Bardalez Gagliuffi, S. E. Logsdon, P. R. M. Eisenhardt, K. Allers, J. H. Debes, M. B. Allen, N. Stevnbak Andersen, S. Goodman, L. Gramaize, D. W. Martin, A. Sainio, M. C. Cushing, T. Backyard Worlds, : and Planet 9 Collaboration, "New Candidate Extreme T Subdwarfs from the Backyard Worlds: Planet 9 Citizen Science Project", arXiv e-prints p. arXiv:2106.01387 (2021).

Miles, B. E., A. J. I. Skemer, C. V. Morley, M. S. Marley, J. J. Fortney, K. N. Allers, J. K. Faherty, T. R. Geballe, C. Visscher, A. C. Schneider, R. Lupu, R. S. Freedman and G. L. Bjoraker, "Observations of Disequilibrium CO Chemistry in the Coldest Brown Dwarfs", AJ, **160**, 2, 63 (2020).

Mollière, P., R. van Boekel, J. Bouwman, T. Henning, P.-O. Lagage and M. Min, "Observing transiting planets with JWST. Prime targets and their synthetic spectral observations", A&A, **600**, A10 (2017).

Mordasini, C., R. van Boekel, P. Mollière, T. Henning and B. Benneke, "The Imprint of Exoplanet Formation History on Observable Present-day Spectra of Hot Jupiters", ApJ, **832**, 41 (2016).

Morley, C. V., J. J. Fortney, M. S. Marley, C. Visscher, D. Saumon and S. K. Leggett, "Neglected Clouds in T and Y Dwarf Atmospheres", ApJ, **756**, 172 (2012).

Morley, C. V., M. S. Marley, J. J. Fortney, R. Lupu, D. Saumon, T. Greene and K. Lodders, "Water Clouds in Y Dwarfs and Exoplanets", ApJ, **787**, 78 (2014).

Morley, C. V., A. J. Skemer, K. N. Allers, M. S. Marley, J. K. Faherty, C. Visscher, S. A. Beiler, B. E. Miles, R. Lupu, R. S. Freedman, J. J. Fortney, T. R. Geballe and G. L. Bjoraker, "An L Band Spectrum of the Coldest Brown Dwarf", ArXiv e-prints (2018).

Nitadori, K. and S. J. Aarseth, "Accelerating NBODY6 with graphics processing units", MNRAS, **424**, 1, 545–552 (2012).

Noll, K. S., T. R. Geballe and M. S. Marley, "Detection of Abundant Carbon Monoxide in the Brown Dwarf Gliese 229B", ApJL, **489**, 1, L87–L90 (1997).

NVIDIA, P. Vingelmann and F. H. Fitzek, "Cuda, release: 10.2.89", URL `https://developer.nvidia.com/cuda-toolkit` (2020).

Öberg, K. I., R. Murray-Clay and E. A. Bergin, "The Effects of Snowlines on C/O in Planetary Atmospheres", ApJL, **743**, L16 (2011).

Opitz, D., C. G. Tinney, J. K. Faherty, S. Sweet, C. R. Gelino and J. D. Kirkpatrick, "Searching for Binary Y Dwarfs with the Gemini Multi-conjugate Adaptive Optics System (GeMS)", ApJ, **819**, 17 (2016).

Oppenheimer, B. R., S. R. Kulkarni, K. Matthews and T. Nakajima, "Infrared Spectrum of the Cool Brown Dwarf Gl 229B", Science **270**, 1478–1479 (1995).

Oppenheimer, B. R., S. R. Kulkarni, K. Matthews and M. H. van Kerkwijk, "The Spectrum of the Brown Dwarf Gliese 229B", ApJ, **502**, 2, 932–943 (1998).

Owens, J. D., D. Luebke, N. Govindaraju, M. Harris, J. Krüger, A. E. Lefohn and T. J. Purcell, "A survey of general-purpose computation on graphics hardware", Computer Graphics Forum **26**, 1, 80–113, URL `https://onlinelibrary.wiley.com/doi/abs/10.1111/j.1467-8659.2007.01012.x` (2007).

Parviainen, H., "PYTRANSIT: fast and easy exoplanet transit modelling in PYTHON", MNRAS, **450**, 3, 3233–3238 (2015).

Patience, J., R. R. King, R. J. De Rosa, A. Vigan, S. Witte, E. Rice, C. Helling and P. Hauschildt, "Spectroscopy across the brown dwarf/planetary mass boundary. I. Near-infrared JHK spectra", A&A, **540**, A85 (2012).

Pecaut, M. J. and E. E. Mamajek, "Intrinsic Colors, Temperatures, and Bolometric Corrections of Pre-main-sequence Stars", ApJS, **208**, 9 (2013).

Piskorz, D., C. Buzard, M. R. Line, H. A. Knutson, B. Benneke, N. R. Crockett, A. C. Lockwood, G. A. Blake, T. S. Barman, C. F. Bender, D. Deming and J. A. Johnson, "Ground- and Space-based Detection of the Thermal Emission Spectrum of the Transiting Hot Jupiter KELT-2Ab", AJ, **156**, 133 (2018).

Piskorz, D., C. Buzard, M. R. Line, H. A. Knutson, B. Benneke, N. R. Crockett, A. C. Lockwood, G. A. Blake, T. S. Barman, C. F. Bender, D. Deming and J. A. Johnson, "Ground- and space-based detection of the thermal emission spectrum of the transiting hot jupiter KELT-2ab", The Astronomical Journal **156**, 3, 133, URL

Press, W. H., S. A. Teukolsky, W. T. Vetterling and B. P. Flannery, *Numerical Recipes in C* (Cambridge University Press, Cambridge, USA, 1992), second edn.

Rajan, A., J. Patience, P. A. Wilson, J. Bulger, R. J. De Rosa, K. Ward-Duong, C. Morley, F. Pont and R. Windhorst, "The brown dwarf atmosphere monitoring (BAM) project - II. Multi-epoch monitoring of extremely cool brown dwarfs", MNRAS, **448**, 3775–3783 (2015).

Rebolo, R., M. R. Zapatero Osorio and E. L. Martín, "Discovery of a brown dwarf in the Pleiades star cluster", Nature, **377**, 129–131 (1995).

Rice, E. L., R. Oppenheimer, N. Zimmerman, L. C. Roberts and S. Hinkley, "A New Method for Characterizing Very Low-Mass Companions with Low-Resolution Near-Infrared Spectroscopy", Publications of the Astronomical Society of the Pacific **127**, 479 (2015).

Samland, M., P. Mollière, M. Bonnefoy, A. L. Maire, F. Cantalloube, A. C. Cheetham, D. Mesa, R. Gratton, B. A. Biller, Z. Wahhaj, J. Bouwman, W. Brandner, D. Melnick, J. Carson, M. Janson, T. Henning, D. Homeier, C. Mordasini, M. Langlois, S. P. Quanz, R. van Boekel, A. Zurlo, J. E. Schlieder, H. Avenhaus, J. L. Beuzit, A. Boccaletti, M. Bonavita, G. Chauvin, R. Claudi, M. Cudel, S. Desidera,

M. Feldt, T. Fusco, R. Galicher, T. G. Kopytova, A. M. Lagrange, H. Le Coroller, P. Martinez, O. Moeller-Nilsson, D. Mouillet, L. M. Mugnier, C. Perrot, A. Sevin, E. Sissa, A. Vigan and L. Weber, "Spectral and atmospheric characterization of 51 Eridani b using VLT/SPHERE", A&A, **603** (2017).

Saumon, D., W. B. Hubbard, A. Burrows, T. Guillot, J. I. Lunine and G. Chabrier, "A Theory of Extrasolar Giant Planets", ApJ, **460**, 993 (1996).

Saumon, D. and M. S. Marley, "The Evolution of L and T Dwarfs in Color-Magnitude Diagrams", ApJ, **689**, 1327–1344 (2008).

Saumon, D., M. S. Marley, M. Abel, L. Frommhold and R. S. Freedman, "New H_2 Collision-induced Absorption and NH_3 Opacity and the Spectra of the Coolest Brown Dwarfs", ApJ, **750**, 74 (2012).

Saumon, D., M. S. Marley, M. C. Cushing, S. K. Leggett, T. L. Roellig, K. Lodders and R. S. Freedman, "Ammonia as a Tracer of Chemical Equilibrium in the T7.5 Dwarf Gliese 570D", ApJ, **647**, 552–557 (2006).

Saumon, D., M. S. Marley, S. K. Leggett, T. R. Geballe, D. Stephens, D. A. Golimowski, M. C. Cushing, X. Fan, J. T. Rayner, K. Lodders and R. S. Freedman, "Physical Parameters of Two Very Cool T Dwarfs", ApJ, **656**, 2, 1136–1149 (2007).

Saumon, D., M. S. Marley, K. Lodders and R. S. Freedman, "Non-equilibrium Chemistry in the Atmospheres of Brown Dwarfs", in "Brown Dwarfs", edited by E. Martín, vol. 211, p. 345 (2003).

Schneider, A. C., M. C. Cushing, J. D. Kirkpatrick, C. R. Gelino, G. N. Mace, E. L. Wright, P. R. Eisenhardt, M. F. Skrutskie, R. L. Griffith and K. A. Marsh, "Hubble Space Telescope Spectroscopy of Brown Dwarfs Discovered with the Wide-field Infrared Survey Explorer", ApJ, **804**, 92 (2015).

Sharp, C. M. and A. Burrows, "Atomic and Molecular Opacities for Brown Dwarf and Giant Planet Atmospheres", ApJS, **168**, 140–166 (2007).

Shu, F. H., "Self-similar collapse of isothermal spheres and star formation.", ApJ, **214**, 488–497 (1977).

Smart, R. L., D. Apai, J. D. Kirkpatrick, S. K. Leggett, F. Marocco, J. E. Morrison, H. R. A. Jones, D. Pinfield, P. Tremblin and D. S. Amundsen, "Parallaxes and infrared photometry of three Y0 dwarfs", MNRAS, **468**, 3764–3774 (2017).

Sorahana, S., T. K. Suzuki and I. Yamamura, "A signature of chromospheric activity in brown dwarfs revealed by 2.5-5.0 μm AKARI spectra", MNRAS, **440**, 3675–3684 (2014).

Sorahana, S. and I. Yamamura, "AKARI Observations of Brown Dwarfs. III. CO, CO_2, and CH_4 Fundamental Bands and Physical Parameters", ApJ, **760**, 2, 151 (2012).

Tinney, C. G., A. J. Burgasser and J. D. Kirkpatrick, "Infrared Parallaxes for Methane T Dwarfs", AJ, **126**, 2, 975–992 (2003).

Tinney, C. G., J. K. Faherty, J. D. Kirkpatrick, M. Cushing, C. V. Morley and E. L. Wright, "The Luminosities of the Coldest Brown Dwarfs", ApJ, **796**, 39 (2014).

Tinney, C. G., J. K. Faherty, J. D. Kirkpatrick, E. L. Wright, C. R. Gelino, M. C. Cushing, R. L. Griffith and G. Salter, "WISE J163940.83-684738.6: A Y Dwarf Identified by Methane Imaging", ApJ, **759**, 60 (2012).

Toon, O. B., C. P. McKay, T. P. Ackerman and K. Santhanam, "Rapid calculation of radiative heating rates and photodissociation rates in inhomogeneous multiple scattering atmospheres", J. Geophys. Res.,**94**, 16287–16301 (1989).

Tremblin, P., D. S. Amundsen, P. Mourier, I. Baraffe, G. Chabrier, B. Drummond, D. Homeier and O. Venot, "Fingering Convection and Cloudless Models for Cool Brown Dwarf Atmospheres", ApJ, **804**, L17 (2015).

Tsuji, T., K. Ohnaka, W. Aoki and T. Nakajima, "Evolution of dusty photospheres through red to brown dwarfs: how dust forms in very low mass objects.", A&A, **308**, L29–L32 (1996).

Twomey, S., B. Herman and R. Rabinoff, "An extension to the chahine method of inverting the radiative transfer equation", Journal of the Atmospheric Sciences **34**, 7, 1085–1090 (1977).

Uehara, H. and S.-i. Inutsuka, "Does Deuterium Enable the Formation of Primordial Brown Dwarfs?", ApJL, **531**, 2, L91–L94 (2000).

Wang, L., R. Spurzem, S. Aarseth, M. Giersz, A. Askar, P. Berczik, T. Naab, R. Schadow and M. B. N. Kouwenhoven, "The DRAGON simulations: globular cluster evolution with a million stars", MNRAS, **458**, 2, 1450–1465 (2016).

Wang, L., R. Spurzem, S. Aarseth, K. Nitadori, P. Berczik, M. B. N. Kouwenhoven and T. Naab, "NBODY6++GPU: ready for the gravitational million-body problem", MNRAS, **450**, 4, 4070–4080 (2015).

Whitworth, A., M. R. Bate, Å. Nordlund, B. Reipurth and H. Zinnecker, "The Formation of Brown Dwarfs: Theory", in "Protostars and Planets V", edited by B. Reipurth, D. Jewitt and K. Keil, p. 459 (2007).

Whitworth, A. P. and D. Stamatellos, "The minimum mass for star formation, and the origin of binary brown dwarfs", Astronomy & Astrophysics **458**, 3, 817–829, URL `http://dx.doi.org/10.1051/0004-6361:20065806` (2006).

Yuan, T. T., L. J. Kewley, A. M. Swinbank, J. Richard and R. C. Livermore, "Metallicity Gradient of a Lensed Face-on Spiral Galaxy at Redshift 1.49", ApJL, **732**, 1, L14 (2011).

Zahnle, K. J. and M. S. Marley, "Methane, Carbon Monoxide, and Ammonia in Brown Dwarfs and Self-Luminous Giant Planets", ApJ, **797**, 41 (2014).

Zalesky, J. A., M. R. Line, A. C. Schneider and J. Patience, "A Uniform Retrieval Analysis of Ultra-cool Dwarfs. III. Properties of Y Dwarfs", ApJ, **877**, 1, 24 (2019).

Zhang, Z., M. C. Liu, M. S. Marley, M. R. Line and W. M. J. Best, "Uniform Forward-modeling Analysis of Ultracool Dwarfs. I. Methodology and Benchmarking", ApJ, **916**, 1, 53 (2021a).

Zhang, Z., M. C. Liu, M. S. Marley, M. R. Line and W. M. J. Best, "Uniform Forward-Modeling Analysis of Ultracool Dwarfs. II. Atmospheric Properties of 55 Late-T Dwarfs", arXiv e-prints p. arXiv:2105.05256 (2021b).